Development of porous materials based on styrene-ethylene-butylene-styrene for oil spill remediation

by

Hyejin Lee

A thesis

presented to the University of Waterloo

in fulfillment of the

thesis requirement for the degree of

Master of Applied Science

in

Chemical Engineering

Waterloo, Ontario, Canada, 2023

Author's Declaration

This thesis consists of material all of which I authored or co-authored: see Statement of Contributions included in the thesis. This is a true copy of the thesis, including any required final revisions, as accepted by my examiners.

I understand that my thesis may be made electronically available to the public.

Statement of Contributions

Chapter 2 presents a literature review that delves into the recent advancements in the field of porous polymeric materials for oil absorption applications. This review is adapted from a draft manuscript currently refined for submission, and as a result, the content within this thesis may undergo modifications. For this work, I served as the lead author. Dr. Boon Peng Chang offered supplementary guidance and Dr. Mekonnen contributed by providing direction and reviewing the manuscript to ensure its quality and relevance.

Chapter 3 is adapted from a manuscript that is currently under review for publication entitled, “Fabrication of triblock elastomer foams for oil absorption applications: effects of crosslinking, composition, and rheology factors”. As the first author of this work, I carried out all experiments, analyzed the data, and composed the initial draft of the paper. Dr. Gupta played a significant role in designing the experiments and offering guidance, while also contributing to the improvement of the draft. Dr. Mekonnen, who conceptualized the project, provided valuable guidance and supervision throughout the process, in addition to reviewing the manuscript.

Chapter 4 is adapted from a manuscript that is currently in the final stages of preparation for submission. In this joint endeavor, I took on the role of the lead author, working closely with research associate Binh-Minh Trinh to design experiments and write the draft. Ethan Alec Crawford, a co-op student in Dr. Mekonnen's group, made significant contributions by conducting experiments and assisting with the creation of some figures. Dr. Gupta provided valuable technical assistance in

designing the melt-blowing process. Dr. Mekonnen, who conceptualized, offered guidance and supervision throughout the process, as well as reviewed the manuscript to ensure its accuracy and relevance.

Abstract

Marine oil spills, resulting from catastrophic equipment failure during oil transportation or the release of oily wastewater from industrial operations, can lead to economic losses and severe environmental damage to marine life. The urgent need for polluted water remediation has prompted scientists and technocrats to develop oil spill cleanup methods, and Oil sorbents have emerged as one of the most effective solutions, as they cause minimal harm to the marine environment and quickly remove pollutants with high oil uptake efficiency. Hydrophobic polymeric foams and fibers, in particular, have gained recognition for their porous structures and large surface areas, which grant them enhanced sorption capacity and separation efficiency.

Styrene-ethylene-butylene-styrene (SEBS) is a hydrophobic and oleophilic thermoplastic elastomer, consisting of rubbery midblock (ethylene-butylene) and glassy end blocks (styrene). The midblock is soluble in hydrocarbon oil, while the end blocks are not, allowing the polymer to selectively capture oil while maintaining its elasticity. SEBS's unique features make it an excellent candidate for an oil sorbent with high oil absorption capacity, efficient oil/water separation, and selective oil congealing properties. However, creating a porous SEBS material is challenging due to its poor melt strength and low melt flow index.

In this thesis, the development of porous structures based on SEBS as mitigation approaches to address the oil spill challenge are investigated and presented. In the first part, the fabrication of a novel and highly effective elastomer foam based on a styrene-ethylene-butylene-styrene (SEBS) and ethylene propylene diene monomer (EPDM) blend was studied. Dicumyl peroxide served as a

radical initiator for the elastomer blend's crosslinking. This crosslinking significantly improved the melt strength of the SEBS/EPDM blend, allowing for extensive expansion and the creation of well-defined porous structures. Consequently, the material exhibited exceptional oil absorption capabilities due to the increased surface.

The later section focuses on developing melt-blown SEBS. To overcome the inherent low melt flow index (MFI) of SEBS, which hinders the melt-blowing process, high MFI polypropylene (PP) was incorporated as a blending additive. The impact of blending polypropylene with SEBS on melt-blowing processability and fiber quality was then examined. Notably, adding 10 wt% PP to SEBS significantly enhances fiber melt-blowing processability, resulting in a more extensive and evenly dispersed fiber stream. Further analysis revealed superior oil uptake capacity and increased surface area, enabling effective interaction between SEBS-based fibers and oil. This interaction led to the formation of a semi-solid gel that creates a barrier, limiting further oil dispersion even at saturation point, demonstrating a markedly superior oil immobilization performance compared to conventional polypropylene melt-blown fibers. Overall, this study showed that the rational design of porous structures from SEBS allows the selective sorption of oil from water.

Acknowledgments

I would like to express my deepest gratitude to my esteemed supervisor, Dr. Tizazu Mekonnen, for his unwavering guidance, support, and encouragement throughout the completion of my Master thesis. His invaluable expertise, keen insight, and genuine passion for my research topic not only inspired me to delve deeper into my studies, but also fostered an environment of intellectual curiosity and growth. Dr. Mekonnen's patience, enthusiasm, and commitment to my academic and personal development have left an indelible mark on my journey, and I am truly grateful for the opportunity to learn from such a dedicated and compassionate mentor.

I am grateful for the financial support provided by Albarrie Canada Limited and Ontario Centre of Innovation (OCI).

My warmest appreciation goes out to the amazing colleagues from Dr. Mekonnen's group. A special thanks goes out to Arvind, Binh, and Ethan for closely collaborating with me on my projects, and to Debela, Rohan, Azin, Dylan, Will, Rachel, Kyle, Parinaz, Mohammed, and Karelle for their companionship and support. Their collective dedication, passion for learning, and unique perspectives have truly enhanced my academic experience. Together, we've created a fantastic group that has made the journey both rewarding and enjoyable.

I would like to extend my sincere appreciation to Jerry and the Jacobson family for their warmth and generosity. Their kindness turned my study abroad experience in Canada into a series of wonderful memories, taking away any loneliness that could've come with it. I am grateful for the

laughter, love, and unforgettable moments we shared. Thank you for providing me with a home away from home.

Finally, I must acknowledge the unwavering support of my family, who have been instrumental in my journey. Despite the physical distance between us, my dear family in Korea and Japan have provided me with an abundance of emotional support and encouragement. I am truly grateful for the love and strength that my mom, dad, Hyejong, Haesong, Miyoung, and my adorable nephew Gi Hun have given me throughout this process.

Table of Contents

List of Figures

List of Tables

Chapter 1: Introduction

1.1. Overview

With the growth of industry and urbanization, there has been a substantial increase in petroleum usage in areas such as transportation, power generation, and the fabrication of plastics and chemicals. It is derived from organic substances such as ancient plants and marine creatures that have been buried under sediment in the ocean and the land [1]. Petroleum is extracted and transported to refineries, where it is processed into various petrochemicals such as diesel and gasoline. However, oil extraction, transportation, and processing often result in spills and a large amount of oily wastewater discharge, leading to significant marine pollution, detrimental environmental impacts, and considerable economic losses [2]. Despite the improved production technologies and safety precautions that have reduced accidental spills from oil platforms to around 3% of the petroleum inputs worldwide [3], major oil spill accidents continue to occur regularly worldwide.

Some of the most significant oil spill accidents that occurred from 1970 include the collision of Atlantic Empress/Aegean Captain (1979) that caused 160,000 metric tons of oil release, the major oil spill in the Gulf of Mexico (1979) of 450,000 metric tons, the Gulf War oil spill in Kuwait (1991) that 1 million metric tons of crude oil were released, Sea Empress (1996) that spilled 3 million metric tons of crude oil, and Deepwater Horizon (2010) in the Gulf of Mexico of 680,000 metric tons oil spill [4–6].

The consequences of oil spills can be severe, impacting marine and terrestrial ecosystems for years and requiring billions of dollars for restoration efforts. When oil spills over the ocean, it reduces the amount of dissolved oxygen in the water and blocks sunlight from penetrating the surface. This can have devastating effects on marine life, causing hypothermia and death among birds and mammals whose waterproofing and insulating properties are compromised by the oil [7]. In addition, oil spills have caused serious water pollution to the environment and affected the global economy; thus, research and development into highly efficient oil spill cleanup methods have become of paramount importance.

In recent years, extensive studies have been conducted, and numerous oil spill cleanup methods have been developed. The choice of the methods is dependent on various factors, such as the amount and the type of oil discharged, the weather (wind and waves), and the surrounding environment (ecosystems and marine species) of the oil-spilled site. The major recovery methods include chemical, bioremediation, in-situ burning, and physical methods [8].

The chemical methods involve the use of chemicals that alter the physical and chemical properties of the oil, facilitating its containment and cleaning [9]. Dispersants and solidifiers are two types of chemicals commonly used for this method. Dispersants are surfactants that function by breaking down the oil slick into smaller droplets that can be dispersed in the ocean (**Fig. 1.1**). The diluted oil is then consumed by native marine microbes, as hydrocarbons are great sources of carbon and energy for them [10,11]. Solidifiers are hydrophobic granules that work as coagulants. When reacted with oil, it changes the oil from a liquid to a rubbery state so that oil compounds can be efficiently removed. They are usually employed along with physical clean-up methods such as

booms and skimmers. The advantage of chemical methods is that they can quickly prevent the spread of oil spills; however, those chemicals can be noxious to several marine organisms.

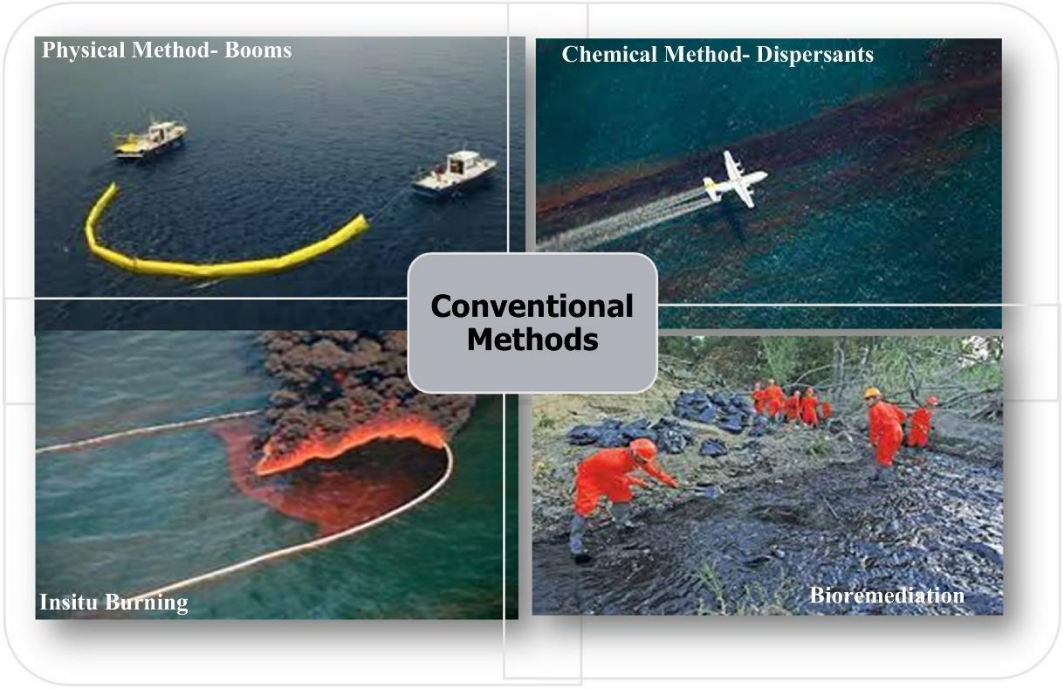

Fig. 1.1. The conventional oil spill remediation methods. (Reproduced with permission from [7]. Copyright 2022 Elsevier Inc)

The bioremediation method uses biodegradation via microorganisms, such as bacteria, fungi, protozoa, and nematodes, that metabolize and degrade hydrocarbons in crude oil [12]. Organic substances are flocculated by aggregated microorganisms, and a form of sludge is generated. Through this process, the pollutants are degraded into non-toxic gases like CO_2 and H_2O, which is helpful in restoring the sea environment [13]. Alkanes and aromatic compounds of low molecular weight are rapidly degraded by enzyme microbes; however, complex organic compounds require a longer time to degrade, as there are a smaller number of microorganisms that can break them

down [14]. Bioremediation has the benefit of being a relatively cheap and eco-friendly technology. However, this method is not free of limitations; some organic components are only degraded by specific species of microorganisms, it needs to meet strict conditions for the microbes to proliferate, and depending on the oil concentration, inherent biodegradability, and biological environment, the biodegradation can take a long time from several weeks to months [15,16].

As thermal remediation, *in-situ* burning is considered an efficient method that prevents the environmental damage of oil discharged into sensitive aquatic ecosystems by burning off a significant portion of the oil [17] (**Fig. 1.1**). It can be conducted rapidly in urgent situations where spilled oil poses a serious hazard to marine habitats and the environment. However, burning oil can generate pollutants such as monoxide, sulfur dioxide, nitrogen oxides, and particulate matter which can have a detrimental impact on the air condition [18]. Also, in-situ burning might not be suitable for thick oil and unfavorable weather, which can restrict its implementation.

The physical cleanup method involves the application of mechanical means to remove oil without changing the chemical and physical properties of the oil [19]. Booms and skimmers are essential tools for containing and recovering oil spills. Booms are utilized to contain and control the spread of oil spills on water's surface, and they can be deployed quickly to form a barrier. A skimmer is another mechanical device often utilized in conjunction with a containment boom for effective oil cleanup. Fence booms, curtain booms (inflated booms), and fire-resistant booms are some of the types available, and their effectiveness is determined by factors, such as the type and concentration of the spilled oil [20,21] (**Fig. 1.1**). Unfortunately, their utilization has some downsides – as for boomers, much of the spilled oil sinks to the bottom causing damage to marine life undersea and

forming tar balls [22]. Also, skimmers often show an inefficiency in separating water from the extracted, which leads to high recycling costs and difficulties.

Meanwhile, employing sorbents (absorbents and adsorbents) have been widely accepted as one of the most efficient physical methods for oil/water separation [23]. The sorbent materials are generally offered with advantageous properties such as cost-efficiency, lightweight, high oil uptake capacity, and rapid oil sorption. Moreover, it has a tremendous environmental benefit, as it does not involve chemicals during the oil cleanup. Various sorbent materials such as silica/graphene [24], polypropylene nonwoven fibers [25], butyl rubber [25], kapok fiber [26], cellulose aerogel [27], polyurethane foam [28], exfoliated graphite [29], etc. have been developed and these materials possess excellent hydrophobicity and oleophilicity. Among these, hydrophobic polymeric foams and fibers have particularly been lauded for their porous structures and large surface area, providing them with enhanced sorption capacity and separation efficiency [30–33].

1.2. Thesis outline

The aim of this study is to present an in-depth understanding of SEBS-based polymeric foams and melt-blown fibers with both aspects of 1) the fundamentals of foaming and melt-blowing and 2) their applications as oil sorbents. Following the introduction, Chapter 2 provides a comprehensive literature review focusing on the processing technology and fundamentals of polymer foaming and melt-blowing, along with exploring the application of polymer foam and melt-blown fibers as oil sorbents. Chapter 3 delves into the research work on the polymer foaming of thermoplastic elastomers, detailing the fabrication process and characterization of SEBS-based foams that exhibit significant foaming expansion and oil absorption capacity due to their increased surface area. Chapter 4 encompasses an in-depth examination of the fabrication, characterization, and functionalization of melt-blown SEBS fibers. These fibers effectively capture and immobilize oil due to their enhanced gel formation capacity and demonstrate outstanding oil/water separation ability, attributable to their porous structure and densely packed fiber mat formation. Lastly, Chapter 5 presents the overall conclusions and potential future directions.

Chapter 2: Literature Review

2.1. Polymeric foams as oil-absorbing materials

Polymeric foam is a low-density porous material created by incorporating a large amount of entrapped gas into a polymer matrix [34]. The presence of nano/micro-sized pores gives the polymeric foam a spongy, cellular structure that provides cushioning and buoyant properties. Also, polymeric foam is known to have many advantages over non-foamed polymer, which in turn allows the polymeric foam to be suitable for various applications – 1) good insulation: the low thermal conductivity of polymeric foams provides them an excellent insulator for a wide range of applications such as building insulation and thermal packaging, 2) lightweight: polymeric foams are lighter than non-foamed polymer, allowing for their ease of handling and transport, good shock absorption: as a consequence of their cellular structure, they exhibit excellent shock-absorbing properties, which make them useful for cushioning and protecting fragile items during transport, and 3) versatility: they can be formulated to have different physical and mechanical properties, and thus have wide applications from a seating cushion to packaging material. In addition to these applications, the large surface area of polymeric foam makes it an effective oil sorbent material because of its large number of sites for oil absorption. The foam's cellular structure creates many small voids that can trap and hold onto the oil, which results in a high degree of sorption. Due to its lightweight and low-density properties, the material is highly effective for ab/adsorbing oil as it floats on the surface, allowing it to contain and prevent the spread of the oil [35].

Polymer materials mainly used for the foaming process are thermoplastics and thermoplastic elastomers, due to their good melt-processibility under heated conditions. Thermoplastics (TPs) have the ability to be repeatedly melted and molded without undergoing significant changes in chemical structure, so TP foams can be melted, expanded, and solidified multiple times without losing their foam structure. Also, TPs have good gas permeability, allowing them to trap a large amount of gas within their structure during the foaming process. Thermoplastic elastomers (TPEs) are a relatively new class of copolymers that display a unique combination of properties from both thermoplastics and elastomers [36]. These polymers incorporate the processing ease of thermoplastics, combined with the stretchability and rigidity of elastomer. TP and TPE foams are employed in various applications, among which TP foams investigated for the oil sorption purpose include polyethylene, polypropylene, thermoplastic polyurethane [37–39], poly(lactic acid) [40,41], polycarbonate, and polystyrene foams, and TPE foams include ethylene propylene diene monomer (EPDM) [30] and ethylene vinyl acetate (EVA) based foams [42].

2.1.1. Basic classification/characterization of foam

The structure of foams can vary depending on the level of expansion and specific formulation. A general characterization of foam should consider a combination of the following factors.

1) Cell size: Cell size, which is a crucial property of foams, can be measured by counting the number of cells intersecting a specific length, as described in ASTM D3576. Microcellular and nanocellular foams are characterized by their mean cell size and cell density. Microcellular foams have a mean cell size of less than 10 μm and cell density of between 109 and 1012 cells/cm^3, while nanocellular foams have a mean cell size of less than 1 μm and cell densities greater than 1015

cells/cm^3 [43–45]. The variation in cell sizes in foams is due to both random nucleation and growth of cells through the diffusion of gas from smaller to larger cells. This process leads to an unstable structure, characterized by a non-uniform cell size distribution. Equation (2.1) describes the pressure inside a bubble surrounded by molten (or softened) polymer, which explains the mechanism of gas diffusion [46,47].

$$\Delta P = \frac{2\alpha}{r} \tag{2.1}$$

Where ΔP is a pressure difference between gas and molten polymer, α is surface tension, and r is a radius of a spherical bubble.

2) Cell structure:

Microcellular foams can be further classified into closed-cell, partially open-cell, and open-cell. Closed-cell foams have open-cell content below 10 vol% and open-cell foams have an open-cell content above 90 vol%. **Fig. 2.1** describes the open-cell and closed-cell structures of polymeric foams. It is important to consider cell morphology and open-cell content in determining the properties and applications of polymer foams. Open-cell foams have broken cells that allow air to occupy the spaces within, making them lightweight, less dense, and have a soft, sponge-like appearance. On the contrary, closed-cell foams have intact cells and are dense and they are commonly used for heat and sound insulation. For specific applications, such as oil sorption, it is crucial for the sorbent to have an optimal open-cell ratio, as a high open-cell content enhances water permeation, but excessive open-cell content can break down the foam structure.

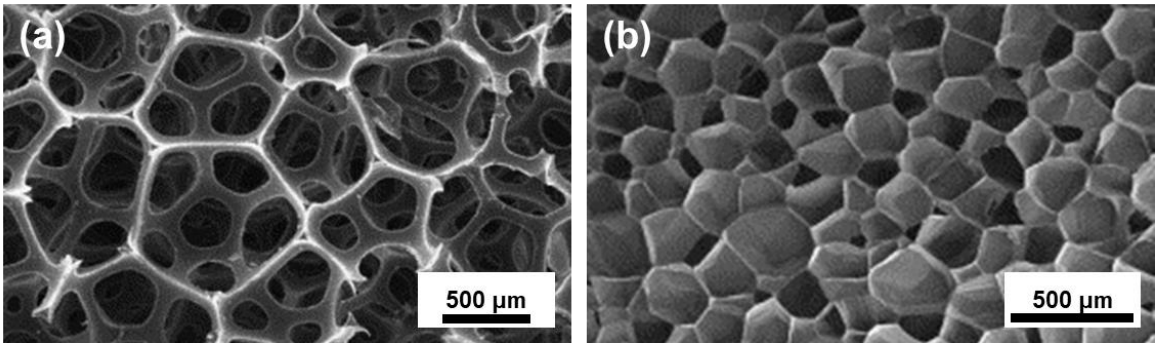

Fig. 2.1. (a) Open-cell [48] and (b) closed-cell [49]structures of polymeric foams (Reproduced with permission from [48] and [49]. Copyright 2004 and 2005 Elsevier Inc.)

3) Expansion ratio: Expansion ratio refers to the relative increase in the volume of a polymer foam during the foaming process, and is expressed as Equation (2.2)

$$\phi = \frac{\rho_1}{\rho_2} \tag{2.2}$$

Where ϕ is an expansion ratio and ρ_1 and ρ_2 are densities of the polymer before and after foaming. The expansion ratio is an important parameter that can affect the final properties of the foam, such as cell size, cell density, and mechanical properties. For example, a higher expansion ratio results in a foam with larger cell sizes and lower cell density, while a lower expansion ratio results in a foam with smaller cell sizes and higher cell density. The expansion ratio can be controlled by adjusting the conditions of the foaming process, such as temperature, pressure, and chemical composition.

2.1.2. The procedure of cell formation

The formation of foam involves the creation and expansion of gas bubbles in a polymer matrix. This results in a system of dense polymer matrix with spherical pores filled with gas. The

transformation of a foaming agent from free gas molecules to spherical bubbles occurs with the rapid change of temperature and pressure, causing a reaction in the polymer system [50]. When the polymer matrix surrounding the gas bubbles solidifies quickly enough before the gas condenses, the foam becomes stable. It is crucial that this solidification process happens faster than the gas phase condensation, as otherwise, the size of gas bubbles reduces, causing the shrinkage of the polymer foam [51]. **Fig. 2.2** describes the general foaming process in four stages. 1) Gas diffusion, 2) Cell nucleation, 3) Cell growth, and 4) Cell stabilization.

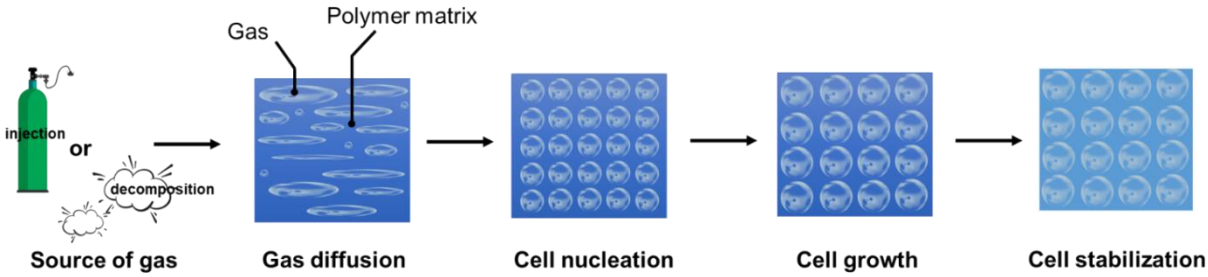

Fig. 2.2. Cell formation procedure of polymeric foam.

1) Gas diffusion: a pressured gas is injected into a molten polymer (for physical foaming) or a decomposed gas from a chemical reaction is introduced to a molten polymer (for chemical foaming). The gas diffuses throughout the molten polymer until saturation is reached.

2) Cell nucleation: The formation of microcellular nuclei starts with the addition of gas to a saturated polymer/gas mixture, causing gas to escape from the single-phase polymer/gas mixture and form the cell nucleus. The thermodynamic change, a driving force of the cell nucleation, is often brought about by a decrease in the

solubility of the gas, which can be achieved through a pressure drop or a temperature increase [52]. If the foaming process involves rapid depressurization, the cell nucleation and the cell growth occur simultaneously, as the escaping gases within the polymer system swiftly expand to create larger cells. The relationship between solubility and pressure is an important factor in the foaming process as this stage influences the final shape and characteristics of the material.

3) Cell growth: Cell nucleation results in the creation of cells with varying sizes. The pressure within a small cell is higher compared to larger cells, causing the smaller cells to coalesce with the larger cells through a pressure gradient. This, in turn, contributes to the expansion of the cells. The cell growth is dependent on various factors, such as the temperature, pressure, and viscoelastic properties of the polymer/gas mixture during the processing.

4) Cell stabilization: The solidification of the molten polymer occurs through cooling or the use of surfactants. Once solidification takes place, the gas inside the cells gradually diffuses out, making room for air to enter. The mutual diffusion between gas and air continues until the gas has completely been replaced by air, leading to cell stabilization.

2.1.3. Foaming agent

Foaming agents are integral components in the fabrication of polymeric foamed, possessing lightness, thermal insulation, and cost-effectiveness [53]. These additives facilitate the formation

of fine and uniform pores within the polymer, leading to a diverse range of foaming applications from rigid thermoset resins to easily softening thermoplastics. Apart from polyurethane foam, which employs water to react with isocyanate to release CO_2 gas for the foaming, foaming agents are often divided into two categories: physical and chemical foaming agents.

2.1.3.1. Physical foaming agent

Physical foaming agents (PFA) function by undergoing a change in their physical state, which involves the vaporization of liquid or depressurization of gas bubbles embedded in the polymer system [54]. PFAs that create foaming expansion through liquid vaporization include water, short-chain hydrocarbons, and halogenated hydrocarbons, and PFAs that create foam by undergoing depressurization are relatively inert gases such as CO_2 and N_2 [55]. Nowadays, CO_2 and N_2 are highly regarded as effective foaming agents for their eco-friendliness, cost-efficiency, foamability, and safety.

The relatively low critical temperature and pressure of CO_2 and N_2 make them easy to enter the supercritical state, enabling them to serve as highly effective foaming agents. A supercritical state is a state of matter that occurs when a substance is maintained at a certain point of temperature and pressure above its critical temperature and pressure. In this state, the substance has properties of both a liquid and a gas, with high fluidity and low surface tension. Therefore, the solubility of CO_2 and N2 in this state increases significantly in the polymer system and this results in a decrease in the glass transition temperature of most polymers. When a molten polymer is saturated with a supercritical fluid, cell nucleation takes place at a high concentration, and cell growth persists until the polymer solidifies. This makes it beneficial to fine-adjust the size of the pores from nano to

macroscale. Furthermore, the modest critical temperature and pressure of CO_2 (31.1 ℃ and 7.38 MPa) make the rapid depressurization step relatively easier for the polymer foaming without requiring a high processing temperature [46].

However, the major challenge of physical foaming is the volume shrinkage of the polymeric foam, especially for elastomers [56,57]. Unlike thermoplastics, TPEs are difficult to foam with large expansion due to their elasticity and low modulus. During the foaming process, gas bubbles are entrapped in the TPEs to create pores within the polymer matrix. However, once TPEs are exposed to ambient temperature and pressure after the foaming process, they become elastic and lack the necessary modulus to withstand the compressive force from the air. As the air pressure is higher than the gas pressure within the polymer, the gas bubbles shrink by the compressive force, and it restricts the foaming expansion [34]. To enhance the modulus of TPEs and mitigate the issue of volume shrinkage, the use of rigid fillers, such as silicate, carbon fiber, and carbon black has been studied [58]. Also, crosslinking (or vulcanization) is an effective way to increase the modulus of the polymer, which involves the formation of covalent bonds between polymer chains and creates an interconnected structure. In the physical foaming method, crosslinking must take place prior to the foaming process. However, this pre-crosslinking often impedes cell growth and restrains foam expansion due to TPEs' enhanced rigidity [34]. In this case, utilizing a chemical foaming agent can facilitate the process.

2.1.3.2. Chemical foaming agent

Chemical foaming agents (CFAs) are thermally decomposable foaming agents that turn into gas when heated. They are mostly solid at room temperature but when exposed to the heat of a specific

temperature (above decomposition temperature), they decompose and release a gas such as N_2, CO_2, or CO. The process of using a CFA involves blending, heating, expansion, and solidification. A blend of the polymer material and the CFA is prepared, and then it is heated under pressure. The heat fluidizes the polymer, causing the foaming agent to release gas through a chemical reaction, and forming cells within the fluid polymer. The polymer/gas mixture is then placed into a mold where the gas expands, resulting in the polymer expanding and forming the desired shape. The mold is then cooled, allowing the polymer to solidify and maintain the cell structure created during the foaming process.

CFAs can be largely classified into two groups: exothermic and endothermic chemical foaming [59,60]. Exothermic CFAs generate a large amount of heat when they decompose and cause an exothermic chemical reaction. They are usually organic compounds such as azodicarbonamide (ADC), p-Toluenesulfonyl hydrazide (TSH), and 4,4'-Oxybis(benzenesulfonyl hydrazide) (OBSH). Endothermic CFAs, on the other hand, absorb heat when they decompose, causing an endothermic reaction. Examples of endothermic foaming agents include inorganic salts such as sodium bicarbonate and ammonium sulfate.

One of the main advantages of CFAs is their ability to create a uniform foam structure. This allows manufacturers to produce consistently sized and shaped foams. Also, using CFAs is cost-effective, because most CFAs are much less expensive than other foaming agents, and it reduces the cost of installation as it requires simple incorporation into existing thermoplastic processing equipment. CFAs can be added to a solid polymer before heating, whereas PFAs require the polymer to be already molten (or softened) before they can be injected. This makes CFAs advantageous to use

in a variety of processing methods such as compression, injection molding, extrusion, and calendering without requiring special storage or handling [61].

Moreover, the chemical foaming method addresses the volume shrinkage issue of the physical foaming method on TPEs. As mentioned, improving the modulus of elastomers requires additional modulus enhancement treatment such as crosslinking. In the physical foaming process, crosslinking must be done before the foaming process, but this pre-crosslinked network often inhibits foam expansion. On the other hand, chemical foaming allows crosslinking and foaming to happen simultaneously, therefore it can benefit from the crosslinking with the enhanced melt strength that maintains the foam structure thus minimizing post-shrinkage and improving the elastomers' dimensional stability [34].

Despite their many advantages, there are disadvantages to using chemical foaming agents. When using these foaming agents, it is important to pay close attention to the foaming agent's decomposition temperature, as the polymer can decompose before the foaming agent is fully activated. Additionally, CFAs can cause contamination if unreacted or solid residue stays in the product. This residue can lead to discoloration, odor, and corrosion of the polymer. Also, the gases released by the foaming agent such as NO_x, SO_x, and a large amount of CO_2 can cause environmental pollution, therefore, it is important to use adequate concentrations of CFAs to minimize the problem.

2.1.3 Methods of preparation for polymeric foams

2.1.3.1 Extrusion foaming

Extrusion foaming is a process where a foaming agent (gas) is injected into the molten polymer through an extruder. The gas is introduced into the polymer through either the thermal decomposition of a chemical foaming agent or the direct injection of a physical foaming agent, with the principles being similar for both methods. Rizvi et al. [62] presented extrusion foaming of PP/PTFE blends using a physical foaming agent (CO_2) in two-step single-screw extruders (**Fig. 2.3**). The solid polymer (usually pellet or powder form) is fed through the hopper and the polymer becomes a completely molten state as it passes the heated screw where shear heating is generated by the screw motion. CO_2 is then introduced into the first single-screw extruder barrel through a syringe pump, ensuring a constant flow rate. The rotating screw inside the barrel creates high shear and high pressure, facilitating the dissolution of CO_2 in the molten polymer through convective diffusion. It is crucial to maintain high pressure throughout the extruder and die to delay bubble nucleation until the polymer emerges from the die. Upon exiting the die, the molten polymer experiences a sudden pressure drop, leading to supersaturation with gas. This phenomenon triggers the nucleation and formation of bubbles within the material. The foam structure stabilizes as it rapidly cools down.

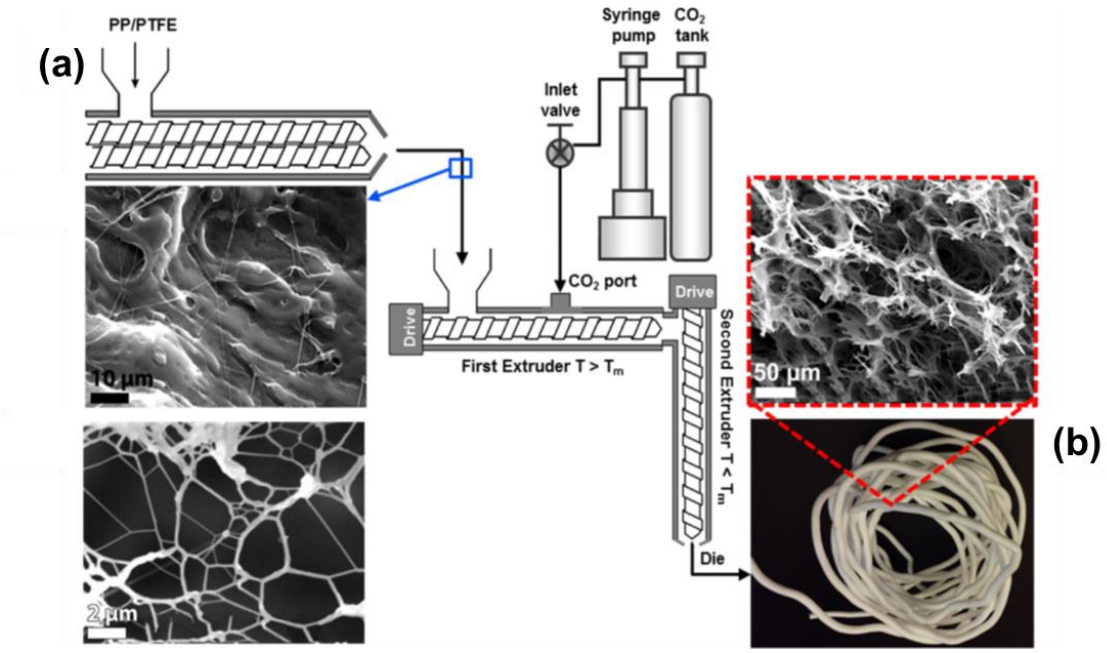

Fig. 2.3. Extrusion foaming of PP/PTFE fibrillar blends: (a) PP-homopolymer blended with PTFE in a twin-screw extruder; (b) images of an open-cell foam filament produced via extrusion. (Reproduced with permission from [62]. Copyright 2014 American Chemical Society.)

2.1.3.2. Batch foaming

The production of elastomeric foam through batch physical foaming can be classified into two methods based on how pressure and temperature are controlled [63]. The first method, heating foaming, involves saturating the elastomer with foaming agents at low pressure and temperature, then expanding the gas-saturated elastomer at a higher temperature for a set amount of time. The second method, cooling foaming, involves first heating and melting the elastomer with foaming agents at high pressure and temperature, then cooling it down to the foaming temperature and expanding it by releasing the pressure. **Fig. 2.4** shows a batch foaming system with a cooling

foaming method [64]. The foamed polymer was a chain-extended polylactide and CO_2 was used as a foaming agent. The maximum processing temperature and pressure in the autoclave were 350 ℃ and 200 bars respectively, and the pressure was rapidly dropped (at the rate of 20 $bars^{-1}$) for the foam expansion.

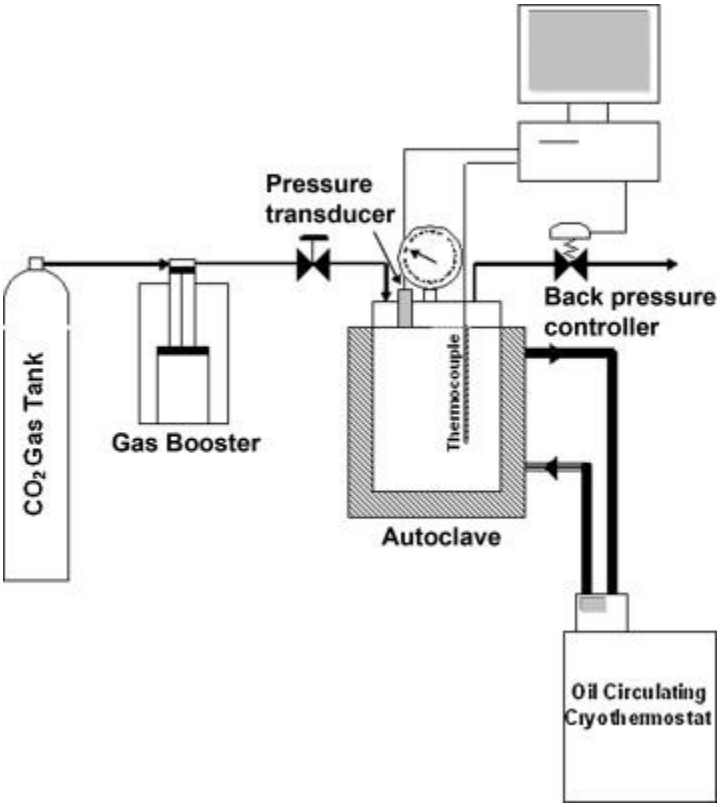

Fig. 2.4. Batch foaming equipment. (Reproduced with permission from [64]. Copyright 2011 Elsevier Inc.)

2.1.3.3. Foam injection molding

Foam injection molding is a quick and economical method of producing foam products with consistent and uniform characteristics. It grants a level of precision in the molding process, such

as the amount of material used, the foam density, and the product's shape. Additionally, it requires minimal tooling and results in low scrap rates.

Hopmann et al. [65] conducted a foam injection molding of ethylene propylene diene monomer (EPDM) using water as a foaming agent, to determine that water vaporization can replace the chemical decomposition foaming method for a TPE. The EPDM samples were made using the breathing mold technique as shown in **Fig. 2.5**. This technique involves the injection of the melt into a compression mold, followed by a residual time of 100 s and the opening of the mold by 2 mm. The opening initiates foaming, after which the sample is demolded. The main benefit of this concept is the controlled foaming after a set time and temperature. The pressure within the cavity increases due to thermal expansion, preventing premature foaming until the mold is opened. The injection was carried out with a mold temperature of 180 – 210 °C and a maximum injection pressure of 75 bar.

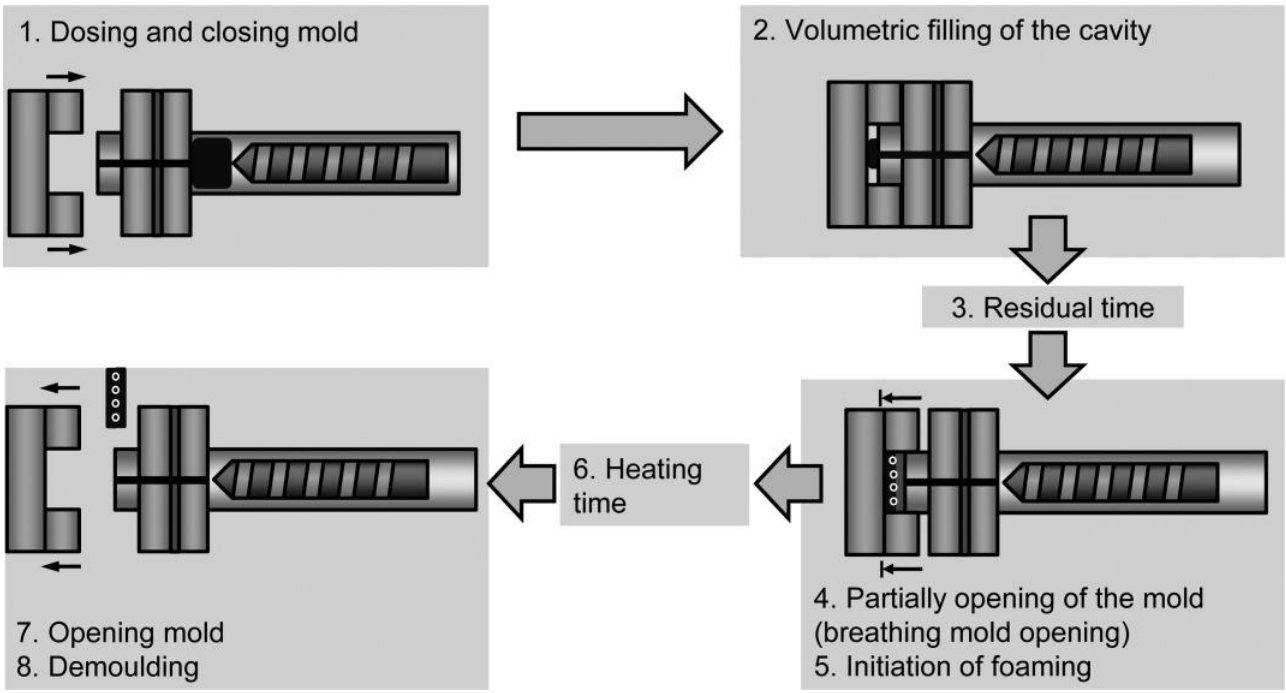

Fig. 2.5. Process sequence of the breathing mold technique in injection molding. (Reproduced with permission from [65]. Copyright 2016 John Wiley & Sons, Inc.)

2.1.4. Foam rheology

The viscoelastic properties of the polymer melt have a major impact on its foaming behavior. When the foam is expanded, a certain amount of pressure is applied to it. The melt strength is a viscoelastic measure of how much pressure the polymer can withstand before deformation begins. The melt strength is dependent on the polymer's molecular weight, molecular weight distribution, and other rheological properties. Enhancing the melt strength of a molten polymer can benefit cell nucleation and structure refinement, reduce gas loss during foaming and prevent cell collapse and foam shrinkage [66,67]. This leads to higher expansion ratios and improved cell morphology.

The relation between polymer rheology and foaming expansion was explained in the work of Li et al. [68]. They fabricated poly (lactic acid) (PLA) foam with a high expansion ratio, using a pre-isothermal treatment, which endowed PLA with high crystallinity and a refined crystalline structure. **Fig. 2.6** presents the rheological properties and the expansion ratio of two different types of PLA ("Non-Iso" represents non-pre-isothermal treated PLA and "Iso" indicates pre-isothermal treated PLA). The results presented in **Fig. 2.6 (a)** demonstrate that the storage modulus (G′) of Iso-PLA was significantly higher than Non-Iso-PLA across the entire frequency range, indicating that Iso-PLA possessed increased melt elasticity of the material. Also, Non-Iso-PLA showed a behavior of viscoelastic liquid as $\tan\delta$ (viscous/elastic ratio) decreased with an increase in frequency (ω), while Iso-PLA showed a solid-like behavior as $\tan\delta$ increased with an increase in frequency (**Fig. 2.6 (b)**). The observations made in the study provided evidence that the pre-isothermal treatment led to an increase in the crystallinity of PLA, which in turn resulted in an improvement in the melt strength of the material.

The expansion ratio of PLA foam was investigated as shown in **Fig. 2.6 (c)** and **(d)**. They used a supercritical CO_2 foaming method to produce the PLA foam and varied the pre-isothermal treatment condition, as well as the foaming temperature and pressure. It was observed that the Iso-PLA foam had notably higher expansion ratios compared to Non-Iso-PLA foam, across almost all the tested temperatures, under both the saturation pressure of 24.1 MPa and 31.0 MPa. Therefore, the study found that the pre-isothermal treatment could significantly increase the expansion ratio of the PLA foam, by enhancing the melt strength of the polymer through crystallization.

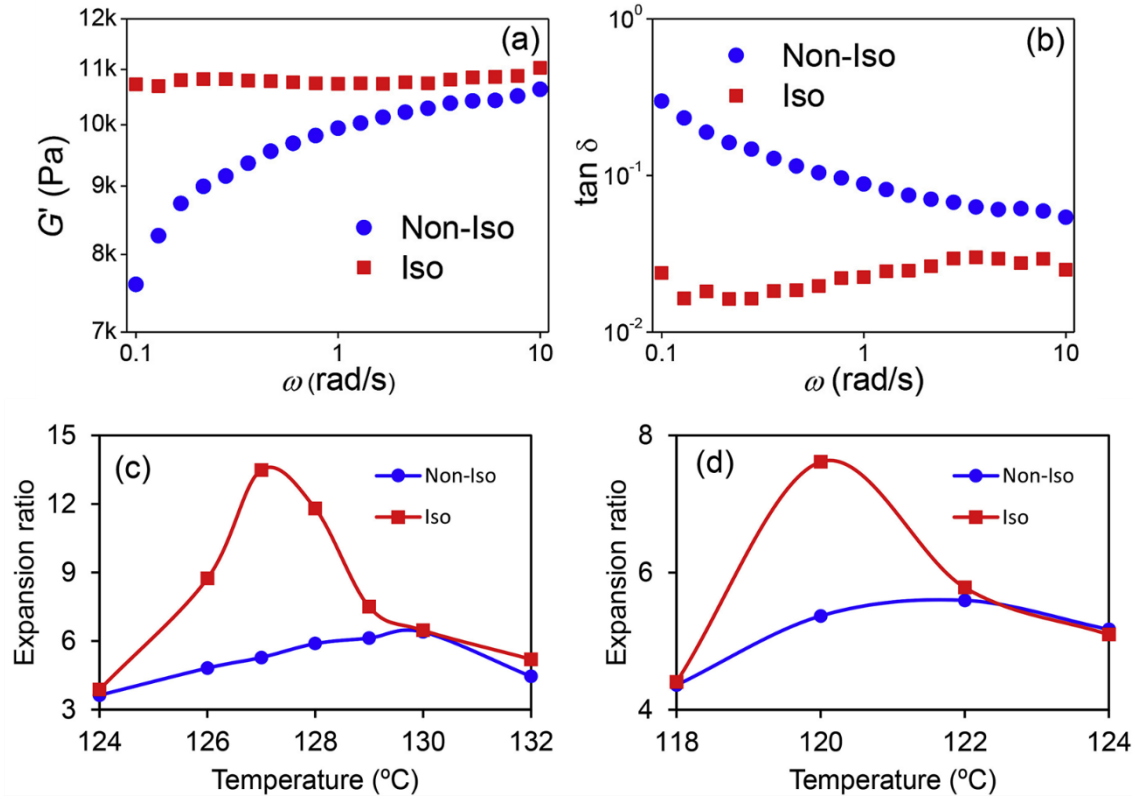

Fig. 2.6. The rheology of Non-Iso and Iso PLAs: (a) the storage modulus (G′) and (b) tan δ and the expansion ratio of Non-Iso and Iso PLA foams under the saturation pressure at (c) 24.1 MPa and (d) 31.0 MPa. (Reproduced with permission from [68]. Copyright 2018 Elsevier Inc.)

2.1.5. Oil sorption and separation mechanism of polymer foam

Polymer foam is a physical sorbent that possesses a remarkable oil-spill cleanup ability, which minimizes environmental damage at an inexpensive cost. Sorbents remove the oil with typically two mechanisms: Adsorption and absorption. Adsorption involves the adhesion of atoms, ions, or molecules from a gas, liquid, or dissolved solid to the surface of a material, and is a surface-based phenomenon driven by physical forces. Absorption, on the other hand, involves the diffusion of

the absorbate throughout the absorbent's body, including the surface and interface. It involves both physical and chemical forces.

Polymeric foams are an effective material for oil/water separation due to their hydrophobic and oleophilic properties, which allow them to selectively ab/adsorb oil while permitting water to pass through the vacant voids in the polymer. This absorption process occurs without dissolving the foam and is further enhanced by capillary action - the tendency of liquids to be drawn into the small spaces between cell walls in the polymer [69]. This mechanism of oil absorption is described by the surface tension equation (Equation (2.3))

$$\gamma = \frac{F}{2L} \tag{2.3}$$

Where γ is the surface tension, F is the force of attraction between molecules, and L is the length of the interface between the liquid and solid. **Fig. 2.7** exhibits the oil/water separation of polymeric foam and the capillary action through cell walls within the polymer. The capillary action of the foam enables it to absorb higher volumes of oil than other materials, making it an ideal material for oil recovery. Furthermore, the larger expansion of the foam has increased surface area (higher interface length and thinner cell wall), which allows for an improved spread of oil throughout the polymer body, resulting in an even greater oil uptake ability.

Adsorption and absorption processes effectively remove oil without dissolving the polymer sorbent. On the other hand, gelation is another method that involves dissolving the polymer sorbent. Polymer sorbents that employ gelation interact with oil when they come into contact, dissolving the polymer to form a gel that selectively removes oil from oil-water mixtures. The chemical

compounds responsible for the gelation process are commonly known as organogelators. Organogelators used in oil spill cleanups primarily include low molecular weight substances like amino acid-, fatty acid-, and sugar alcohol-based gelators [70,71]. However, a number of studies have reported the use of high molecular weight polymers for selective gelation of hydrocarbon oil [72–74]. The gelation process is driven by non-covalent interactions such as hydrogen bonding, π–π stacking, and van der Waals forces, without involving a chemical reaction [74].

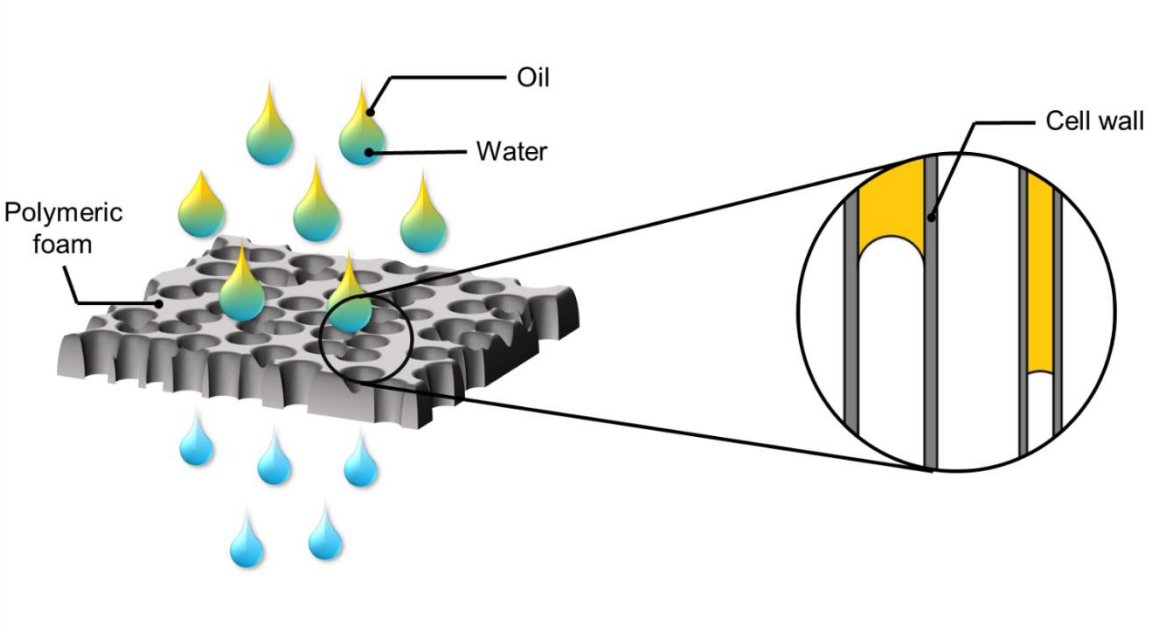

Fig. 2.7. Oil/Water separation of polymeric foam and capillary action within the polymer.

2.1.6. Recent progress of polymeric foam

2.1.6.1. Nanocomposite polyurethane foam

Polyurethane foams have been one of the major research topics as effective oil-absorbent materials due to the combination of desirable properties such as ease of modification, processibility,

recyclability, high oil absorption capacity, and exceptional mechanical strength. Furthermore, they can be easily fabricated on a large industrial scale thus they have become a promising candidate for oil and organic solvent absorption.

However, the polar groups present in polyurethane, such as carboxyl and amino groups, make these materials hydrophilic and therefore reduce their selectivity and overall performance in oil/water separation processes. To address this issue, recent studies have focused on surface modification of polyurethane foam to achieve hydrophobic surfaces, which would increase the oil/water selectivity. Various materials have been used for this purpose, including Al_2O_3 [75], ZnO [76], SiO_2/MnO_2 [77], lauryl methacrylate [78], and carbon-based materials [79–81]. Among the materials used for the hydrophobic functionalization of polyurethane sponges, carbon-based composites such as nanotubes, nanofibers, nanoparticles, and graphene (2D nanocarbon) have proven to be effective as fillers in polyurethane foam. These fillers not only increase the hydrophobicity of the foam but also improve its overall performance.

Keshavarz et al. [82] studied multi-walled carbon nanotube (MWCNT) modified polyurethane foam (PUF) and the results showed that the addition of MWCNTs on PUF surface improved its thermal and mechanical resistance and increased its light crude oil sorption capacity by 21.44 % at a concentration of 1 wt. % MWCNT. The sorbent's reusability was also tested through four cycles of chemical regeneration and 85.45% of its initial oil sorption capacity remained after regeneration. Another noticeable work of MWCNT-incorporated PUF material was reported by He et al. [80]. Their work indicated that the modified foam has a high water contact angle of 159 ° and an improved oil absorption of up to 60 g/g. It was confirmed to be highly effective and reusable

(900 cycles) in various oil/organic-water systems such as engine oil, silicone oil, and kerosene. Also, the modified materials showed 27 % higher tensile strain and 35 % lower compressive strain compared with regular polyurethanes, indicating they possessed enhanced mechanical properties and larger foam expansion.

Visco et al. [83] investigated polyurethane-based foams filled with carbon nanofibers (CNF) to enhance their oil selectivity and mechanical durability. The samples were characterized through various physical and mechanical tests, including contact angle measurement, absorption tests, optical microscopy observation, and compression fatigue tests. The results showed that the addition of CNF to the foam led to an increased hydrophobicity (contact angle of 111-114 °) and a better oil separation (22.85 % improvement in oil/water selectivity compared to a non-modified PUF). The optimal filler amount was found to be around 1 wt% for a homogeneous distribution within the foam. Furthermore, the fatigue test results showed that the mechanical properties of the foam improved with increasing amounts of carbon filler, leading to greater resistance to fatigue and increased elasticity.

The study of Anju et al. [84] presented a novel Graphene-meso Iron Oxide composite incorporated Polyurethane foam (GPUF) as a highly efficient sorbent for organic contaminants and oils. The foam's surface was modified by anchoring the Graphene-meso Iron Oxide composite, which endowed high porosity, increased hydrophobicity, and great magnetic properties to the polyurethane foam. The effectiveness of the GPUF was demonstrated by its ability to remove oils rapidly and selectively from water using a magnetic field, while its magnetic properties also enabled it to be easily directed to specific areas and quickly recollected after use. The 3D porous

polyurethane scaffold and Graphene-mesoporous Iron oxide composite were found to have a cooperative effect on the adsorption dynamics, leading to selective adsorption capacity for a wide variety of oils and organic pollutants in the range of 90–316 g/g. The GPUF was also easily recoverable by manual squeezing, with the reusability of over 150 cycles (for chloroform) and maintained its high adsorption capacity (**Fig. 2.8**).

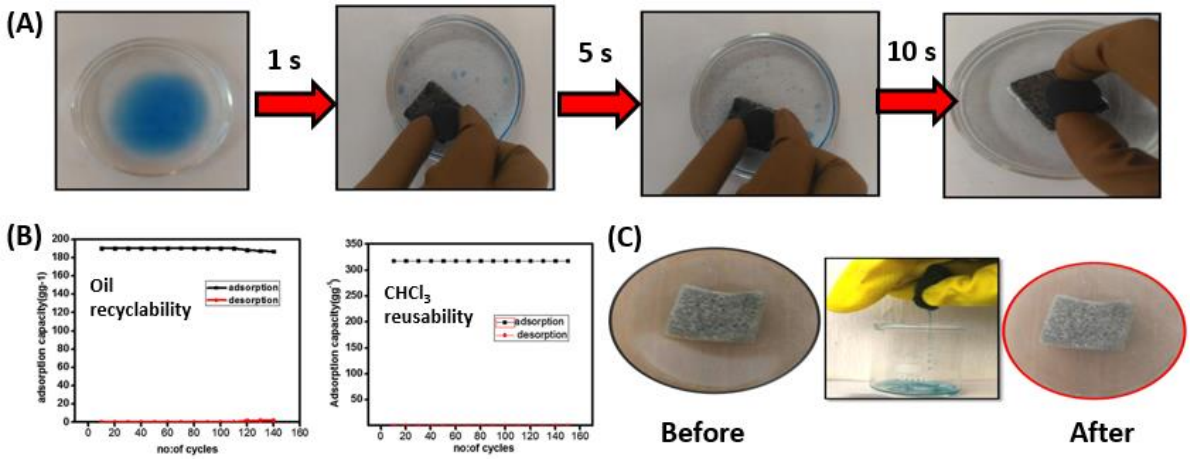

Fig. 2.8. (A) Oil removal by magnetically driven GPUF over time; (B) Adsorption capacity of GPUF in cycles of adsorption and desorption of diesel oil and chloroform; (C) Digital images of GPUF before and after reusability studies using diesel oil. (Reproduced with permission from [84]. Copyright 2020 Elsevier Inc.)

2.1.6.2. Biodegradable polymer-based foam for the oil sorption

The extensive use of conventional petroleum-derived polymers led to significant consumption of non-renewable resources and the production of large amounts of difficult-to-degrade plastic waste, resulting in severe environmental pollution. This contradicts the goals of sustainable development

and the primary purpose of oil-water separation, which is to conserve energy and safeguard the environment. As a result, there is growing interest in oil-ab/adsorbing polymeric foam made from bio-based and biodegradable substances.

Poly(lactic acid) (PLA) is among the most extensively studied biodegradable polymers. PLA foam with an open-cell structure and high expansion ratio possesses a 3D structure with a large specific surface area and increased porosity, which provides high buoyancy in the water and efficient oil sorption [85,86]. With its strong oleophilicity and hydrophobicity, PLA serves as an excellent material for oil absorption. Moreover, the porous nature of PLA foam allows for easier degradation compared to solid PLA.

Polyvinyl alcohol (PVA) is an affordable, non-toxic, and biocompatible polymer that has attracted significant interest due to its ease of fabrication, biodegradability, and suitability for environmental remediation [87]. PVA foam, with its high porosity and low density, exhibits outstanding adsorption performance and the durability of PVA-based foam is essential for sustained oil-water separation applications [88]. However, the hydrophilicity of PVA foam limits its application in oil-water separation [89]. This issue can be addressed by incorporating nanocomposite often through surface modification. Pristine PVA foam typically contains numerous hydroxyl groups, which enable active site reactions with nanoparticles, resulting in hierarchical structures on the PVA foam's framework [90].

Table 2.1 exhibits the studies of biocompatible polymer-based foams designed for oil sorption applications. Wang S et al. [86] and Li et al. [91] successfully created PLA foam and PLA/PBS foam, respectively, employing the supercritical CO_2 foaming method. Both PLA-based foams

exhibited great recyclability for CCl_4. In **Table 2.1**, the recyclability item indicates the tested number of sorption and desorption cycles during which the foam preserved its structural integrity and oil sorption capacity. Wang X et al. [92] employed a water-assisted thermal phase separation to prepare superhydrophobic PLA foam in a simple and facile method, which showed great sorption capacity at around 12 – 31 g/g. Gao et al. [87] combined porous boron nitride nanofibers (BNNFs) with PVA to create a composite foam using a freeze-drying method. An increase in BNNFs content resulted in a larger specific surface area and significantly increased oil sorption capacity. Jin et al. [93] fabricated a PVA-based porous gel with a surface acoustic wave (SAW) microfluid generation method, which allowed for improved control and flexibility in manipulating the microfluid. He et al. [90] prepared superhydrophobic and superoleophilic TiO_2/PVA foam by anchoring TiO_2 to the surface of PVA foam with chemical modification. For other biomass-derived foam modification, Lorevice et al. [94] fabricated cellulose nanofibrils (CNFs) based foam incorporated with natural rubber (NR), and Hwang et al. [95] created PU foam combined with hydrophobized lignin particles, which both showed great reusability.

Table 2.1. Biocompatible polymer foams developed for oil-absorbing application.

Type	Material	Fabrication method	Type of oil/solvent	sorption capacity (g/g)	Reusability (cycle)	Reference
PLA	PLA foam	sc CO_2 foaming	CCl_4, ethyl acetate, N-octane, etc.	4.6 - 15.1	20 (CCl_4)	Wang S et al. [86]
	PLA/PBS foam	sc CO_2 foaming	CCl_4, ethyl acetate, silicone oil, etc.	7.9 - 21.9	20 (CCl_4)	Li et al. [91]
	PLA foam	water-induced phase separation and freeze-drying	Engine oil, silicone oil, cyclohexane, etc.	around 12 - 31	10 (ethanol and cyclohexane)	Wang X et al. [92]
PVA	BNNFs/PVA foam	freeze-drying	silicone oil and pump oil	19.8 – 61.1	-	Gao et al. [87]
	PVA-based porous gel	SAW-induced bubble generation and freeze-drying	fluorocarbon solvent/oil and silicon oil	around 4 - 8	10 (fluorocarbon oil)	Jin et al. [93]
	TiO_2/PVA foam	PVA modification with TiO_2 anchoring	PEG, CCl_4, ethanol, etc.	4.3 - 13.6	15 (n-hexane and CCl_4)	He et al. [90]
other biopolymers	NR/CNF foam	CNF modification with NR anchoring	Diesel, pump oil, silicone oil, etc.	around 40 (silicone and pump oil)	20 (THF, Chloroform, and Toluene)	Lorevice et al. [94]
	lignin/PU foam	lignin modification with PUF	crude oil, olive oil, pump oil, etc.	around 6 - 9	50 (crude oil and olive oil)	Hwang et al. [95]

2.2. Melt-blown fibers

2.2.1. Role of melt-blown fibers

Melt-blowing is a manufacturing process used to produce fine fibers from thermoplastic resins. The process involves melting a polymer resin and then extruding it through small nozzles, where high-velocity fluid, typically air, is blown through the nozzles to break up the polymer stream into tiny droplets [96]. These droplets then solidify into fibers as they come into contact with a conveyor or take-up screen [97]. The resulting fibered web is self-bonded, so the fibers stick together without the need for adhesives. The fibers produced by the melt-blowing process are typically very fine, with diameters ranging from micro- to nanometers.

The melt-blowing process is applied in various fields, including automotive components, filtration, thermal insulation, geotextiles, drug delivery systems, and garments [98,99]. The resulting fibered web can be used as a filter medium in the air or liquid filtration systems, as the small fiber diameters provide a high surface area, which increases filtration efficiency [100]. Melt-blowing can also be used to produce non-woven fabrics for use in clothing and protective gear, as well as in medical applications like wound dressings and surgical masks [101,102]. Melt-blown fibers have also been found to be effective in oil sorption due to their hydrophobic nature and porous structure. In producing melt-blown fibers, the use of hydrophobic polymers like polypropylene can result in a membrane that repels water due to its low-surface-energy fibers with varying diameters. The rough and porous structure created by these interwoven fibers allows for the selective permeation of oil instead of water [103]. This property is useful in oil spill cleanup, where

melt-blown fibers can be used to ab/adsorb to contain spilled oil and/or filter the contaminated water.

The melt-blowing process depends on the spin head that extrudes the molten polymer through a row of closely spaced fine holes. The polymer stream is then blown apart into fine fibers by high-velocity fluid and drawn onto a collector to form a self-bonded web [104]. The melt-blowing method is an appealing choice for generating fine fibers on an industrial scale since it is a quite straightforward process and provides high specific productivity [105].

2.2.2. Melt-spinning and Melt-blowing.

Melt-spinning and melt-blowing are two common techniques used to produce fibers from polymer materials. Although they share similarities, there are some differences in the process of fiber formation.

Melt spinning is a process in which polymer resin is melted and extruded through a spinneret to form a fiber. The spinneret contains numerous holes or orifices, and the extrusion process produces continuous filaments. The diameters of the fibers produced in melt spinning can be varied by adjusting the size of the orifices in the spinneret [106].

Melt-blowing, on the other hand, is a one-step process in which the molten polymer is blown into ultrafine fibers by hot, high-velocity air. The fiber is then collected on a rotary drum or a forming belt with a vacuum underneath the surface to form a non-woven web. In melt-blowing, the die assembly is different from the melt-spinning process, as hot air converges with the fiber as it emerges from the die [107]. The fibers produced in melt-blowing are typically smaller in diameter

typically ranging from 1 to 10 μm, which allows melt-blown fibers to have superior filtration properties, while conventional melt-spun fibers have a coarser fiber structure, higher tensile strength, and lower pressure drop [108]. The diameters of the fibers produced in melt-blowing can be varied by adjusting the air pressure, temperature, and distance between the die and the collector.

2.2.3. Melt-blowing process

In the present day, there exists a multitude of designs for melt-blowing processes, yet a set of fundamental components is commonly shared among the majority of such processes. These components include 1) polymer feed, 2) a metering pump system, 3) die assembly, 4) air assembly, and 5) fiber collection and a winding system [109]. The schematic diagram of melt-blowing is described in **Fig. 2.9**.

The extrusion process begins by feeding the polymer pellets or granules into the extruder hopper, where they are conveyed along the hot walls of the barrel between the screw flights. As the polymer flows through the barrel, it becomes molten due to the combined effects of high temperature, friction, and shear heating as the screw rotates inside the barrel. The molten polymer is then pushed towards the metering zone, which applies the greatest pressure during the extrusion process. This high-pressure molten polymer is regulated by a breaker plate with a screen pack that is positioned near the screw discharge. The molten polymer is then transferred to the metering pump which precisely controls the flow rate of the molten polymer, which is essential for creating uniform fibers. The metering pump works by measuring and delivering a fixed volume of polymer melt per unit of time and ensures consistent polymer flow under process variations in viscosity and temperature. The most crucial component of the melt-blowing process is the die assembly, which

comprises three essential parts: polymer feed distribution, die nosepiece, and air manifolds [110]. The polymer feed distribution is designed in a way that polymer distribution is not heavily influenced by the shear properties of the polymer, allowing for the melt blowing of a wide range of polymeric materials with one distribution system. Once the polymer melt exits the feed distribution channel, it directly flows to the die nosepiece, which is a broad, hollow, and tapered metal piece containing several hundred holes or orifices spread across its width. The orifices or holes in the die nosepiece release the polymer melt, which then solidifies into thin strands. These strands are then drawn out and stretched into fine fibers (attenuation) by high-velocity hot air (typically at 230 ℃ to 360 ℃ and 1/2 to 4/5 the speed of sound) [111]. A spin head enables the extrusion of low-viscosity molten polymer through a single row of fine holes that are closely spaced, typically ranging from 1000 to 4000 holes/m. To solidify and draw the extruded fibers, high-velocity hot air is used and then cooled by entrained air (winding process). The collected fibers are subsequently formed into a fiber mat.

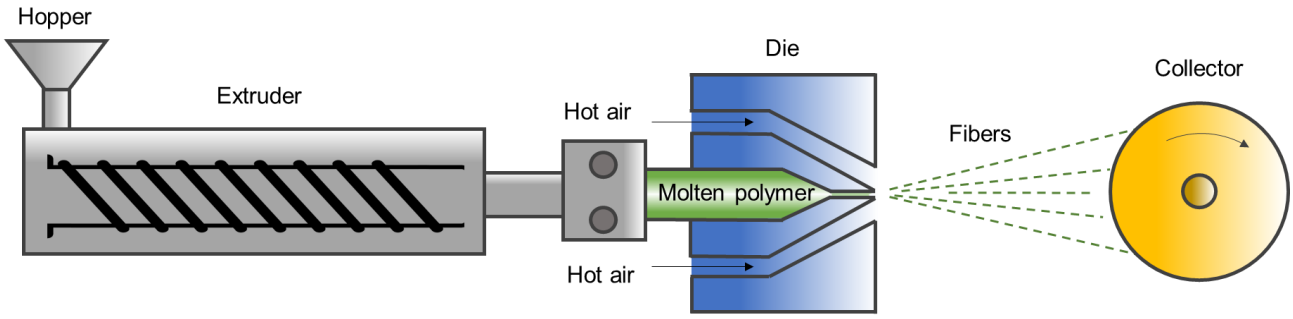

Fig. 2.9. Melt-blowing process from the extruder.

2.2.4. Melt-blowing dynamics

A considerable amount of theoretical and experimental research has been conducted on the mechanisms of fiber dynamics during Melt-blowing [112,113]. Understanding fiber dynamics is critical in controlling the properties of melt-blown nonwoven fibers.

2.2.4.1. Fiber motion

Whipping is a phenomenon that occurs in the melt-blowing process when the polymer fibers undergo lateral oscillations due to aerodynamic forces [112]. The theory of aerodynamically driven jet bending was developed by Entov and Yarin [113], who stated that if the velocity of the flow exceeds a certain critical value, any small disturbance in the flow will grow and result in instability. According to the online measurement conducted by Xie and Zeng [114], the area between 0 to 5 cm at the centerline experienced high air velocities and significant turbulent fluctuations when the polymer melt was discharged from the die. The measurement of turbulence quantities is crucial in the melt-blowing process to understand fiber motion and formation. Also, it can prevent operational problems caused by strong velocity fluctuations, such as fibers sticking to the die face or becoming entangled with themselves or adjacent fibers. Xie and Zheng's observation of fiber whipping amplitude and frequency showed that whipping occurs more intensely with an increase in distance from the die, while the frequency of the whipping action decreased as the distance from the die increased.

One of the factors that influences fiber motion is the airflow field created near the melt-blowing die. The airflow field can be modified by using different die designs, such as slot die and annular die (or swirl die). A slot die is a type of melt-blowing die that has a rectangular opening for airflow. The airflow field near the slot die is important for fiber formation and quality because it determines

the degree of fiber attenuation, whipping motion, entanglement, and cooling. Xie et al. [115] discussed the measurement and analysis of the three-dimensional jet flow field under a common slot-die using a hot wire anemometer, three-dimensional traverse equipment, and a stepper motor. Their results showed that the velocity of airflow is significantly reduced near the slot end face, which affects the distribution of the flow field. The characteristics of the flow field led to inconsistencies in fiber diameter and strength. In the center area and its vicinity, air velocities are high with little difference between them, while distant areas have lower velocities and no drafting effect on the fiber. The velocity on the spinning line decreased sharply as the distance to the die increased, and the instantaneous speed fluctuated rapidly, which can cause fiber whipping and hinder smooth drafting.

On the other hand, a swirl-die (annular-die) can produce a swirling diffused airflow that can induce helical fiber motion and result in fibers with specific patterns. Moore et al. [116] reported that the inner annular wall of the die creates significant variations in turbulence behavior, including the formation of a recirculation region due to the center wall effects. In addition, the annular orifice generates a substantial amount of turbulence in its immediate vicinity, which is much greater than that generated by a circular orifice. The flow properties of a swirl die are significantly different from those of a more extensively studied slot die. Zhu et al. [117] studied the relationship between the lateral swirling diffusion of airflow and fiber distribution in the unique swirl-die melt-blowing process. The three-dimensional resultant velocity of air (v) in the swirl-die melt blowing was three-dimensionally decomposed into its lateral velocities (v_r and v_s) and the downward velocity (v_z), which is directed toward a fiber collector. The fiber path in the swirl-die melt blowing was captured

using high-speed photography. It was found that the critical boundary of the air lateral diffusion velocity (v_r) played a significant role in controlling the lateral fiber distribution during melt-blowing. However, most of the twisting velocity (v_s) was located outside the conical fiber envelope and had little contribution to the continuing helical motion of the fiber below 6 mm from the die.

2.2.4.2. Fiber diameter

Numerical simulation has been used in several studies to predict the diameter of melt-blown fibers during the melt-blowing process. The first model, developed by Uyttendaele and Shambaugh [118], was based on equations used in the melt-spinning process and simulated fiber dynamics in one dimension. Shambaugh and his team later improved the model by expanding it to two-dimensional and three-dimensional models [119,120], allowing the fibers to experience lateral velocity perturbations and simulate the whipping phenomena observed during melt-blowing.

The distance between the die and collector (DCD) affects the diameter of melt-blown fibers, as it impacts the fiber attenuation rate due to aerodynamic drag and fiber entanglement [121]. The effect of DCD on melt-blown fiber properties depends on intrinsic material properties, such as crystallization kinetics, viscosity, and relaxation time [100]. Fibers produced at larger DCDs tend to have smaller diameters due to greater deformation from high-speed hot air drag. DCD also influences the mat thickness and pore size of melt-blown fibers. Fiber speed is generally independent of diameter, except near the die where entanglement is low [122]. It is therefore anticipated that during melt-blowing, fine fibers will have a lower temperature compared to coarse fibers due to their faster cooling rate and similar exposure time to cool air.

Air temperature and air pressure are critical parameters in melt-blowing that can influence fiber diameter. Studies have shown that as the air temperature increases, the average fiber diameter tends to decrease [123,124]. This is because higher temperatures soften and melt the polymer resin to the required viscosity for efficient extrusion in melt-blowing [125]. Also, air temperature affects the processability of the material and the physical properties of the polymer melt. Lower polymer flow rate and higher initial temperature have been shown to decrease the fiber diameter [124]. An increase in air pressure can also lead to a decrease in fiber diameter. The shape of fibers produced in melt-blowing is affected by both air pressure and air velocity, which are linked to the rate of airflow. When air velocity is increased during the process, it leads to greater attenuation and results in a smaller fiber diameter [100]. However, generating excessive air pressures during the process can result in fiber breakage and the production of loose fibers. In order to minimize the significant energy cost associated with the use of pressurized hot air in melt-blowing, it is important to develop a technique to produce melt-blown fibers with low air velocity [121].

Tan et al. [126] examined how the linear viscoelasticity of polymer melt impacts the diameter and diameter distribution of melt-blown fibers. Polystyrene of varying molecular weights was added to control the viscosity and elasticity of the testing samples. The average diameter and fiber diameter distribution, or the coefficient of variation were used and calculated with the following equations (Equations (2.4) and (2.5)).

$$f(d) = \frac{1}{(d \cdot \sigma\sqrt{2\pi})} \, exp\left[-\frac{1}{2\sigma^2}\left\{ln\left(\frac{d}{d_{av}}\right)\right\}^2\right] \tag{2.4}$$

Where the $f(d)$ is lognormal distribution, d is the fiber diameter, d_{av} is the average diameter, and σ is standard deviation.

$$CV = \sqrt{exp(\sigma^2) - 1} \times 100\ \% \tag{2.5}$$

Where CV is the coefficient of variation.

The study found that increasing viscosity resulted in an increase in average fiber diameter, with minimal effect on CV. Conversely, increasing elasticity above a certain threshold value decreased CV while increasing average diameter, as illustrated in **Fig. 2.10** The figures show the average diameter (d_{av}) and coefficient of variation (CV) of melt-blown polystyrene samples (of almost constant viscosities) as a function of the longest melt relaxation time (λ_1), which associated with elasticity. A notable increase in average diameter was observed at the highest elasticity (highest λ_1) and a decline in CV beyond a specific threshold value (1 ms $\leq \lambda_1 \leq$ 10 ms) was observed along the increase of elasticity.

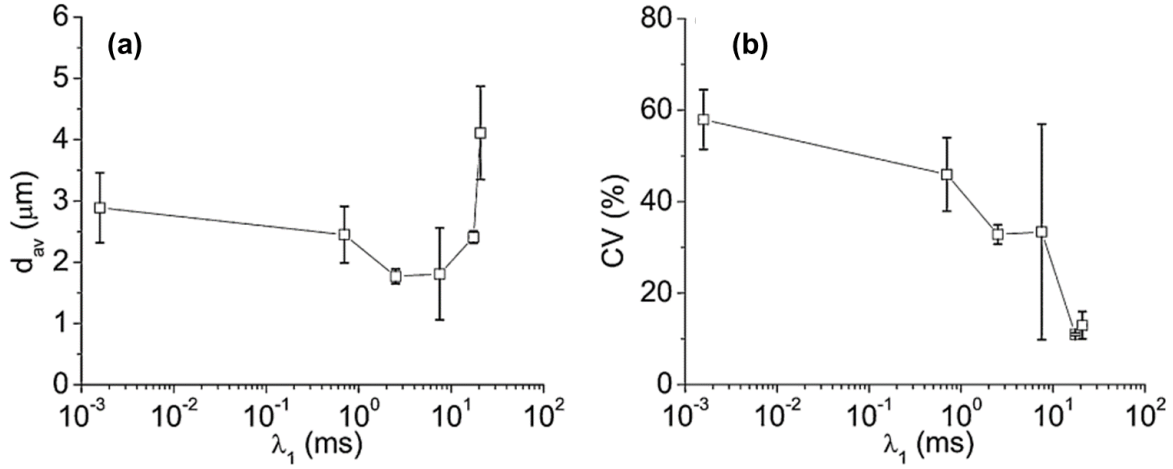

Fig. 2.10. (a) Average diameter (d_{av}) and (b) coefficient of variation (CV) of melt-blown

polystyrene fibers at approximately constant viscosities. (Reproduced with permission from [126]. Copyright 2010 Elsevier Inc.)

2.2.4.3. Crystallization

Crystallinity is also an important physical property to understand melt-blown fibers. Uyttendaele and Shambaugh [118] analyzed the crystallinity of melt-blown PP using a differential scanning calorimeter (DSC) with a 20 ℃/min scan rate of 5-6 mg sample. A single peak was found at 159 ℃ which was caused by the monoclinic crystal structure due to the high spinning speed and the tested polymer's relatively low melt flow index (35 g/10min). Bresee and his team observed fiber crystallization behavior through successive investigations of melt-blown fibers. They reported that fiber attenuation mostly occurred close to the die area before the fibers had solidified while most of the molecular orientation and crystallization occurred further from the die after the fibers had solidified [127]. The fiber array structure was found to be less complex near the die but exhibited greater complexity further away from the die. In their later work, wide-angle x-ray diffraction (WAXD) and small-angle x-ray scattering (SAXS), and optical microscope measurements were taken at various locations between the die and collector, as well as from a web retrieved from the collector by Yin et al. [122] to investigate the crystallization of PP during melt-blowing. The WAXD measurements revealed that fibers between the die and collector were mostly smectic mesophase, while the web from the collector exhibited a well-defined monoclinic crystalline structure. This suggested that the majority of fibers did not crystallize until they reached the collector. The SAXS measurements further supported this observation, indicating that fibers 25 cm from the die showed little lamellar stacking, while fibers retrieved from the collector contained

well-stacked lamellae. Moreover, optical microscope images showed that no spherulites were present in fibers retrieved at any location between the die and collector, whereas coarse fibers retrieved from the collector contained large spherulites.

The effects of various melt-blowing parameters on the structure of PP fibers were studied by Kara and Molnár [121]. It was observed that lower air velocity, pressure, and temperature led to slower cooling rates and higher fiber crystallinity. The tensile behavior of the fibers changed from malleable to brittle as the air temperature and pressure increased, due to increased fiber entanglements and a crystalline structure change. The structure of melt-blown fibers was analyzed using WAXD, which showed the formation of crystalline, amorphous, and mesomorphic phases. The content of these phases varied depending on the processing conditions and the temperature gradient between DCD. They found that it was essential to minimize the temperature difference between the fiber and its surroundings to generate high-strength melt-blown fibers with a perfect crystalline structure and high air stretching was also required to reduce crystallite size and improve molecular orientation.

2.2.4.4. Porosity and pore size

The functionality and filtration performance of melt-blown fibers is greatly affected by their pore size. Fabrics produced by melt blowing have a range of porosity from 70 to 99%, fiber diameters from 500 nm to hundreds of microns, and exhibit alignment and anisotropy [128]. The pore size can be controlled by adjusting the production parameters such as fiber diameter, air pressure, temperature, and polymer melt viscosity [121,129,130]. High-speed air jets also lead to the formation of finer fibers and smaller porosities, which in turn reduces the size of pores of the fiber

web [131]. The thickness of the fiber web is affected by the speed at which the collector moves, with a slower speed causing an increase in thickness and a further reduction in pore size [132]. Kara and Molnár [121] conducted a study in which they investigated the impact of various parameters on the pore size and porosity of melt-blown PP fibers (**Fig. 2.11**). The research discovered that the porosity and the pore size of melt-blown fibers are influenced by DCD, air temperature, and air pressure. When DCD increased, pore size first decreased until 150 mm but then increased with higher DCD. Increased air turbulence at extended DCD led fibers to spread out over a larger area, reducing fiber packing density, and creating a softer texture. As the air temperature increased, the fiber diameter shrank and resulted in fluctuating porosity and overall reduced pore sizes, and at 125 ℃ (the lowest tested temperature) the fibers exhibited the highest porosity with large pore size. Elevated air pressure constricted fiber flow, leading to increased mat thickness and fiber packing density, which subsequently caused smaller pores and a thicker mat.

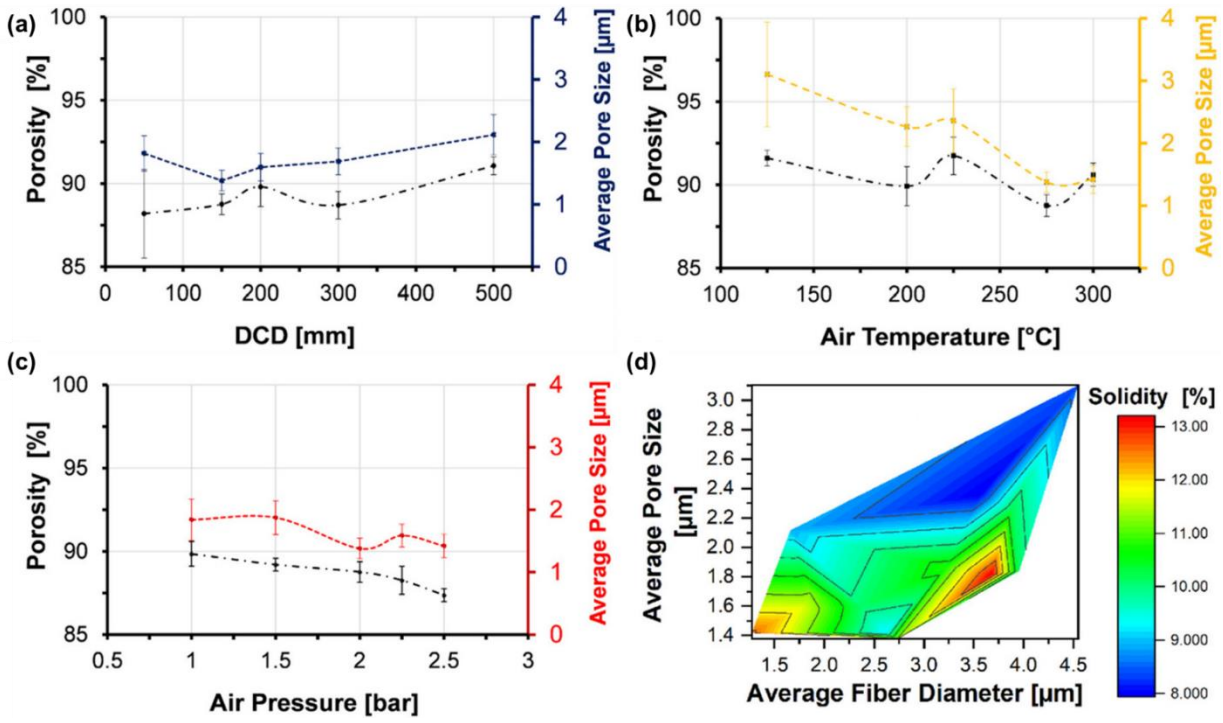

Fig. 2.11. Porosity and pore size of PP melt-blown fibers as a function of (a) die-to-collector distance, (b) air temperature, (c) air pressure; (d) 2D contour plot of fiber solidity and pore size as a function of fiber diameter. (Reproduced with permission from [121]. Copyright 2021 John Wiley & Sons, Inc.)

The pore size of melt-blown fibers ($\overline{D}$) can be represented by employing Equations (2.6) and (2.7) [133].

$$\overline{D} = d_f \sqrt{\frac{32}{(1-c)^2 f(c)}} \tag{2.6}$$

$$f(c) = \frac{5.6c}{-lnc + 2c - 0.5c^2 - 1.5} \quad (2.7)$$

Where d_f is average fiber diameter, c is fiber packing density, $(1 - c)$ is porosity, and $f(c)$ is the function of fiber packing density given by Langmuir [134].

2.2.5. Melt-blown fibers for oil sorption

Nonwoven sheets of micro- and nanofibers produced from the melt-blowing process are highly effective as oil sorbents. The fibrous structure created by this melt-blowing allows for a highly porous surface area and is especially suitable for applications such as oil/water separation and oil sorption [135]. Especially, utilizing polypropylene (PP) in the fabrication of melt-blown fibers allows for enhanced oil adsorption performance, as PP inherently repels water and adsorbs oil [136]. Employing melt-blowing technology, ultrafine PP fibers are formed to create a specific structure characterized by microscale roughness and exceptional wetting properties. The PP melt-blown fibers exhibit high breakthrough pressure and exceptional separation efficiency with stability and reusability in a range of demanding environments [137].

Zhang et al. [137] fabricated a PP membrane through a facile melt-blowing process. The PP membrane showed exceptional oil-water separation capabilities, high flux, and improved intrusion pressure. The membrane's hydrophobic nature, along with the coarse and porous structure created by the interlacing of low-surface-energy fibers of different sizes contributed to its ability to selectively permeate oil over water. These membranes excelled at separating oils like pump and crude oil from various aqueous solutions, achieving over 99% separation efficiency. They

remained functional in harsh environments and are reusable for at least 20 cycles while preserving their effectiveness.

Meng et al. [138] examined the impact of varying melt flow indexes (MFIs) on the oil absorption capacity and diameters of PP melt-blown fibers. Four types of PP with different MFIs (800 g/10min, 1100 g/10min, 1300 g/10min, and 1800 g/10min) were prepared. PP resins are divided into two groups: 1) unblended PP resins with 4 different MFIs and 2) blended PP resins, in which each resin consists of two different PP types with distinct MFIs, combined in a 50:50 ratio. Both groups of PP resins were melt-blown into fibers using a swirl die melt-blowing apparatus. A blended PP fiber web consisting of 50% PP with an MFI of 1800 g/10min and 50% PP with an MFI of 800 g/10min demonstrated the highest oil adsorption capacity at 94.05 g/g. In contrast, unblended PP webs with MFIs of 800 g/10min and 1800 g/10min exhibited oil adsorption capacities of approximately 50 g/g and 70 g/g, respectively. This can be attributed to the variations in porosity and fiber diameter. Unblended PP fiber web with low MFI (800 g/10min) created a large average fiber diameter (5.68 μm), while that of a high MFI (1800 g/10min) created a small average fiber diameter (1.97 μm). The high porosity and large disparities in fiber diameter for a blended PP fiber web ensured a rapid oil sorption rate and large storage space for the adsorbed oil. Moreover, this blended PP fiber displayed good reusability, maintaining a sorption capacity of 18.36 g/g after five cycles. It was found that blended PP fiber combined with different MFIs presented a promising option for oil spill remediation.

Sun et al. [139] blended PP and titanium dioxide (TiO_2) through an extruder and then created PP/TiO_2 fibers through melt-blowing designed for oil/water separation and photocatalysis.

Differential scanning calorimetry (DSC) and thermogravimetric analysis (TGA) results revealed that the presence of TiO_2 increased crystallinity and raises the thermal decomposition temperature. Scanning electron microscopy (SEM) images demonstrated a uniform dispersion of TiO_2 within the PP matrices, leading to a larger fiber diameter and rougher surface. The study overall showed crystallization, thermal stability, and photocatalytic performance due to an increase in TiO_2 content. The addition of TiO_2 increased oil/water separation efficiency, and oil flux (about 15,000 L/m^2h), and the fibers remained stable after 6 hours of ultraviolet exposure.

Chapter 3: Fabrication of Triblock Elastomer Foams for Oil Absorption Applications: Effects of Crosslinking, Composition, and Rheology Factors

3.1. Introduction

Marine oil spills caused by catastrophic equipment failure in oil transportation or oily wastewater release from industrial operations can lead to economic loss and severe environmental damage to marine life. The necessity of polluted water remediation has urged scientists and technocrats to develop oil spills cleanup methods, such as an in-situ burning method, bioremediation, gravity-based separation, and the use of chemical dispersants [140–142]. Among the various methods, employing oil absorbents is considered one of the most efficient ways because they cause minimal harm to the marine environment and remove pollutants swiftly with high oil uptake efficiency [143]. Until recently, microcellular polymeric foams such as polyurethane-, polyethylene-, polypropylene-, and polystyrene-based foams have gained greater attention in being utilized as high-performance oil-absorbent materials [144–150]. The hydrophobicity and interconnected porous structure allow these polymeric foams to have a large surface area, low density, deformability, elasticity, excellent oil/water selectivity, and enhanced oil uptake ability.

Moreover, polymeric foams can be readily manufactured by employing either physical or chemical foaming methods. In the physical foaming method, the foaming agents such as CO_2 and N_2 are treated under high pressure and temperature to reach the supercritical state and impregnate into a softened polymer. Upon depressurization, the lowered pressure allows the compressed gas in the polymer matrix to expand and create pores [34]. On the other hand, in the chemical foaming

method, low-molecular-weight and thermally decomposable organic or inorganic foaming agents are utilized. Under a high temperature, the chemical agents decompose to generate gas such as N_2, CO_2, or CO within the blended polymer. The gas bubbles expand when the polymer solidifies at room temperature, creating polymer foams [151].

While physical foaming has the advantages of being cost-efficient and eco-friendly, the limitation of this method is the severe post-foaming shrinkage, especially in elastomeric foams [152,153]. The foaming of elastomers is more complex than thermoplastics due to their elastic nature. Elastomers allow foaming agents (gas) to impregnate their polymer matrix and create gas bubbles during the foaming process; however, they turn rubbery after they are exposed to ambient temperature and pressure. Owing to the low modulus in the rubbery state, elastomers cannot withstand the compressive force from the air, causing gas bubbles within the polymer system to shrink and constrain the foaming expansion [154]. This issue can be resolved by introducing crosslinking (or vulcanization) to give a high modulus to the elastomers [155]. In the physical foaming method, the crosslinking must first be carried out, followed by the foaming process; however, the pre-crosslinked network often hinders cell growth and foam expansion. On the other hand, chemical foaming allows crosslinking and the foaming process to coincide, which minimizes post-shrinkage and improves the elastomers' dimensional stability [34].

Thermoplastic elastomers (TPEs) are melt-processable polymers like thermoplastic and yet possess the properties of elastomers. These elastomers can be easily re-softened, molded, and blended again with other thermoplastics or TPEs, as crosslinking does not occur in the melting process unless external crosslinkers are provided [156]. Styrene-ethylene-butylene-styrene (SEBS)

is a type of TPE obtained by hydrogenating a styrene-butadiene-styrene (SBS) block copolymer, which eliminates carbon-carbon double bonds of butadiene moiety to form ethylene-butylene blocks [157]. This triblock copolymer is composed of rubbery midblock (ethylene-butylene) and glassy end blocks (styrene) [158]. The midblock is soluble in hydrocarbon oil, but the end blocks are not; therefore, the polymer can absorb a large amount of oil while maintaining its elasticity. Compared to other typical triblock copolymers such as SBS and styrene-isoprene-styrene (SIS), SEBS has relatively higher modulus and resistance to moisture, UV light, and heat degradation, and is therefore employed in various applications, such as coatings, automotive, adhesives, insulation, and sealants [159]. Along with its hydrophobicity and oil-absorbing ability, the excellent mechanical properties of SEBS suggest that it has great potential to serve as a high-performance oil-absorbent material.

In this study, porous SEBS elastomer foam was conceived to maximize the properties of SEBS as an oil-absorbent material. In addition, another type of TPE, ethylene propylene diene monomer (EPDM), was selected as a blending partner of SEBS. This is because, EPDM is a widely used and commercially available TPE that exhibits a high resemblance with SEBS in terms of the chemical structure and physical properties, such as hardness and rheology, to generate a compatible blend [160]. Moreover, EPDM has sufficient melt strength and appealing physicochemical properties to generate high-performance elastomer foams with excellent mechanical properties, outstanding resistance to chemicals, heat, and weathering, and ease of processing and creating porous structure [161–164]. Last, adopting EPDM enables crosslinking in the polymer system on account of the unsaturated double bond (from ethylidene-2-norbornene (ENB)) on its structure. The crosslinking

allows finetuning of the melt strength to facilitate foaming expansion and foam stability, as well as to enhance the thermal, mechanical, and rheological properties [155,165].

The novelty of this study is that SEBS has yet to be investigated as a base material to be utilized as an oil-absorbent material. Furthermore, the foaming of triblock elastomers, including SEBS-based foam remains largely unexplored compared to other TPEs, such as EPDM and ethylene vinyl acetate (EVA) foams. Only a limited number of investigations have been reported regarding SEBS foams, such as supercritical carbon dioxide physical foaming of SEBS/PP and SEBS/PS [166–169], or supercritical nitrogen foaming of SEBS [170]. However, the above-mentioned materials exhibited low expansion ratios and rather limited success. Thus, this research aimed to investigate the viability of SEBS as an oil-absorbent material and to understand the crosslinking effect in the foaming of the SEBS/EPDM blend.

3.2. Materials and methods

3.2.1. Materials

Styrene-ethylene-butylene-styrene (SEBS) (KRATON G1652 M, density = 0.91 g/cm^3, solution viscosity = 550 cP (20% in toluene at 25 °C), and styrene content = 30 wt.%) was obtained from Kraton (TX, USA). Ethylene propylene diene monomer rubber (EPDM) (SABIC EPDM 657, density 0.87 g/cm^3, and ethylidene-2-norbornene (ENB) content of 5 wt.%) was sourced from SABIC (Saudi Arabia). Dicumyl peroxide (DCP) was purchased from Sigma-Aldrich (ON, Canada). Azodicarbonamide (ADC) 97%, a chemical foaming agent with a decomposition temperature of 200 °C, was obtained from Sigma-Aldrich (ON, Canada). Hyvolt II transformer oil

and FR3 oil (vegetable oil) were purchased from Fluids, Inc. (MS, USA) and Cargill (MN, USA), respectively.

3.2.2. Processing methods

3.2.2.1. Batch mixing

The SEBS/EPDM foam formulations (**Table 1**) were prepared in a batch mixer (HAKKE Rheomix Lab Mixer, Thermo Fisher Scientific) equipped with Banbury rotors (Rotors R3000, Banbury). SEBS was first softened in the batch mixer, then EPDM was added with the processing temperature and the rotation rate at 170-180 ℃ and 60 rpm. The batch mixer was air-cooled to ~125℃ to add 8 phr of ADC and 0.2 phr of DCP. ADC and DCP content were selected based on preliminary experimentation and optimization. The levels of ADC and DCP varied from 2 to 12 phr and 0.1 to 1 phr, respectively, and the optimal concentrations were 8 phr and 0.2 phr, respectively. The compositions were then allowed to be mixed (60 rpm, 125 ℃). When the rotor torque showed a substantial increase (~50 Nm), the mixing was carried on for 1-2 minutes, maintaining the temperature below 150 ℃ to avoid the decomposition of ADC and a DCP mediated crosslinking.

Table 3.1. The material composition of SEBS/EPDM and SEBS/EPDM/DCP.

	Sample name	SEBS (wt.%)	EPDM (wt.%)
SEBS/EPDM	S100	100	0
	S80E20	80	20
	S60E40	60	40
	S40E60	40	60
SEBS/EPDM/DCP	S100/DCP	100	0
	S80E20/DCP	80	20
	S60E40/DCP	60	40
	S40E60/DCP	40	60

3.2.2.2. Compression molding

The obtained mixture from the batch mixer was cut into small pieces and processed in the compression molding press (Carver 4386 CH laboratory manual heated press, Carver) at a temperature and pressure of 130 ℃ and 5.5 metric tons for 20 min to form 3 mm thick sheets. Each sheet was then exposed to 200 ℃ for 20 minutes in a 3.0 mm mold spacer. In this procedure, the high temperature allowed the chemical foaming agent (ADC) to decompose and generate gas inside the material to create foam. Simultaneously, DCP decomposed into radicals and developed crosslinking nodes between polymer chains. **Schematic 1** describes a schematic illustration of the foaming process and network formation.

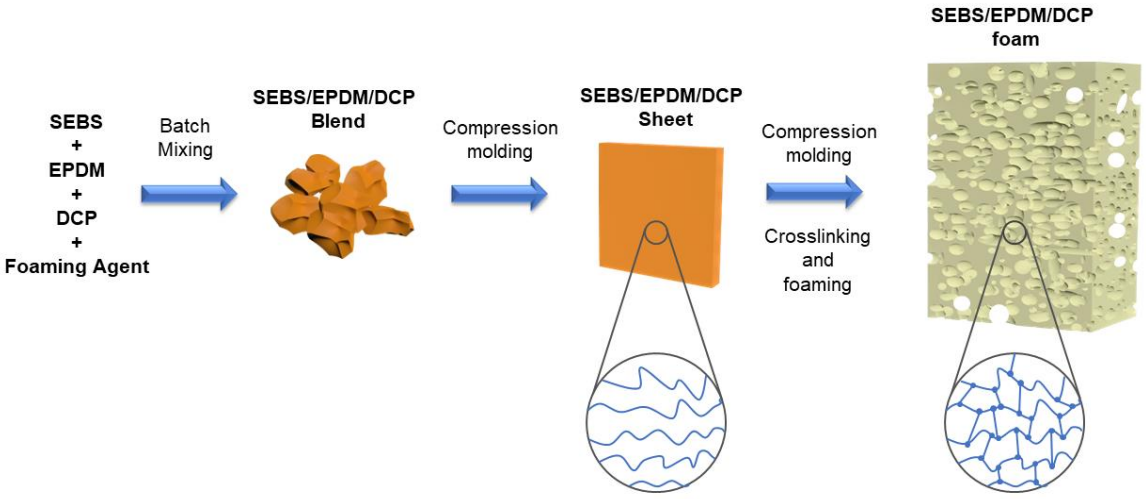

Schematic 1. Schematic procedure of creating SEBS/EPDM/DCP foam.

3.2.3. Characterization

3.2.3.1. Density and volume change

The density (g/mL) of SEBS/EPDM and SEBS/EPDM/DCP before and after foaming was evaluated by the water displacement method using a densimeter (Densimeter MD-300S, Alfa Mirage). The volume change and expansion ratio (ϕ) were calculated as per Equations (3.1) and (3.2).

$$Volume\ change\ (\%) = \frac{V_2 - V_1}{V_1} \times 100 \tag{3.1}$$

$$\phi = \frac{\rho_1}{\rho_2} \tag{3.2}$$

Where V_1 [mL/g] and V_2 [mL/g] are the volumes per weight of each sample before and after foaming, respectively. Similarly, ρ_1 and ρ_2 are calculated to evaluate the density of the samples before and after foaming, respectively.

3.2.3.2. Gel and swelling ratio

The gel content and the swelling ratio were evaluated to confirm the formation of crosslinking nodes and to determine the weight increase from the dried gel to the wet gel due to solvent absorption, respectively. For this, each foam sample was soaked in hot toluene (80 ℃ for 20 h). Then, the swollen gel was removed from the toluene and dried in a convection oven (80 ℃ *for 24 h).* The gel content and the swelling ratio were determined using Equations (3.3) and (3.4).

$$Gel\ content\ (\%) = \frac{W_2}{W_1} \times 100 \tag{3.3}$$

$$Swelling\ Ratio\ (\%) = \frac{W_3 - W_1}{W_1} \times 100 \tag{3.4}$$

Where W_1 is the original weight of the sample, W_2 is the weight of swollen gel after hot toluene soaking, and W_3 is the weight of the dried gel.

3.2.3.3. Thermal properties

A dynamic mechanical analyzer (DMA) (Q800, TA Instruments) was employed to test the viscoelastic behavior of SEBS/EPDM and SEBS/EPDM/DCP foams. The sample specimens (5 mm (W) × 10 mm (L) × 2-5.5 mm (T)) were evaluated from -80 ℃ to 60 ℃ at a ramp rate of 3 ℃ /min. The frequency and strain were kept constant at 1 Hz and 0.2 %, respectively.

A rheometer (HAAKE Mars III, Thermo Scientific) was also employed to analyze the intrinsic viscosity (|η*|), storage modulus (G'), and loss modulus (G'') as a function of frequency. A frequency sweep test was carried out at 220 ℃ for SEBS, S40E60, and S40E60/DCP, and 180 ℃ for EPDM, with a frequency of 1 Hz. P20 CS L geometry was used, and each sample was placed between a hot plate and a heated geometry in a gap of 1 mm.

3.2.3.4. Mechanical properties

Mechanical properties, such as tensile strength, elastic modulus, and elongation at break were evaluated using a universal testing machine (AGS-X series, Shimadzu) equipped with a 500 N load cell. For this, the foams were cut into rectangular strips (5 mm (W) × 70 mm (L) × 2-5 mm (T)) and were tested with a strain rate of 500 mm/min. Samples with sizes of 10 mm (W) × 10 mm (L) × 7-9 mm (T) were prepared to evaluate their compressive strength using the same universal testing machine. The maximum compressive stress was determined at a compression of 65 %. The employed test speed was 1 mm/min with a 500 N load cell.

3.2.3.5. Morphology

Field emission scanning electron microscopy (FESEM) (FEI Quanta Feg 250, Oxford Instrument) was employed at a voltage of 20 kV to observe the cell morphology of the foams. The scanning was carried out on the cross-sectional surface of each foam cut via a cryomicrotome. The cell diameter was measured from the average of the major and minor axes of each cell. The cell density (N) was then calculated using Equation (3.5).

$$N_0 = \left[\frac{nM^2}{A}\right]^{\frac{3}{2}} \phi \tag{3.5}$$

Where n is the number of cells in the SEM image, M is the magnification of the image, A is the area of the cell, and ϕ indicates the expansion ratio.

3.2.3.6. Chemical structure analysis

An FTIR spectrometer (Nicolet 670 NEXUS FTIR, Thermo Fisher Scientific) equipped with an Attenuated total reflection (ATR) technique was employed to analyze the chemical functional groups. The FTIR was set in transmittance mode and recorded the spectra 500 to 4000 cm^{-1} at 4 cm^{-1} resolution for 32 scans. The results are presented in **Appendix A** (**Fig. A1**).

3.2.3.7. Oil absorption test

Three SEBS/EPDM and SEBS/EPDM/DCP foam specimens of similar thickness (~ 6mm) were cut into a square shape (20 mm × 20 mm) and accurately weighed to test their oil absorption capacity. They were then immersed in oil (Hyvolt II) for 15 minutes. The foams were then taken out, and the surface was gently blotted with a paper towel to remove excess oil. To evaluate the oil absorption of the foams as a function of time, they were weighed and then submerged again in the oil for the next designated times. The same procedure was repeated, and the time intervals of the specimens submerged in the oil were 15 min, 30 min, 60 min, 2 h, 4 h, 6 h, 8 h, 1 day, 2 days, 3 days, and 5 days. The oil absorption was calculated by weight difference as shown in Equation (3.6).

$$Oil\ sorption\ (\%) = \frac{W_n - W_0}{W_0} \times 100 \quad (3.6)$$

Where W_0 is the original weight of each foam sample and W_n is the weight of the sample after oil absorption for the predetermined time.

3.2.3.8. Wettability test

The water contact angle of SEBS/EPDM/DCP foams was measured using a sessile drop method. 4μL of deionized water was dispensed onto the cross-sectional surface of the foams. The droplet images were captured after 3 seconds of the water drop. The ImageJ contact angle plugin was used to measure the contact angle of each droplet.

3.3. Results and discussion

3.3.1. Foaming expansion

The foaming agent used in this experiment is azodicarbonamide (ADC), a powdered substance mainly used for rubber and thermoplastic foaming. During the heat processing at 200 ℃ in the compression mold, the foaming agent decomposed [171], releasing a relatively large volume of gas, and was entrapped in the softened SEBS/EPDM and SEBS/EPDM/DCP blended sheets. After removing the molding plates, the sheets further expanded to generate highly porous microcellular rubber foams.

Fig. 3.1 (a) presents the volume change and expansion ratio of SEBS/EPDM and SEBS/EPDM/DCP foams before and after foaming. The expansion ratio is an important indicator of the degree of foaming. The densities of all the materials before foaming were between 0.92 and

0.94 g/cm^3. After foaming, the density of SEBS/EPDM foams without DCP decreased to 0.42-0.46 g/cm^3, with an expansion ratio of 2.0 - 2.1. In the case of the foams containing DCP, the same expansion ratio (2.0) was noted for S100/DCP foam; however, sponge-like foams with extensive expansions were fabricated for the compositions containing EPDM of 20 wt.% and above. For S80E20/DCP, its average density changed from 0.93 g/cm^3 to 0.15 g/cm^3, with an expansion ratio of 6.1. Furthermore, S60E40/DCP and S40E60/DCP both showed significant changes in density from 0.92-0.93 g/cm^3 to 0.07 g/cm^3, with an expansion ratio of 12.8 - 13.1 and a volume change of 1200 %, indicating that these are the optimal material compositions for the best foamability. Notably, the densities and the expansion ratios of S60E40/DCP and S40E60/DCP foams were almost identical. Also, the visual appearances of the two foams were similar: fluffy and elastic foams with evenly distributed large pores (**Fig. 3.1 (b)**). As a result, when the proportion of EPDM reached 40 wt.% or more, the foams exhibited a considerable rise in the expansion ratio, and the two foams, S60E40/DCP and S40E60/DCP, both showed comparable foaming characteristics. The enhanced expansion ratio of these samples is related to their melt strength and the DCP-mediated crosslinking, as discussed in the subsequent sections. Representative images of the various composition foams with and without DCP additives are in **Fig. 3.1 (b)**. The changes in the foaming expansions as a result of the foaming formulation variations and the presence of DCP was noticeable in these images.

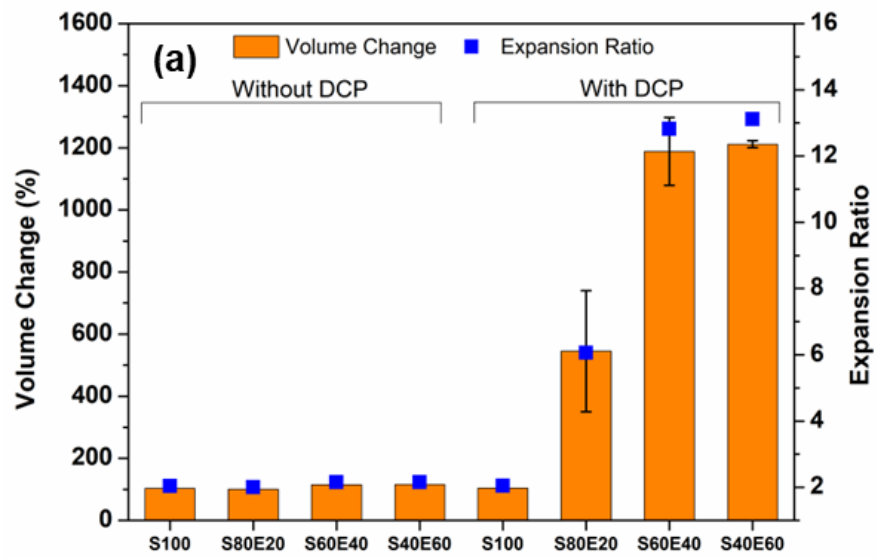

Fig. 3.1. (a) Volume changes due to foaming and expansion ratio of SEBS/EPDM and SEBS/EPDM/DCP foams; (b) Size image of a sheet before foaming and the images of

SEBS/EPDM and SEBS/EPDM/DCP after foaming (size adjusted to the actual ratio of each material).

3.3.2. Characterization of crosslinked foams

To create a high-quality foam, it is essential for the polymer material to have sufficiently high melt strength. As for SEBS/EPDM foams without DCP, the foaming expansion was fairly low (**Fig. 3.1 (a)**) due to a relatively low melt strength, which created weak cell walls that ruptured easily for not bearing the expansion force developed by the generated gases. In order to enhance the melt strength of SEBS/EPDM foams, the peroxide crosslinking method was introduced. The DCP employed in this study can generate free radicals to link polymeric chains in an elevated temperature condition and create a strong carbon-carbon crosslinking bond or chemical bridge between polymers in a three-dimensional structure. Compared to sulfur vulcanization which creates carbon-sulfur and sulfur-sulfur bonds, the carbon-carbon bond generated by peroxides gives better resistance to thermal degradation [172]. As for polyolefins, dicumyl peroxide (DCP) is one of the most widely used crosslinkers due to its easy accessibility and high crosslinking efficiency compared to all the other peroxides [173]. The peroxide-mediated crosslinking mechanism of EPDM is described in **Fig. 3.2 (a)**.

In order to understand the crosslinking effect of DCP in the blend formulations, the gel formation of SEBS/EPDM and SEBS/EPDM/DCP foams was tested [174,175]. **Fig. 3.2 (b)** shows the gel formation experiment using hot toluene as the organic solvent. All the SEBS/EPDM foams without DCP were completely dissolved in toluene, which means that a 3D network gel was not generated without DCP. As for S100/DCP, although a minimal amount of gel was attached to the wall, the

majority of the polymer body was dissolved in toluene. This shows that DCP created slightly crosslinked chains in pure SEBS; however, the crosslinking degree was insufficient to form a stable gel. This is because the styrene end blocks in SEBS lower the crosslinking efficiency as it is difficult for the peroxide to penetrate the styrene segment to form a radical thus most crosslinking happens in the remaining ethylene-butylene midblock, which comprises 70 % of SEBS [176,177]. Moreover, the SEBS employed in this study have relatively low molecular weight (with low solution viscosity (550 cP)), and as a result the short ethylene-butylene midblock had only a small portion to be crosslinked [178]. On the other hand, when DCP was incorporated into the foams containing EPDM, the crosslinking was evident, as the gel formation was noticeable for the S80E20/DCP, S60E40/DCP, and S40E60/DCP. The gel content was the highest for S40E60/DCP (68 %), as shown in **Fig. 3.2 (c)** indicating that the gel content increased with the rise in the EPDM content. As the majority of the crosslinking took place in the EPDM structure rather than in SEBS, a higher amount of EPDM gave more crosslinked polymer chains and therefore improved the quantity of the crosslinked gel network.

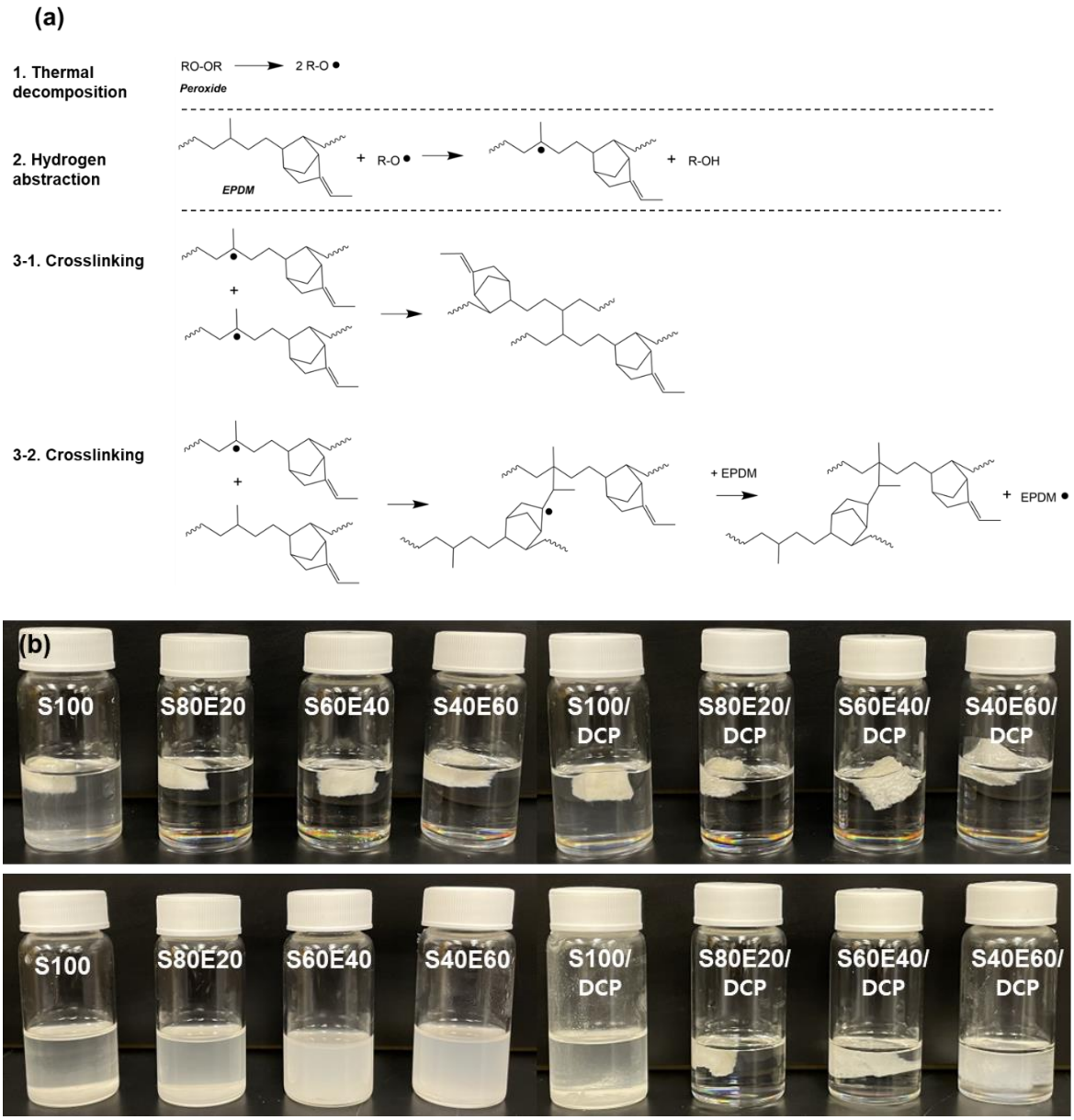
(a)
1. Thermal decomposition
RO-OR
2 R-O •
Peroxide
2. Hydrogen abstraction
EPDM
+ R-O •
+ R-OH
3-1. Crosslinking
3-2. Crosslinking
+ EPDM
+ EPDM •
(b)
S100
S80E20
S60E40
S40E60
S100/ DCP
S80E20/ DCP
S60E40/ DCP
S40E60/ DCP
S100
S80E20
S60E40
S40E60
S100/ DCP
S80E20/ DCP
S60E40/ DCP
S40E60/ DCP

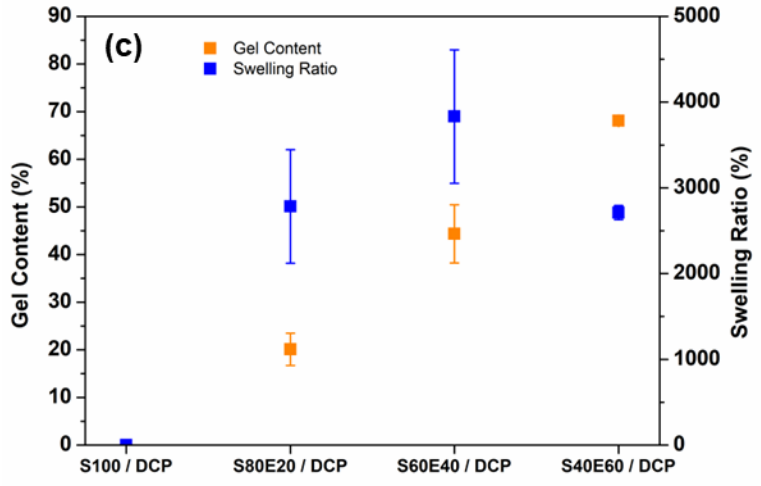

Fig. 3.2. (a) Peroxide crosslinking mechanism of EPDM; (b) Foam specimens immersed in toluene for the gel formation experiment. (Top: right after immersion; Bottom: after immersion at 80 ℃ for 20 h); (c) gel content and swelling ratios of DCP crosslinked foam samples.

3.3.3. Rheology

Interfacial adhesion is generated when two different materials are blended, and it determines how well one material disperses into the other material's polymer matrix. For high interfacial adhesion, the compatibility of the two materials' physical and chemical properties is essential [179,180]. Thus, EPDM was selected as a blending partner of SEBS as it possesses a similar chemical structure (**Fig. A1** in **Appendix A**) and physical properties to SEBS [160]. The essential reason for incorporating EPDM was to enhance the melt strength of the SEBS/EPDM blend via DCP crosslinking. As shown in **Fig. 3.1**, SEBS/EPDM blend with DCP displayed outstanding foam expansion, and peroxide-mediated crosslinking of EPDM is described in **Fig. 3.2 (a)**. To evaluate

the change in the rheology of the baseline and blend samples, the intrinsic viscosity (|η*|), storage modulus (G'), and loss modulus (G") of pure SEBS and EPDM and unfoamed S40E60 and S40E60/DCP were analyzed as a function of frequency and the results are shown in **Fig. 3.3**. The almost identical viscoelastic curves of SEBS and EPDM in **Fig. 3.3 (a-c)** confirmed that the two TPEs have similar rheological properties, which led to their good compatibility. In addition, a significant rise in melt strength was observed for S40E60/DCP compared to S40E60, through the viscosity, storage modulus, and loss modulus results, and it supported the crosslinking effect of

DCP.

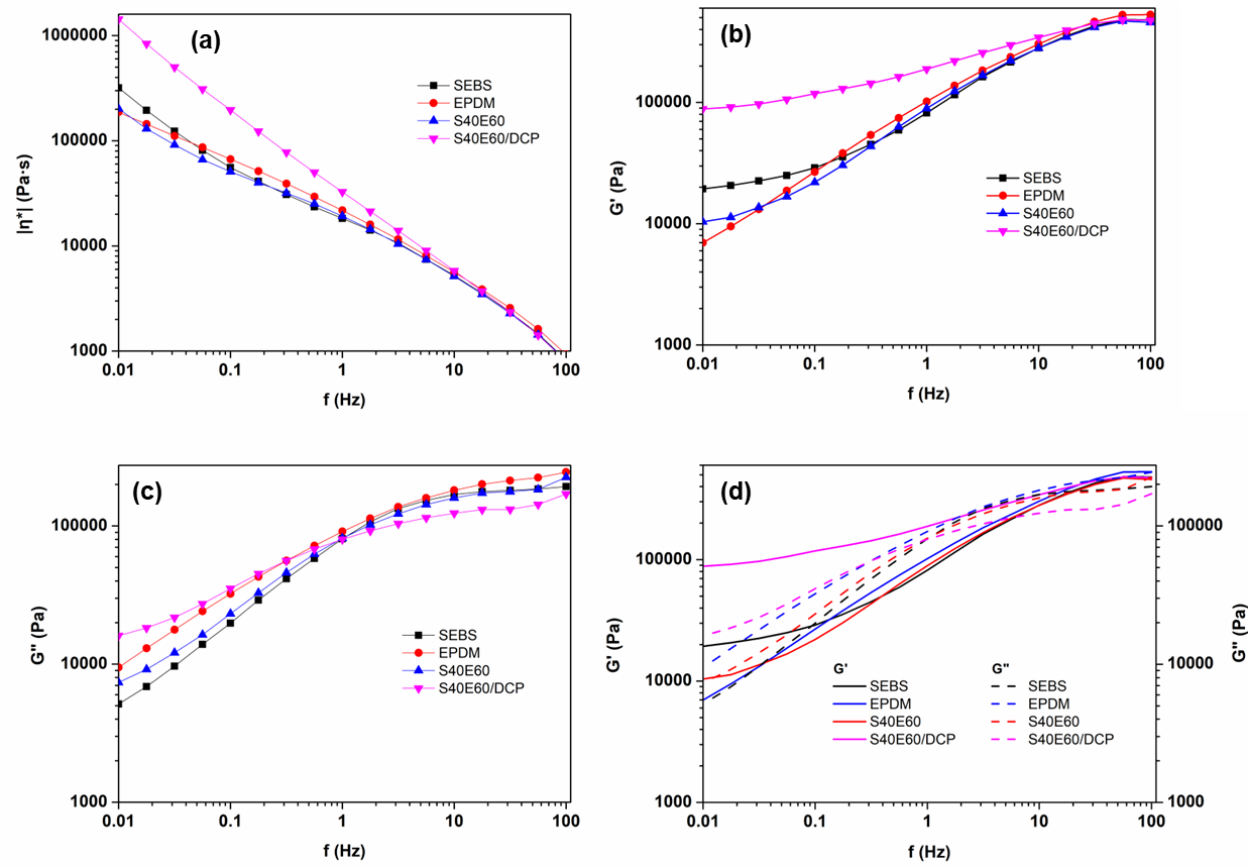

Fig. 3.3. (a) Complex viscosity, (b) Storage modulus, (c) Loss modulus, and (d) Storage and loss modulus of SEBS, EPDM, S40E60, and S40E60/DCP.

Through dynamic mechanical analysis (DMA), the specific storage modulus and tan delta were evaluated as a function of temperature to understand the viscoelastic behavior of SEBS/EPDM and SEBS/EPDM/DCP foams (**Fig. 3.4**). In **Fig. 3.4 (a)**, the storage modulus of S100 foam was found to be 970 MPa/(g/cm^3) at -60 ℃, and it continuously reduced with temperature increase and eventually dropped to 13 MPa/(g/cm^3) at 40 ℃. Each material in the graph showed a steep fall in the midpoint (between -60 ℃ and -40 ℃) because the glass transition temperatures of the materials

were shown within this temperature range. The addition of EPDM has changed macromolecular mobility as the storage modulus gradually decreased from S100 (13 MPa/(g/cm^3) at 40 ℃) to S40E60 (4.5 MPa/(g/cm^3) at 40 ℃). While EPDM gave more flexibility to the materials, DCP added rigidity, as S100/DCP displayed the highest specific storage modulus due to a slight amount of crosslinking brought about by DCP. Although DCP promoted crosslinking in the presence of EPDM, S80E20/DCP displayed a lower storage modulus than S100/DCP because the foam expansion ratio of S80E20/DCP (6.1) is larger than S100/DCP (2.0), which contributed more to elastic energy storage. The foaming expansion added a cushion-like elastic property to the foam. For this reason, S60E40/DCP and S40E60/DCP, the two foams with the highest expansion ratio (12.8 and 13.1, respectively), showed a huge drop in storage modulus. Interestingly, the storage modulus of S40E60/DCP was higher than S60E40/DCP despite the higher EPDM content. This indicated that when the expansion ratios were similar (12.8 and 13.1), the degree of crosslinking contributed more to the storage modulus than EPDM's softening effect. In other words, S40E60/DCP showed increased stiffness than S60E40/DCP, as S40E60/DCP had a larger crosslinked area.

A material's capacity to absorb energy as a function of temperature was expressed as tan delta, the ratio of loss modulus to storage modulus (G"/G') [181]. The temperature at which the maximum peak of the tan delta was shown indicated a glass transition temperature (T_g) (**Fig. 3.4 (b)**). The results in **Fig. 3.4 (b)** demonstrated a single tan delta peak for the SEBS/EPDM blend indicating there was no phase separation and a high likelihood for interfacial adhesion between the SEBS and EPDM phases. Also, the tan delta peaks of SEBS/EPDM foams without DCP showed

a constant rise in T_g from -46 ℃ (S100) to -35 ℃ (S40E60) with an increase in EPDM amount, which demonstrated that EPDM had a higher T_g than SEBS. Likewise, the same tendency was observed in SEBS/EPDM/DCP foams where T_g gradually shifted toward higher temperature from -42 ℃ (S100/DCP) to -38 ℃ (S40E60/DCP).

The magnitude of the tan delta peak expressed the change in the polymer's chain mobility. The peak intensities at T_g were the highest for S100 and S100/DCP. This was because the chain sliding generated from the flexible midblock (ethylene-butylene chains) in SEBS led to an increased loss modulus (G") during the glass transition. The lower peak intensities were observed in formulations with higher EPDM content because the incorporation of EPDM brought about the interfacial adhesion with SEBS, which limited the free volume for molecular movement. As a result, with the increase in EPDM content, the polymer's chain mobility significantly decreased during the glass transition, and the increased elasticity led to higher storage modulus (G') and lower peak intensity. However, a slight increase in peak magnitude was noticed for S40E60 and S40E60/DCP, compared to S60E40 and S60E40/DCP, implying that EPDM's effect in decreasing the peak intensity was limited to a specific concentration.

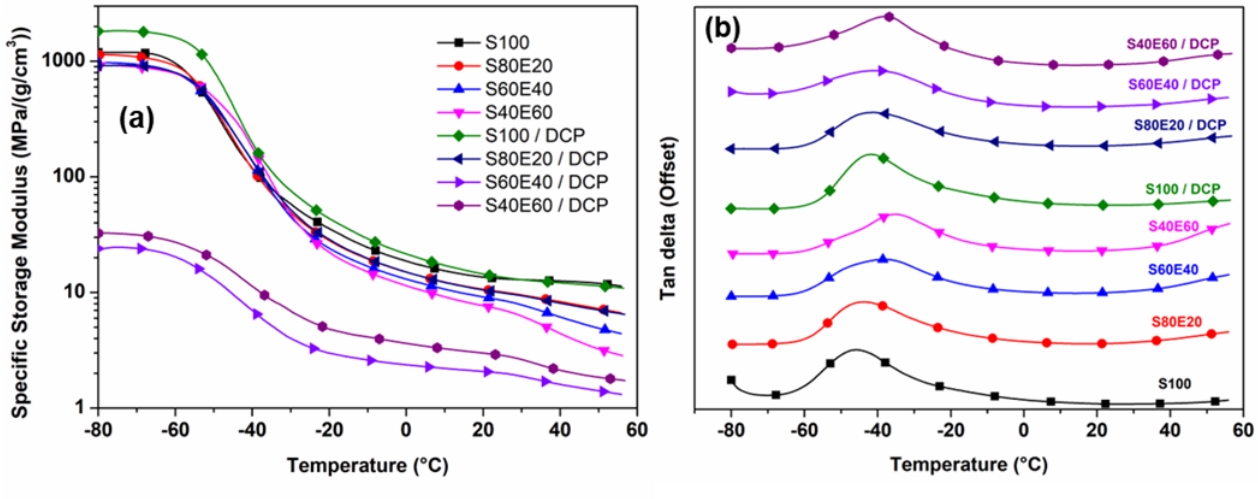

Fig. 3.4. Dynamic mechanical analysis (DMA) (a) Storage modulus and (b) Tan delta as a function of temperature

3.3.4. Mechanical properties

The change in tensile properties as a result of the incorporation of EPDM and the crosslinking effect in the foams was evaluated. The ultimate tensile strength (UTS), modulus (at 0-20 % of strain), and elongation at break were presented in **Fig. 3.5**. Due to the large density difference between SEBS/EPDM and SEBS/EPDM/DCP foams, UTS and elastic modulus (Mpa) were divided by each foam's density (Mpa/(g/cm^3)) for precise comparison. The specific modulus (**Fig. 3.5 (a)**) generally dropped with the increase in the EPDM content. The lowest specific modulus was noted for S60E40/DCP and S40E60/DCP foams (2.1 Mpa/(g/cm^3)), showing that the two highly foamed specimens had low resistance to elastic deformation. The specific UTS results (**Fig. 3.5 (b)**) of 100 wt.% of SEBS content were the highest in both categories of the foams with and without DCP. The graph showed that as for SEBS/EPDM foams without DCP, the increase in

EPDM amount significantly reduced the specific UTS. However, this trend was observed in SEBS/EPDM/DCP foams. For instance, samples with 40 wt.% of EPDM composition showed higher UTS than 20 wt. %. This is likely because the 40 wt.% of EPDM provided higher crosslinking, enhancing the physical stability under tension. The UTS has reduced for S40E60/DCP compared to S60E40/DCP, which can be attributed to the lower tensile strength of EPDM despite the higher crosslinking.

It was seen that adding DCP to pure SEBS foam increased the elongation at break value from 962 to 1112 % (**Fig. 3.5 (c)**), which is contrary to the specific modulus and UTS results (**Fig. 3.5 (a-b)**). Overall, the general tendency shown in **Fig. 3.5 (a-c)** was that the foams containing EPDM had comparatively lower resistance to stretching and displayed lower strain at break.

An apparent change in mechanical property resulting from foaming expansion was observed in the compressive strength. **Fig. 3.5 (d)** exhibited specific compressive strength at 65% strain. High specific compressive strengths from 2.88 to 3.9 MPa/(g/cm^3) were recorded for all the SEBS/EPDM foams and S100/DCP. These formulations had a comparatively low expansion ratio (2.0-2.1). On the other hand, significantly lower specific compressive strengths at 0.26-0.30 MPa/(g/cm^3) were noted for the highly expanded foams (S80E20/DCP, S60E40/DCP, and S40E60/DCP) with expansion ratios of 6.1 to 13.1. Since these foams were largely converted to porous spongey-like morphology, they displayed high shrinkage under compression but also recovered back quickly due to their elasticity.

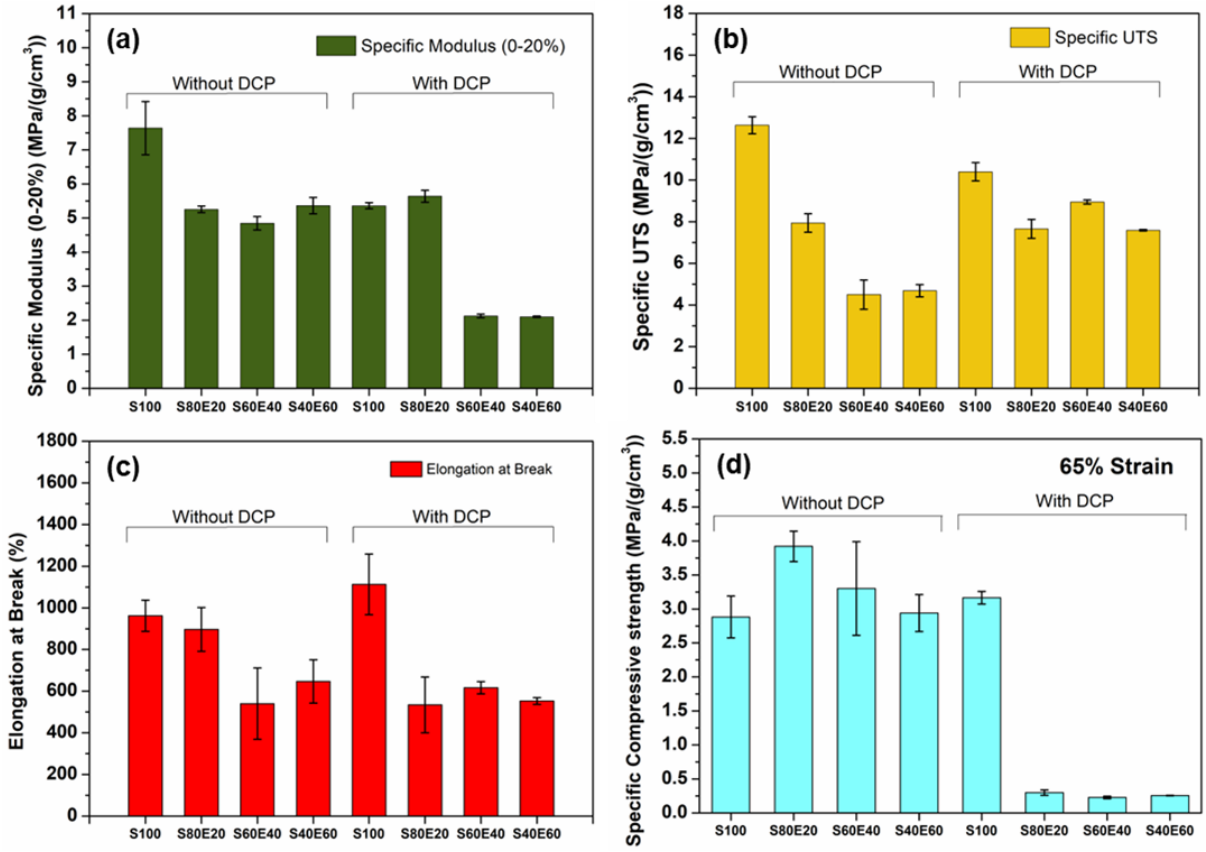

Fig. 3.5. (a) Specific UTS and specific modulus (0–20 % strain), (b) Elongation at break, and (c) Specific compressive strength of SEBS/EPDM and SEBS/EPDM/DCP foams.

3.3.5. Cell structure

The cross-sectional cell morphology of SEBS/EPDM and SEBS/EPDM/DCP foams were investigated, and the results are displayed in **Fig. 3.6 (a)**. The cell morphology of S100 was mostly closed cells; however, a clear trend was seen for SEBS/EPDM foams without DCP, that the foam contained more and more open cells with the increase in EPDM ratio. The addition of DCP in S100 resulted in coalescence, the neighboring cells impinging with one another, and yielded an undefined cell structure with no distinctive cell walls. The microscopic images showed that

SEBS/EPDM/DCP foams with an EPDM content of 20 wt.% or more had a well-defined cell structure. In S80E20/DCP, thick cell walls and polygonal structures were created as a result of impingement. The high elastic modulus of S80E20/DCP, due to its high SEBS content, regulated further cell growth, creating thick cell walls and a vertically flattened shape. Because of increased crosslinked polymer chains in the EPDM matrix, the increase in EPDM amount allowed the foams to have less elastic resistance to cell growth and to possess sufficient durability to retain the enlarged cell structure. Therefore, the large-sized pores in thin cell walls with well-defined cell structures were observed in S60E40/DCP and S40E60/DCP foams.

Cell morphology was further investigated by analyzing cell density and cell diameters (**Fig. 3.6 (b)**). A high cell density of 2.58×10^{14} cells/cm^3 was shown for S100, and small to mid-sized cells with a 147 mm average cell diameter were randomly distributed. In the SEBS/EPDM foams, adding EPDM increased the overall cell sizes, and the cell density decreased accordingly. S80E20 had a slightly lower average cell diameter and a higher cell density than S100, and this was because of the plenty of tiny cells in S80E20.

To compare S100/DCP and S100, similar average cell diameters and cell densities were observed despite the different cell structures. Because of the large foam expansion of S80E20/DCP, the average cell diameter leaped to 744 mm, and the cell density dropped to 2.72×10^{11} cells/cm^3. The cell size further increased for S60E40/DCP and S40E60/DCP foams (cell diameters 1025 and 890 μm, respectively), with cell densities of 1.12×10^{11} and 1.63×10^{11} cells/cm^3. The result illustrated that the enhanced melt strength of S60E40/DCP and S40E60/DCP owing to an enlarged

crosslinking network improved the stability of bubble nucleation, therefore the fully expanded foams led to good distribution of large-sized cells, and the cell density reduced consequently.

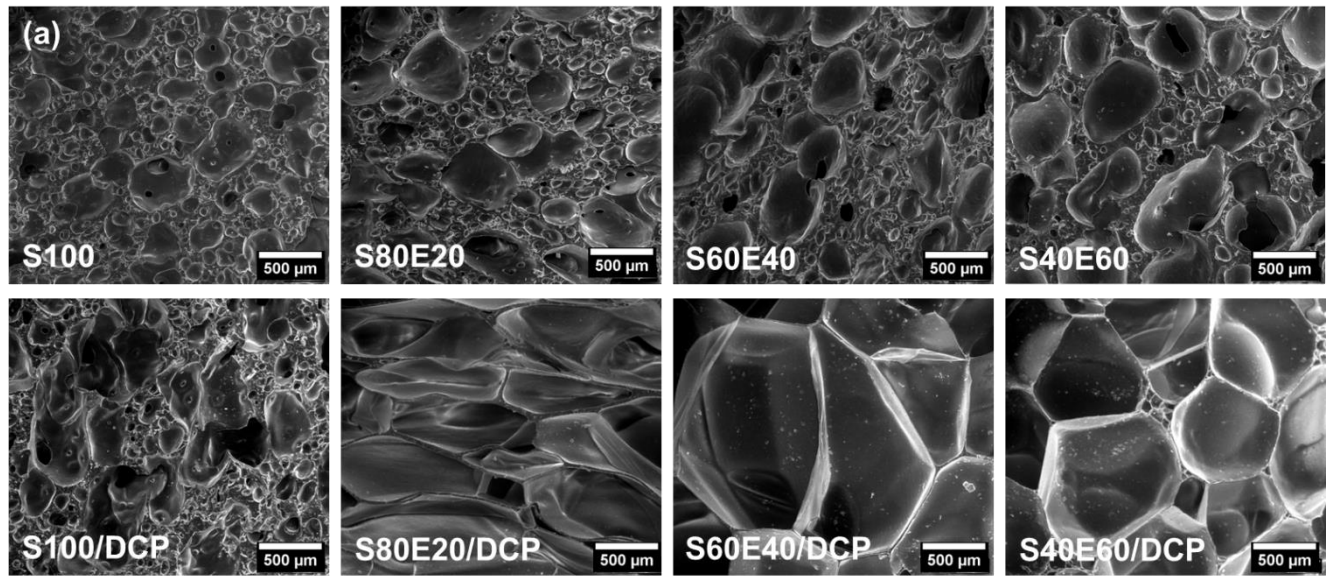

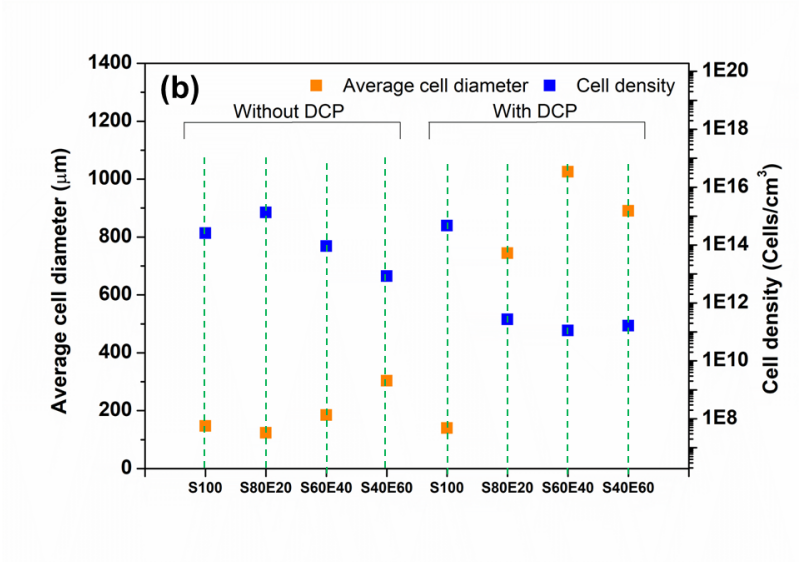

Fig. 3.6. (a) SEM images of SEBS/EPDM and SEBS/EPDM/DCP foams; (b) Average cell diameter and cell density.

3.3.6. Oil absorption performance

Fig. 3.7 shows the oil absorption performance of SEBS/EPDM and SEBS/EPDM/DCP foams for a transformer oil (Hyvolt II) recorded for 5 days. The tested materials in **Fig. 3.7 (a)** are SEBS/EPDM foams without DCP. Although there was no meaningful change in the expansion ratio between the four foams, which was around 2 (**Fig. 3.1**), the observed general trend was that as the EPDM content increased, so did the oil absorption capacity. The oil absorption of the S100 at 1 h, 1 d, and 5 d was 32, 60, and 93 wt.%, and that of S60E40 was 48, 115, and 268 wt.%, respectively. The oil absorption capacity of S40E60 on day 5 was higher than twice the amount of S100. The SEM images of SEBS/EPDM foams (**Fig. 3.6 (a)**) support the reason behind this observation. The dominant cell structure was closed cells for S100; however, as the EPDM content increased from 20 wt.% to 60 wt.%, the SEM images showed increasing cell size and open cell ratio. This cell structure allowed the oil to spread along the interconnected cell walls rapidly; thus, the oil can be efficiently absorbed and contained in the entire polymer system [91]. Also, while there was almost no difference in oil absorption between unfoamed SEBS and S100 foam, an increased oil absorption was seen for S40E60 foam compared to unfoamed S40E60, due to its enlarged surface area.

The oil absorption performance of SEBS/EPDM-based foams containing DCP is presented in **Fig. 3.7 (b)**. Due to the crosslinking effect of DCP in the EPDM matrix, the foams expanded to a great extent and formed a highly porous structure with large pores (average diameter of 7–4 - 1025 mm). The common trend observed in both SEBS/EPDM and SEBS/EPDM/DCP foams (**Fig. 3.7 (a-b)**) was that the higher EPDM content promoted foaming and hence oil absorption. In the case of

SEBS/EPDM/DCP foams, adding DCP in the presence of EPDM boosted the oil absorption capability. The oil absorption of S80E20/DCP at 1h, 1d, and 5 d was 352, 575, and 624 wt.%; for S60E40/DCP, it was 337, 643, and 1019 wt.%; and for S40E60/DCP, it was 314, 648, and 1030 wt.%, respectively. Remarkably, S60E40/DCP and S40E60/DCP obtained oil absorption of over 1000 wt.% on day 5. Moreover, while S80E20/DCP seemed to have reached equilibrium absorption capacity at 624-629 % from day 3, the oil absorption of S60E40/DCP and S40E60/DCP was anticipated to rise further until reaching the equilibrium amount after day 5. Thus, S60E40/DCP and S40E60/DCP presented the maximum absorption performance among all the tested materials. The fact that S60E40/DCP and S40E60/DCP had a high expansion ratio (12.8 and 13.1, respectively) accounted for the oil uptake ability. The larger expansion of the foam led to a larger cell size with thinner cell walls. Thus, capillary action was promoted, and together with solvent-induced swelling, it enabled efficient diffusion of oil within the polymer system [182]. Since SEBS/EPDM foams and S100/DCP presented low expansion (expansion ratio 2.0-2.2), their oil absorptions were recorded to be significantly lower compared to the largely expanded foams such as S80E20/DCP, S60E40/DCP, and S40E60/DCP.

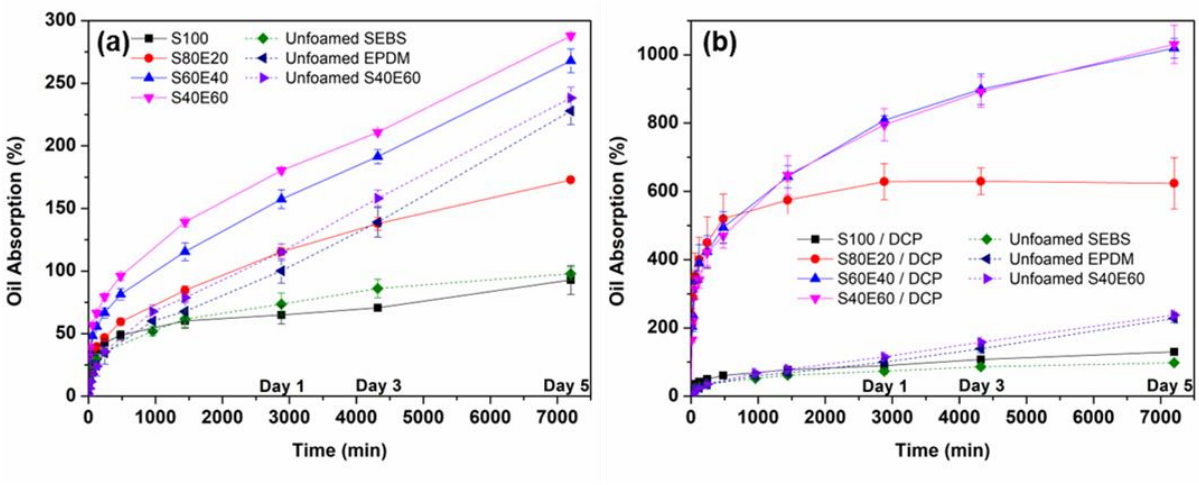

Fig. 3.7. (a) Oil absorption (%) of SEBS/EPDM foams and (b) SEBS/EPDM/DCP foams.

Notably, incorporating EPDM was also conducive to maintaining the foam shape after being immersed in the oil. **Fig. 3.8 (a)** shows the original foam samples cut in a square before immersion in the oil, and **Fig. 3.8 (b)** presents the foam samples after 5 days of the oil absorption. In **Fig. 3.8 (b)**, the foam samples with low EPDM content (S100, S100/DCP, S80E20, and S80E20/DCP) became sticky and partially dissolved in the oil, whereas the foam samples with higher EPDM content (S60E40, S60E40/DCP, S40E60, and S40E60/DCP) maintained their original foam structure with good stability. Since the midblock (ethylene-butylene) of SEBS is soluble in oil [158], this segment allowed the polymer to absorb oil effectively; however, it also led to SEBS being partially dissolved in the oil and deformed the polymer shape. On the other hand, the crosslinked polymer chains of the EPDM matrix made the polymer resistant to dissolution and maintained its structural integrity in the oil. Therefore, S60E40/DCP and S40E60/DCP exhibited remarkable oil absorption performance due to the high oil-dissolving ability of SEBS,

accompanied by the ability to preserve the structural integrity owing to the crosslinked EPDM matrix.

In addition to the similar rheological properties of SEBS and EPDM, both elastomers are inherently hydrophobic and lipophilic. Water contact angle (WCA) measurement illustrated in **Fig. 3.8 (e-f)** demonstrated the hydrophobicity of the SEBS/EPDM/DCP foams with the S60E40/DCP and S40E60/DCP formulations exhibiting water contact angles of 119.6 °, and 113.5 °, respectively. Previous research has paid attention to these features of both polymers and studied to utilize and enhance the hydrophobic and oleophilic properties for a range of applications [30,183–186]. Thus, it is reasonable to expect that SEBS/EPDM/DCP foams could provide excellent oil/water separation attribute. **Fig. 3.8 (c-d)** shows the oil removal of S60E40/DCP and S40E60/DCP in an oil/water mixture. The result showed that 3.5 mL of blue-colored oil was successfully removed from the surface of the water, using 1 g of each foam sample for 30 seconds. Along with the outstanding oil absorption ability, the complete oil-separating performance from water demonstrated the material's great potential to be utilized for oil spill cleanup.

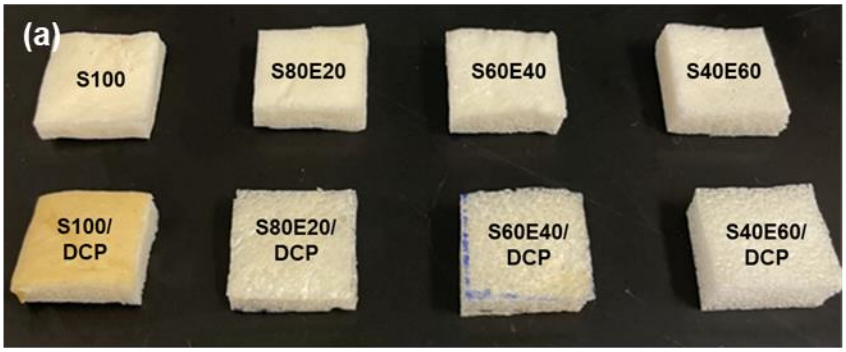

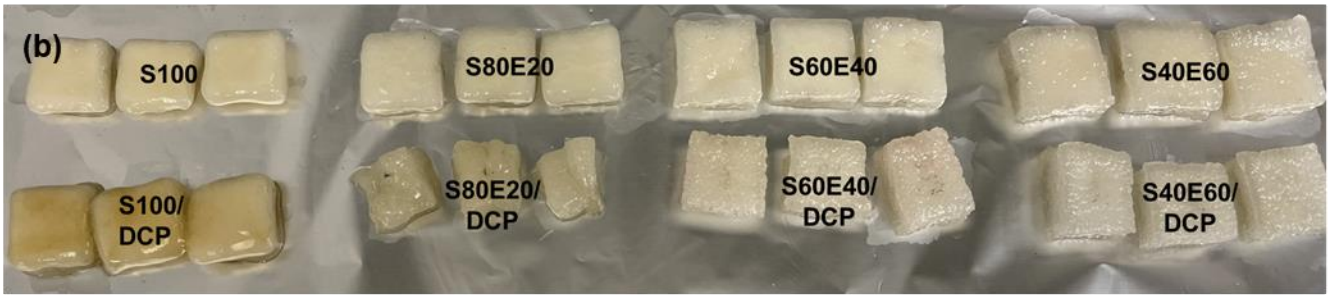

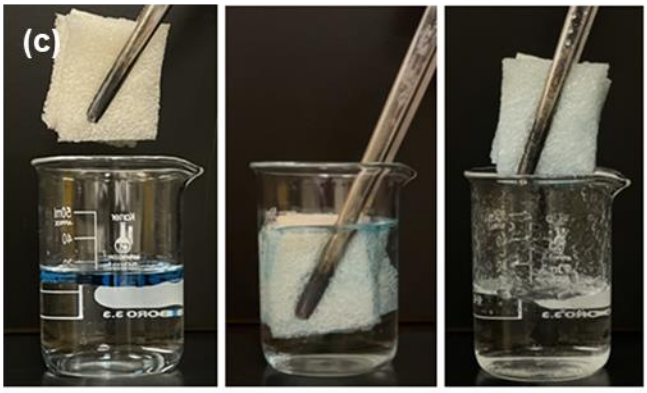

S60E40/DCP

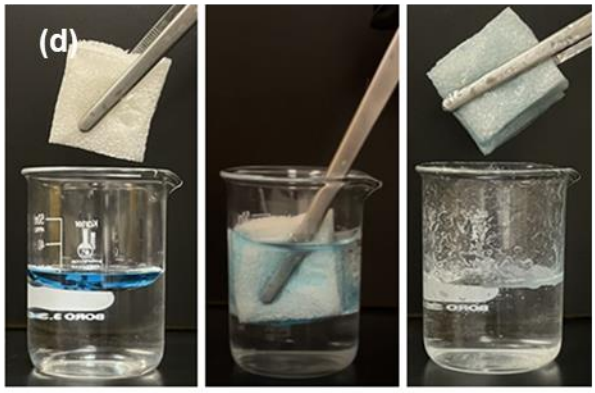

S40E60/DCP

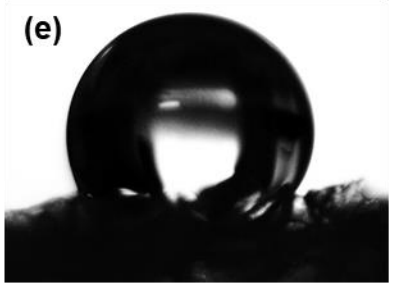

S60E40/DCP
WCA 119.6 ± 2.0 °

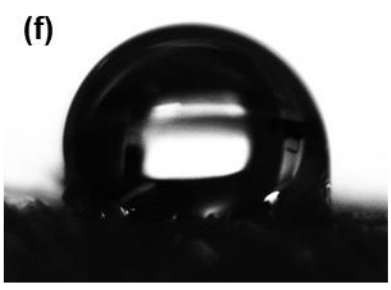

S40E60/DCP
WCA 113.5 ± 1.6 °

Fig. 3.8. (a) Foam samples prepared for the oil absorption test; (b) Foam samples after 5 days of oil absorption; (c-d) Oil/water separation test of S60E40/DCP and S40E60/DCP; (e-f) Water contact angle of S60E40/DCP and S40E60/DCP.

3.4. Conclusion

In conclusion, we have successfully fabricated SEBS-based rubber foam modified with EPDM and DCP as a high-performance oil-absorbing material. It was observed that the incorporation of 40 wt.% or higher amount of EPDM in the SEBS matrix had a significant foaming expansion effect with a 1200 vol.% volume change. The peroxide (DCP) mediated crosslinking enhanced the melt strength of the SEBS/EPDM blend and thus allowed the foam to possess higher mechanical strength as well as large-sized cell pores with well-defined cell structure. The large pores facilitated capillary action and contributed to high oil absorption (up to 1030 wt.%). Furthermore, this novel SEBS/EPDM/DCP foam exhibited excellent oil/water selectivity as well as high oil resistance, indicating that it can serve as an efficient oil absorbent for the remediation of oil-contaminated water. Post oil absorption, the crosslinked elastomer foam maintained its morphology, indicating its potential for reusability. Overall, this work indicated a new approach for the fabrication of elastomer foams using a solvent-free, scalable, and industry-proven melt compounding and molding process to generate highly efficient oil-absorbing materials.

Chapter 4: Thermoplastic Elastomer Melt-blown Fibers for Oil Spill Remediation: Fabrication, Oil Uptake, and Gel Formation Studies.

4.1. Introduction

As industrial growth and urbanization continue to drive the demand for petroleum, this vital fossil-fuel resource has become integral to the global economy. However, petroleum extraction, transportation, and processing pose significant environmental and economic challenges, including oil spills and the release of oily wastewater [4–6]. Consequently, developing highly efficient oil/water separation methods is crucial to mitigate these adverse effects. Unfortunately, traditional remediation methods, including dispersion, solidification, thermal remediation, and bioremediation, have limited efficiency and the potential to generate secondary pollution [187]. In response to these limitations, researchers have shifted their focus toward exploring sorbents and membranes with distinct wettability properties, as these show potential for improved oil/water separation selectivity and increased efficiencies [188,189].

Melt-blown fibers, ranging from micro- to nano-scale fiber diameters, demonstrate remarkable efficacy as oil-separating membranes or sorbents, owing to their large surface area and porous structure [190,191]. Melt-blowing is a polymer manufacturing process technology that produces ultrafine fibers from thermoplastic resins. The method involves melting a polymer resin, extruding it through small nozzles, and using high-velocity fluid to break the polymer stream into droplets that solidify into fibers upon contact with a conveyor or collector screen [96,98]. Upon cooling, the resulting fibers adhere to one another, forming a porous fiber mat. The melt-blowing process

necessitates feeding materials of high melt flow index (MFI), as it allows for easy extrusion and drawing of fine fibers [124,192]. A high MFI signifies lower polymer viscosity and enhanced flow upon heating, which is crucial for effectively stretching and rapidly solidifying molten polymers into fine fibers [193]. The polymers with high MFI allow for a smooth and efficient process with consistent and high-quality fiber production.

Recent advancements in polypropylene (PP) melt-blown fiber research have led to significant improvements in oil/water separation applications. A variety of innovative melt-blown membranes have been developed, including those based on pure PP [137], magnetically enhanced PP [194], PP/PET [191,195], PP/PEG [190], and PP/TiO_2 [139] composites. The employment of PP in the production of fibers results in improved oil separation performance since PP naturally resists water and selectively attracts oil. Non-woven PP fibers demonstrate distinct porous web structure with excellent wetting properties, oil/water separation efficiency, stability, and structural integrity after oil adsorption [137]. The employment of PP based non-woven geotextiles to prevent ground water contamination from leaked petrochemicals from containers and storage facilities has also attracted substantial interest, due to their excellent oil sorption capabilities [196].

However, PP melt-blown fibers designed for oil spill remediation rely on oil adsorption as their primary mechanism for oil uptake. Oil adsorption entails the accumulation of oil molecules on the fiber surface, where they adhere through physical interactions rather than molecular-level chemical interaction or bonding, and without penetrating the material's internal structure[197,198]. A significant challenge associated with oil-adsorbing materials is that upon reaching their saturation point, they can no longer adsorb additional oil, potentially allowing excess oil to disperse or leak.

Moreover, additional osmotic pressure from water or other solvents could also leach the adsorbed oil. For instance, oil leaks from large oil containers require that the sorbent material provide effective oil sorption and sealing until the leak is mitigated [199,200]. Thus, there is a high demand for materials that can chemically and physically interact with sorbent to capture oil spill and provide sealing.

Styrene-ethylene-butylene-styrene (SEBS) is a thermoplastic elastomer (TPE) derived from hydrogenating a styrene-butadiene-styrene (SBS) block copolymer, transforming carbon-carbon double bonds in the butadiene moiety into ethylene-butylene blocks [201]. This triblock copolymer consists of rubbery ethylene-butylene mid-blocks and glassy styrene end blocks [202]. The mid-blocks dissolve in oil, while the end blocks do not, allowing the polymer to capture oil without entirely dissolving as a liquid [158]. As a result of the interaction between oil and the material, a solidified gel can be created. This phenomenon is known as gelation. Such gels self-assemble by non-covalent interactions, such as van der Waals interactions, π- π stacking, and hydrogen bonding [203]. Gelation is a method used for oil spill cleanup by selectively congealing oil from oil/water mixtures. By immobilizing oil, the gelation method facilitates oil removal from the water without further dispersing the oil throughout the water column [74,204]. A key advantage of gelation is that the formed gel creates a barrier, restricting additional oil spread even when the material becomes saturated with oil [199,200].

In this study, the employment of SEBS-based melt-blown fibers was explored by leveraging the selective oil gelation properties of SEBS and the enhanced surface area provided by melt-blown fibers, aiming to achieve exceptional oil/water selectivity. Notably, only a handful of studies have

investigated the melt-blowing of SEBS, highlighting the novelty of this work in the field [204,205]. This is likely because the melt-blowing process of SEBS fibers is challenging owing to the material's low MFI and sticky elastomeric behavior. While high MFI PP (typically 800 - 1800 g/10 min) is readily available for the melt-blowing process, SEBS typically has low MFI (3 - 25 g/10 min) owing to its high molecular weight. This limited melt-processibility of SEBS can cause complications in the melt-blowing process. In this study, high MFI PP was blended with SEBS at low concentrations to compensate for the low MFI SEBS and improve the melt-blowing processibility. The optimization and characterization of SEBS-based melt-blown fibers as well as the effects of blending PP with SEBS on melt-blowing processability and fiber quality were evaluated. Furthermore, the study examined the oil/water separation performance and gelation properties of the resulting SEBS-based melt-blown fibers, providing insights into their potential applications for oil spill mitigation.

4.2. Materials and methods

4.2.1. Materials

Maleated styrene-ethylene-butylene-styrene (SEBS) (KRATON FG1924 GT, styrene content 13 wt.%, maleation level of 0.7-1.3 wt.%, solution viscosity 19,000 cps, M_W ~150,000 g/mol) was provided by Kraton (TX, USA). Polypropylene (PP) (Metocene MF650Y with M_W= 72,500 g/mol) was sourced from LyondellBasell Industries (TX, USA) [206]. FR3 oil (vegetable oil) was purchased from Cargill (MN, USA). Water soluble dyes (Methyl orange and Brilliant Green) and Oil soluble dyes (Oil Red EGN and Oil Blue N) were obtained from Sigma-Aldrich (MO, USA).

4.2.2. Methods

4.2.2.1. Blend extrusion

The SEBS was physically mixed with powdered PP, dried at 80 ℃ for 24 h to remove residual moisture, and equilibrated in an air-sealed container for at least another 24h prior to use. The SEBS/PP blend formulations with high SEBS content (80 -100 wt.%) were listed in **Table 4.1.** Blend mixtures of SEBS and PP were fed (~ 5 g/min) into a twin-screw extruder (Process 11 Parallel Twin-Screw Extruder, Thermo Fisher Scientific) with a screw speed of 70 rpm. The extruder had a maximum processing temperature of 175 ℃ and a temperature profile of 120/140/160/165/170/170/165/160 ℃ from the feed to extruded die. The blended extrudates were then air-chilled, pelletized, and conditioned in zip-lock bags at ambient temperature.

Table 4.1. The material composition of SEBS/PP blends.

	Sample name	**SEBS (wt.%)**	**PP (wt.%)**
SEBS/PP fibers	S100	100	0
	S90P10	90	10
	S80P20	80	20
	P100	0	100

4.2.2.2. Melt-blowing

A custom melt blowing die was designed that fits the horizontal twin-screw extruder set-up. **Schematic 1(a)** illustrated the melt-blowing set up. The twin-screw extruder was used to heat and extrude the polymer melt through the melt-blowing die at a controlled rate. The temperature and

screw speed of the extruder was set at 300 ℃ and 150 rpm, respectively. The melt-blowing die configuration was comprised of a jet angle cap, a melt feed nozzle, and a gas feed, as demonstrated in **Schematic 1 (b).** This configuration of the gas flow direction and the customized designed die resembled Exxon slot dies, which are commonly used for industrial melt-blowing applications [207]. The outer angle cap consisted of a single outer hole diameter of 2.5 mm and an impinging air jet angle of 128° that allows the generation of blown fibers by heated N_2 gas. The inner nozzle contains a single inner capillary with a diameter of 1 mm, a capillary length of 8 mm, and a die-setback distance of 1.5 mm. The temperature feed was connected to an air feed with nitrogen (N_2) inlet jet temperature source, in which the jet temperature was controlled to a temperature of ~350 ℃ through a transformer (Powerstat® Variable Transformer) connected to a 750 W heating torch located upstream of the melt blowing die (Laramy Products, Lyndonville, VT, USA).

The gas volumetric flow rate (0.5 L/min) was calculated and adjusted based on the gauge pressure of inert nitrogen gas (N_2) located upstream of the air heating element. The fiber collector consisted of an aluminum sheet-covered conveyor belt that rotates at 60 rpm and was placed at a die-to-collector distance (DCD) of ~40 cm to ensure proper fiber solidification. The solidification of fibers was assisted by employing a gas-cooling system (mechanical cooling gun) employed close to the fiber collector. Based on preliminary optimization, a feed rate of 3.5 g/min was employed in the extruder to obtain uniform fibers.

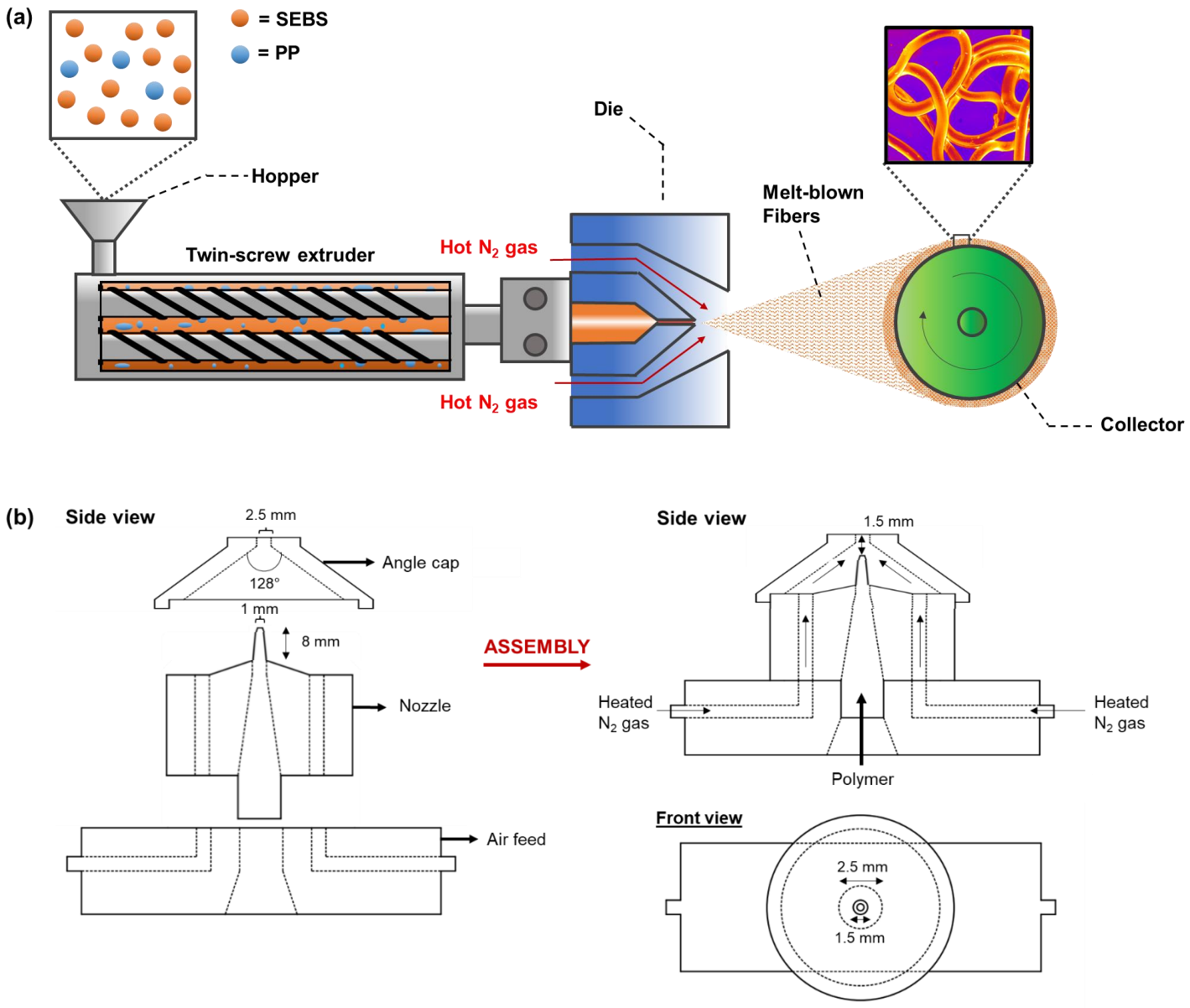

Schematic 1. (a) Schematic procedure of fabricating the melt-blowing of SEBS/PP fibers, and (b) Schematic of the melt-blowing die assembly

4.2.2.3. Fiber characterization

Fourier transform infrared spectroscopy (FTIR)

The blending of SEBS with PP, as well as the interaction of the non-woven fibers with oil were characterized at ambient temperature using a Fourier transform infrared spectrometer (FTIR, Nicolett 6700, Thermo Scientific Inc.) (**Fig. A2** in **Appendix A**). All samples were prepared by placing the specimens directly atop the attenuated total reflection (ATR) accessory and pressed to ensure direct contact with the crystal. FTIR scans, in transmittance mode, were recorded in the range of 4000 to 500 cm^{-1} under the same conditions as the background.

Capillary rheology

The melting rheological parameters (melt viscosity, shear stress, and shear rate) of SEBS/PP blends were generated from a dual-bore piston-type capillary rheometer (Rosand Advanced RH2000, Malvern instrument). The samples were dried at 120 ℃ for 2 hours to remove moisture prior to the measurement. To evaluate the flow behavior of the polymer flow under melt-blowing processing conditions, the capillary rheometer was operated at 300 ℃ in the shear rate range of 20 to 10,000 s^{-1}. The L/D ratio and the diameter of the capillary in one bore were 16/1 and 1 mm, respectively, whereas the orifice die in another bore was a near zero-length capillary. Standard Bagley and Rabinowitch corrections were applied during the measurement to account for the pressure drop effect of the molten polymer when entering the capillary.

Melt flow index (MFI)

The melt flow index of SEBS/PP blends was measured using a Dynisco-Kayness polymer testing system (LMI4000, Frankiln, MA, USA) in accordance with ASTM D1238 with a load of 2.16 kg. The MFI measurement was conducted at two temperatures: 230 ℃ and 300 ℃

Polarized optical microscopy (POM)

Polarized optical microscope images were collected using an Olympus BX53M microscope. Fiber samples were held in place between glass slides and observed at 10x magnification. Fiber diameter was determined using the Olympus Stream Basic software measuring tool. Approximately 90-150 fiber diameters were individually measured to determine the diameter distribution of the fibers.

Scanning electron microscopy (SEM)

The surface morphology of the fiber samples was examined using field emission scanning electron microscopy (FESEM) (FEI Quanta Feg 250, Oxford Instrument) at a 20 kV voltage. Observations were conducted at a 100x magnification level. **Fig. A3** in **Appendix A** displays the obtained SEM images.

Statistical analysis

Any replicate data in this work was presented as mean ± standard deviation. A significance level of $\alpha < 0.05$ was employed. Statistical differences in data were determined using one-way analysis of variance (ANOVA).

2.2.4. Evaluation of fiber interactions with oil and water

Oil sorption and gel formability test

Three specimens of each non-woven fiber mat composition, weighing ~ 0.5 g each, were accurately measured and then placed in a plastic container. Next, 2.5 g of oil was added to the container, allowing the samples to ab/adsorb the oil. After waiting for 1 minute of sorption, the

fiber mat sample was removed from the oil, and allowed to drain the excess oil drop. The oil sorption capacity was then determined via weight difference, as depicted in Equation (4.1).

$$Oil\ sorption\ (\%) = \frac{W_1 - W_0}{W_0} \times 100 \tag{4.1}$$

Where W_0 is the original weight of each fiber mat sample and W_1 is the weight of the sample after oil sorption.

Following the oil sorption test, each fiber mat sample was placed back into the container and allowed to rest at ambient temperature (21 ℃) for 1 day to evaluate gel formation. Once gelation occurred, the fiber mat samples were noted to display semi-solid gel morphology. The weight of the semi-solid fiber/oil gel was measured to evaluate the gel formation capacity of each fiber mat sample. Similarly, the gel formation capacity was calculated based on Equation (4.2).

$$Gel\ formation\ capacity\ (\%) = \frac{W_2 - W_0}{W_0} \times 100 \tag{4.2}$$

In this equation, W_0 represents the initial weight of each fiber sample, and W_2 signifies the weight of the solid fiber/oil gel.

Oil penetration test

S90P10 and P100 fiber mats were prepared and immersed in oil baths. To ensure saturation (both samples) and gel formation (S90P10), the fiber samples were left in the oil baths for one day. Following oil immersion, each oil-containing mat was weighed (all samples displayed similar weight and volume). The saturated fiber mats were then placed on circular felt pads positioned on

Buchner funnels. FR3 oil (dyed blue) was poured onto each fiber mat, and oil penetration was monitored for 1 hour.

Afterward, the collected oil was removed, and water (dyed yellow) was poured onto both P100 and S90P10 samples. Water penetration was observed for another 1 hour.

Water contacts angle

The water contact angle for SEBS/PP fibers was determined using the sessile drop technique. A 4μL droplet of deionized water was placed on each fiber mat. Images of the droplets were taken 1 s after dispensing the water. 1 s was selected to ensure that the water does not percolate into the mat prior to the measurement. To measure the contact angle of each droplet, the ImageJ contact angle plugin (Drop analysis – LB-ADSA) was utilized.

Oil/water selectivity test

A mixture of oil/water with a 1:6 oil-to-water weight ratio was prepared with the oil dyed red and the water dyed blue. This oil/water mixture was subsequently poured onto a fiber mat (S90P10) placed on a Buchner funnel. The oil and water were separated through gravitational force upon pouring. The filtration device was observed overnight to check for any potential oil leakage. The oil/water selectivity was determined using the equation provided (Equation (4.3)).

$$Oil/water\ selectivity\ (\%) = \frac{W_{oil}}{W_{o/w}} \times 100 \tag{4.3}$$

Where $W_{o/w}$ is the weight of oil in the oil/water mixture and W_{oil} is the weight of oil captured in the fiber mat. A minimal amount of oil adhering to the inner surface of the beaker was neglected.

Parallel plate rheology

The rheological properties of the fiber/oil gel were studied using parallel plate rheology (HAAKE MARS III Rheometer). The linear viscoelastic region (LVR) analysis was conducted to determine the strain of 1% for oscillation frequency sweep. Frequency oscillation ramp tests were then performed using a 20 mm diameter disc and a gap width of 1 mm over a frequency range from 100 to 0.1 Hz at 25 ℃.

To evaluate the gelation, the SEBS/PP fiber mat samples were positioned on the rheometer plate and oil equal to 2.5 times the sample's mass was applied directly to the fiber sample's surface. Subsequently, a frequency sweep test was initiated to assess the change in rheological properties as the gel formation occurred. Separately, the rheology of the fiber mat/oil solid gel was evaluated. For this, the fiber mat/oil gels were prepared by combining the designated weight ratio of oil and each fiber sample (Fiber: oil weight ratios of 1:2.5 and 1:5). After 1 day of gelation, the rheological properties of the semi-solid fiber/oil gels for each oil ratio were evaluated.

4.3. Results and discussion

4.3.1. Rheology and melt flow analysis

In the melt-blowing process, the polymer is typically processed through a small capillary nozzle and stretched out into microfibers by applying hot gas. Thus, it is essential to investigate the processing behavior of the formulations (S100, S90P10, S80P20, and P100) through a small nozzle via capillary rheology analysis that resembles the extrusion process for the melt-blowing operations. The variation in the corrected shear viscosity versus the corrected shear rate of the

blends was collected and displayed in **Fig. 4.1 (a)**. Overall, all the fiber materials showed a strong shear thinning or pseudoplastic behavior, in which the shear viscosity linearly decreased over the increasing shear rate, which is a typical behavior of thermoplastic materials [208,209]. The linear curves over the entire range of processing shear rate implied that the polymer flow adhered to the classic power law relationship, which can be expressed as Equation (4.4) [210].

$$\eta = K\,\dot{\gamma}^{n-1} \tag{4.4}$$

In which, η and $\dot{\gamma}$ are the shear viscosity and the shear rate, respectively. K and n represent the consistency and power-law indexes, respectively.

The K and n values are shown in **Table 4.2** for the respective polymer blends. Overall, it was observed that the power-law index all exhibited values below one (n < 1), confirming the pseudoplastic nature of the system. The consistency index (K) value declined as the concentration of P100 increased in the binary blends, which signified that S90P10, S80P20, and P100 had lower shear viscosity and higher fluidity over the entire shear rate range compared to pure S100 material.

Table 4.2. Consistency (K) and power-law (n) indexes of SEBS, PP, and SEBS/PP blends.

Sample name	Consistency index (K)	Power-law index (n)
S100	14001	0.020
S90P10	3678	0.024
S80P20	2750	0.034
P100	2236	0.024

It was evident that the reduction in the shear viscosity of SEBS was directly correlated to the loading concentration of PP in the binary blend formulas. The shear viscosity curve of S90P10 significantly decreased over the corrected shear rate range, indicating that a low PP loading (10 wt.%) can effectively improve polymer flow. By functioning as a lubricant, it facilitated the extrusion of S90P10 and aided the overall melt-blowing process. On the contrary, there was only a slight reduction in shear viscosity of S80P20 as compared to S90P10 fibers, indicating that additional PP loading in the 20 wt.% did not have a significant lubricating effect on the melt viscosity of SEBS, and about 10 wt.% PP loading could be optimal. Relatively poor compatibility of PP with the SEBS could also be the reason for the observed lack of rheology change at higher PP loading. It is important to highlight that despite the maleation of SEBS, the high MFI PP (low molecular weight and viscosity) and SEBS (high molecular weight and viscosity) are expected to generate inferior compatibility, due to the high viscosity difference (ratio) than inhibit the dispersion of PP in the SEBS matrix during melt-mixing [211].

The shear stress versus shear rate curves for these samples was also displayed in **Fig. 4.1 (b)** to further investigate the flow behavior of the binary blends at 300 ℃. As anticipated, SEBS exhibited much higher shear stress than PP over the studied shear rate ranges, which was attributed to the high elasticity of the sample. With only small loading incorporation of PP, the blends of S90P10 and S80P20 have shown considerable reduction in shear stress, which further showcased the lubricating effect of PP in the binary blend formulations.

The flow behaviors of the S100, S90P10, S80P20, and P100 samples through a nozzle were further analyzed by evaluating the MFI, which is another way to quantify the amount of

polymer flowing through a capillary under specific temperatures and weights. As a rule of thumb, the MFI required to produce melt-blown fibers should range from 15 to 3000g g/10 min [212]. The MFI measurement was performed at 230 ℃ and 300 ℃ to validate the melt-processability of all melt-blowing materials during melt-blown extrusion.

It was observed that S100 displayed low MFI values (10.2 g/10 min) at 230 ℃, which would indicate a poor melt flow through the capillary and be considered a challenging material for melt-blowing processes. This could inhibit the ability of the softened polymer to form a fine fiber structure as the extrudate would not be able to stretch out into thin lines in the nozzle. On the other hand, P100 possessed tremendously high MFI values, which were 1240.8±132.5 and 1740.2±82.3 g/10min at 230 ℃ and 300 ℃, respectively. The high MFI of P100 was accredited to its low molecular weight and melt viscosity, which inherently makes the material more suitable for melt blowing and blending it with SEBS can facilitate the melt-blowing operation of SEBS [213]. This, in turn, contributes to the production of more uniform non-woven webs. At 230 ℃, the MFI of the blend increased proportionally with the addition of PP. The MFI values rose from 10.2±0.6 g/10min (S100) to 20.1±1.8 g/10min (S90P10), and further to 41.1±1.4 g/10min (S80P20). This trend signifies that the presence of PP effectively enhanced the flow of SEBS, doubling its MFI for every 10 wt.% loading increment. The hydrogen bonding between the compatibilizer's MA groups in SEBS and the methyl groups of PP may contribute to the enhanced interfacial adhesion among polymer chains. This interaction allows the triblock polymer SEBS to display better flow properties and reduced molten polymer viscosity, facilitating a smoother flow during processing at elevated temperatures [214,215].

To aid with the melt-blowing process of pure non-woven fibers of S100, the processing must also be run at an elevated temperature (300 ℃) to achieve a high MFI (116.6 ± 2.3 g/10 min), that can be amenable for melt-blowing operation (Figure 1c). Similarly, the S90P10 and S80P20 blends also exhibited high MFI at elevated temperatures. Overall, the prohibitively low MFI at lower temperature ranges and high MFI observed at 300 ℃ indicated that the melt-blowing extrusion need to be carried out at elevated temperature (~300℃) to generate non-woven fibers of SEBS.

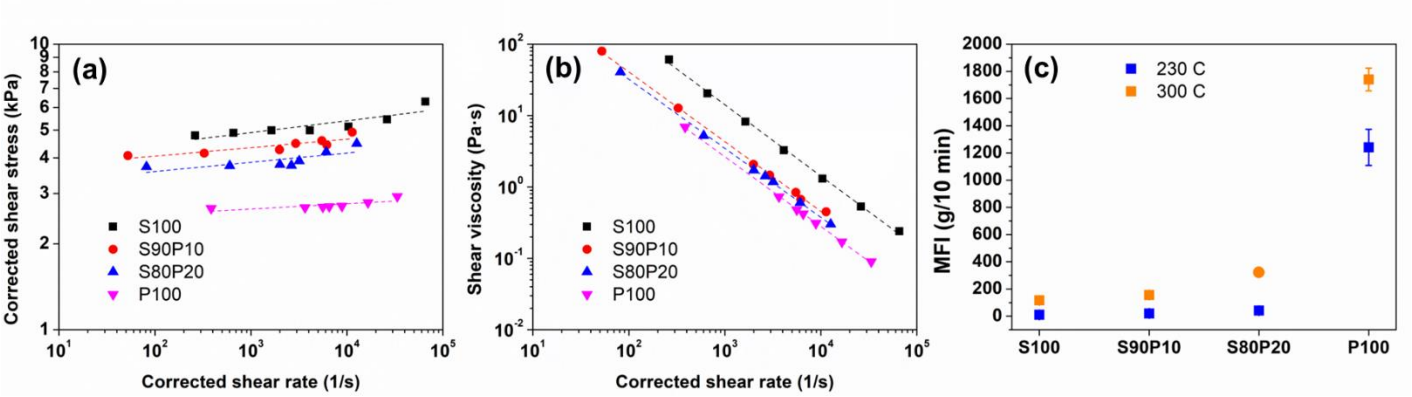

Fig. 4.1. Flow curves indicating (a) Shear viscosity and (b) shear stress of S100, S90P10, S80P20, and P100 fibers as a function of shear rate; (c) Melt flow index of S100, S90P10, S80P20, and P10 fibers at 230 and 300 ℃.

4.3.2. Melt-blowing process

The melt-blow processing of SEBS/PP blends was monitored to examine the effects of PP as an additive in the production of melt-blown SEBS fibers. It is important to note that SEBS has not been extensively investigated for melt-blowing applications due to its high viscosity (low MFI),

the need for high processing temperature, and high elasticity and stickiness, which all can result in limited processing windows. In this study, we demonstrated a successful melt-blowing process by employing an elevated processing temperature (300 ℃), with minimal flow instabilities and defects during processing. However, due to the high elasticity and high extensional strain of the copolymer branch, the fiber stream of pure SEBS (S100) during the melt-blowing process still exhibited some limitations, such as a narrow distribution angle and stickiness, as indicated in **Fig. 4.2 (a)**.

Notably, the addition of PP loading at 10 wt.% (S90P10) showed a great improvement in the melt-blowing process of SEBS/PP blends as noted from the smooth fibers and avoidance of drooling/blob at the melt blow die. Furthermore, the angular distribution of the S90P10 melt-blown fiber stream became much more widespread (**Fig. 4.2 (a)**), which helped S90P10 to yield a larger fiber mat area at the collector. This improvement in the melt-blowing process was credited to the enhanced interaction between SEBS and PP in the S90P10 blends, in which PP chains increased the melt flow index (MFI) and reduced the overall melt viscosity of the blend. This reduction corresponded to an increase in MFI, which in turn could potentially yield a more uniform web structure.

On the other hand, it was intriguing to observe that with a 20 wt.% PP loading, the melt-blowing process of the S80P20 blend exhibited spontaneous accumulation of polymer at the die exit, as depicted in **Fig. 4.1 (a).** The occurrence of this phenomenon in the melt-blowing is referred to as "die drool", which could be attributed to the high concentration of volatile components (PP) in the blends [193]. It was assumed that a portion of the SEBS became detached from the rapid fiber

stream of PP and trailed at the nozzle's end. Although a small addition of PP improved the melt-processibility of SEBS, as evidenced by the S90P10 processing, a higher concentration of PP could have a negative impact. This was due to the disparities in the melt rheology and MFI between SEBS and PP [193].

Fig. 4.2 (b) displays a visual comparison of width distribution and fiber web structure of various formulations. Among the produced melt-blown fibers, S100 fibers exhibited the lowest mat width due to the narrow cone stream shape of fibers coming out during processing. On the other hand, formulations containing PP (S90P10, S80P20, and PP) all showed larger fiber mat widths. This suggests that the use of high MFI PP may have lubrication effects that allow the blends to be extruded out of the small capillary more swiftly, thus enhancing the overall output efficiency of the fibers. However, in the case of the S80P20 formulation, even though a large fiber mat was collected, the majority of the SEBS material went to waste as it was lost at the die exit during the processing stage. Also, the accumulated polymer (blob) around the die was sporadically expelled by the hot gas inlet jet, resulting in bead-like formations within the produced fiber mat. **Fig. 4.2 (b)** illustrates closely packed fiber mats in S100 and S9010 formations, however, S80P20 presents a sparse fiber mat in which small beads were interspersed.

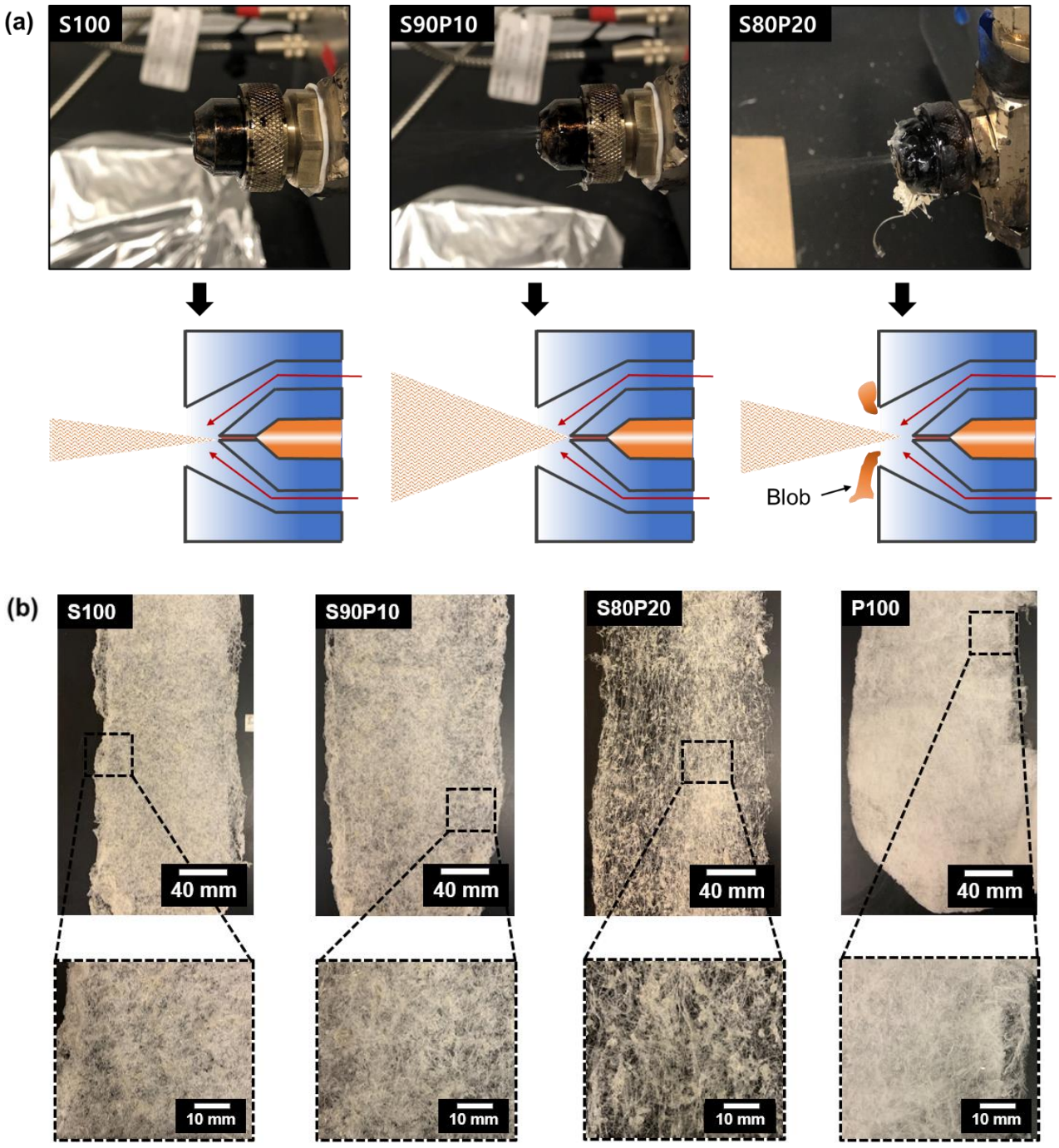

Fig. 4.2. (a) The fiber angle distribution during melt-blowing processing of neat SEBS and SEBS/PP blends; (b) The non-woven fiber mats of neat SEBS, neat PP, and SEBS/PP blends.

4.3.3. Fiber characterization

The morphology of the fiber surfaces was examined using both polarized optical microscopy (POM) (**Fig. 4.3 (a)** and **Fig. A3** in **Appendix A**) and scanning electron microscopy (SEM) (**Fig. A4** in **Appendix A**). Each SEBS/PP fiber was melt-blown at consistent federate (3.5 g/min), temperature (300 ℃), and screw rotation (150 rpm) utilizing a single inner hole diameter of 1 mm. Despite the uniform fabrication method, the fibers exhibited distinct morphologies due to their varying compositions.

The microscopic image of S100 revealed significant variance in fiber diameters. Each large-diameter fiber was surrounded by smaller-diameter fibers of varying sizes. Although the fibers appeared quite dense in **Fig. 4.1 (b)**, the microscopic image showed non-uniform fiber diameters. As depicted in **Fig. 4.3 (b)**, a substantial percentage of the fibers had smaller diameters, with an average fiber diameter (d_{av}) of 51.0 µm. The fibers exhibited a coefficient of variation (CV) of 91.8%, indicating a considerable dispersion in fiber diameters, with the largest fiber diameter measuring up to 270 µm. The addition of 10 wt.% PP in S90P10 appeared to contribute to a more uniform distribution of fibers, as evidenced in the microscopic image and the fiber diameter distribution (**Fig. 4.3 (c)**). The microscopic image displayed reduced entanglement and narrower size distribution compared to S100, which was further supported by an increased d_{av} of 62.1 µm and a lower CV of 63.9%. Upon increasing the PP content to 20 wt% in P80S20, a coarse web structure with small beads embedded in the fiber web was observed (**Fig. 4.1 (b)**), likely due to the "die drool" during the melt-blowing process [193]. However, at the fiber scale, a more even distribution of fiber thickness was apparent, with predominantly thick fibers of similar sizes. The

average fiber diameter rose to 84.0 µm, with a reduced size dispersion (CV = 47.3%). It is noteworthy to mention that the quantity of both the smallest (10 µm) and largest (200 µm) fibers increased, despite the smaller size dispersion. This suggests that at 20 wt.% PP content, the small-sized fibers (~10 µm) were predominantly influenced by the PP phase, while the large-sized fibers (180-200 µm) were primarily governed by the SEBS phase. **Fig. A3** in **Appendix A** shows the creation of fine PP fibers beside S80P20 fibers. The P100 fibers composed of pure PP exhibited a highly disordered orientation and an extremely thin, frizzy structure with a significantly lower average fiber size of 7.13 µm (**Fig. 4.3 (e)**). These excessively frizzy fibers are commonly referred to as "flies," which resulted from extreme melt-blowing conditions [193]. Although a processing temperature of 300 °C and a nitrogen gas inlet jet temperature of 350 °C were appropriate for SEBS melt-blowing, these temperatures led to fiber breakup when processing PP.

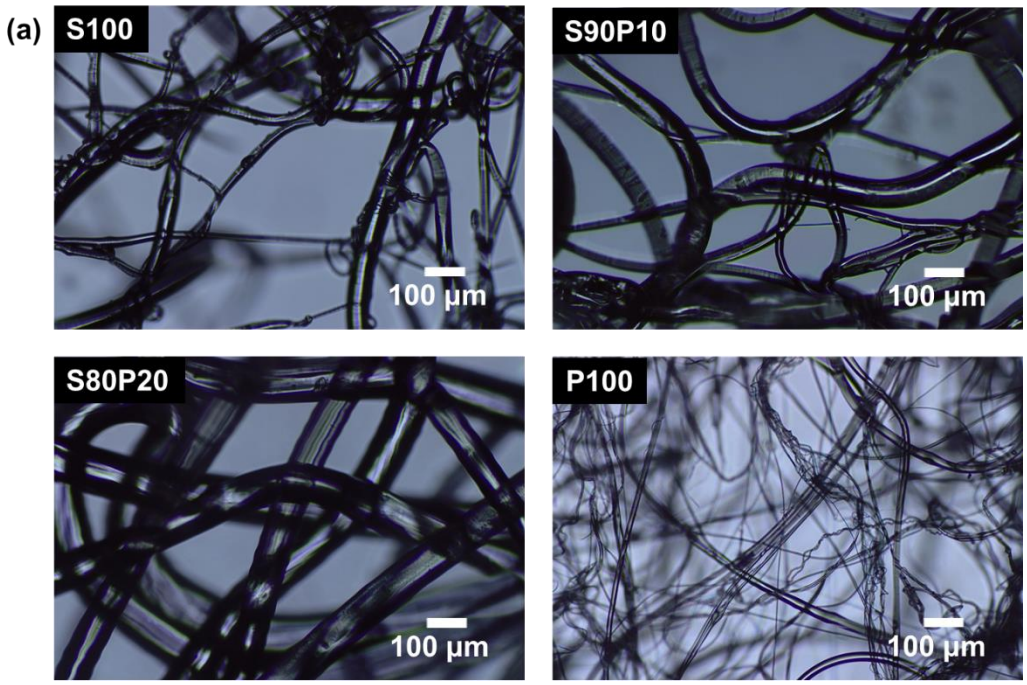

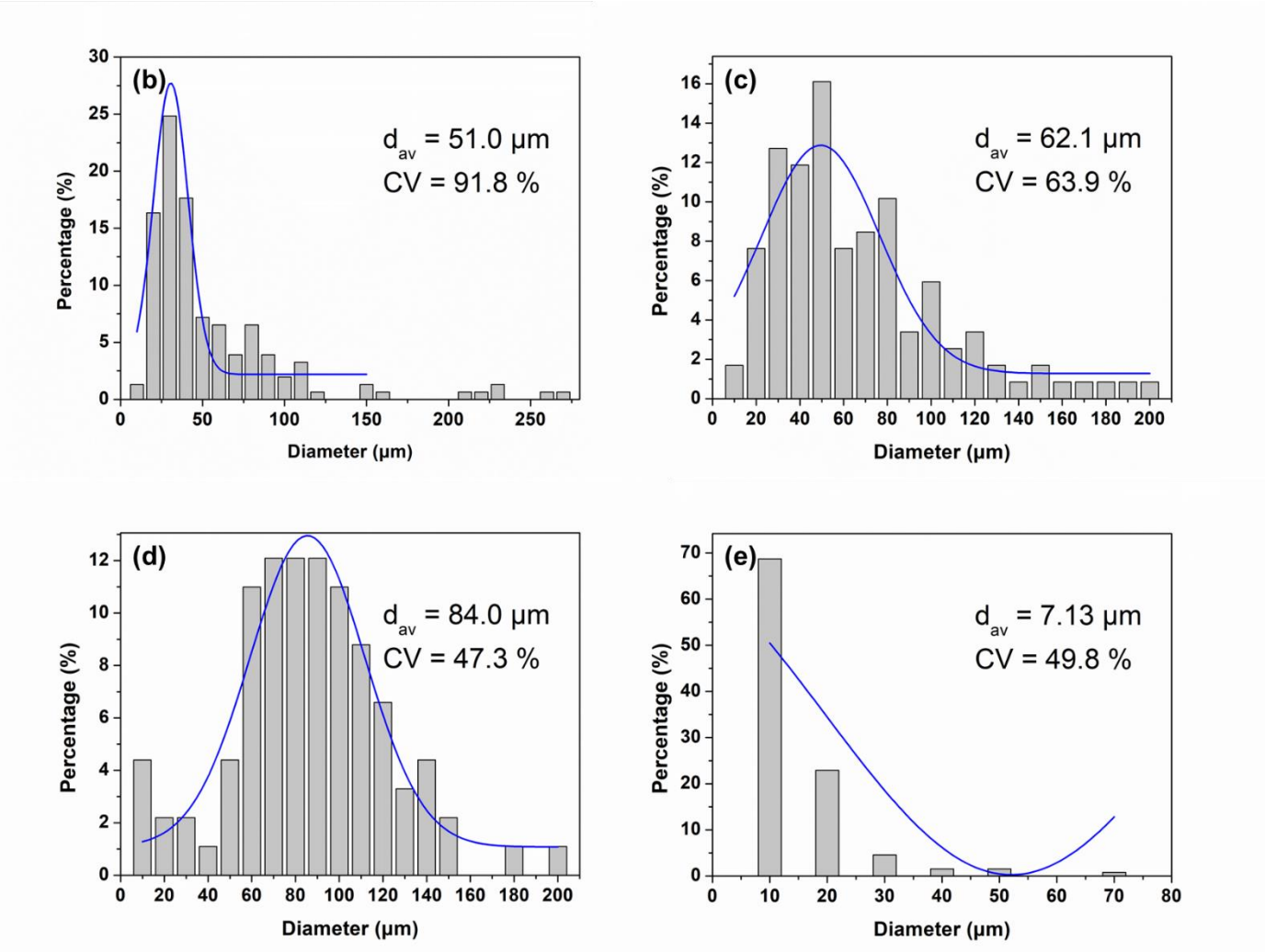

Fig. 4.3. (a) Polarized optical microscope image of SEBS/PP fibers; (b-d) Fiber diameter distribution.

4.3.4. Interaction with oil and water

To gain insight into the influence of varying fiber characteristics resulting from distinct material formulations on oil and water interactions, the SEBS/PP fibers were evaluated using vegetable oil-derived ester (FR3) fluid. It was meaningful to evaluate the fiber interaction with nature-derived

fluid due to the increasing demand for natural ester fluids as substitutes for petroleum oil. As these oils are transported and handled similarly to petroleum oils, using highways, tankers, rail, and vessels, the risk of edible oil spills is also comparable to that of petroleum oil spills [216]. In this section, the immediate oil sorption and gel formation capacities of the SEBS/PP fibers, as well as their selective oil uptake due to their inherent hydrophobicity and oleophilicity, are investigated and compared. Moreover, the rheological properties of the gel formation and the fiber/oil gels were analyzed to better understand their viscoelastic behavior.

4.3.4.1. Oil sorption and gelation

In order to evaluate the impact of varying morphologies of the SEBS/PP nonwoven fibers on the immediate oil sorption capacity, an oil sorption test was conducted as depicted in **Fig. 4.4 (a)**. The fibers were prepared with a weight ratio of 1:5 (fiber: oil) and removed after 1 minute of oil sorption. Upon examination, minimal gel formation was observed, indicating that the primary mechanism driving oil uptake was ab/adsorption rather than gelation when the materials were exposed to oil for only 1 minute. Adhesion between the fibers and oil surface, as well as cohesive forces between oil molecules, may also have contributed as influential factors in the process [217]. The data presented in **Fig. 4.4 (c)** reveals that the sorption capacity varies across the samples. The P100, as anticipated, adsorbed the entirety of the oil, achieving a 500 wt.% sorption capacity. This can be attributed to the P100's ultra-fine fiber diameters and extensive specific surface area, which together offered large binding sites for oil molecules to adhere to. For SEBS-based fibers, S90P10 demonstrated the highest capacity with a value of 405 wt.%, followed by S80P20 at 364 wt.%, and S100 exhibited the lowest capacity at 262 wt.%. The highest oil sorption capacity of S90P10 can

be attributed to its relatively low average fiber diameter (d_{av} = 62.1 μm), uniform fiber diameter distribution (CV = 63.9%), and dense fiber web structure. Although S100 possessed the lowest average fiber diameter (d_{av} = 51.0 μm), the broad fiber diameter dispersion (CV = 91.8%) hindered the uniform oil adhesion throughout the fiber mat. Moreover, despite the uniform fiber diameter distribution of S8020 (CV = 47.3%), the sparse fiber mat and the presence of beads could have negatively impacted the oil sorption performance.

On the other hand, when the SEBS-based fibers were exposed to the oil for a longer period, a gelation process became more pronounced, suggesting a gradual transition from ab/adsorption to gelation as the predominant oil uptake mechanism over time. After 1 day, no visible changes were observed in the gelled fibers. The observation suggested that the gel formation process had most likely reached completion at room temperature (21 ℃). This extended observation period ensured that adequate time was given for all potential gel formation processes, providing a more accurate depiction of the material's performance after prolonged oil exposure.

For S100, S90P10, and S80P20, the semi-solid gel was generated through a gelation process that resulted from the interaction between fibers and oil. When SEBS was exposed to the oil, the oil selectively dissolved the ethylene-butylene mid-blocks without affecting the styrene end blocks. Therefore, while the oil interacted with the SEBS, the rigid styrene end blocks act as physical crosslink sites, leading the SEBS/oil mixture to exhibit the characteristics of a physical gel [158]. As for P100, there was no change in physical structure when comparing the two oil uptake observations after 1 minute to those after 1 day. Since no gel formation occurred, it can be concluded that there was no interaction between the oil and pure PP fibers, and oil adsorption

served as the sole principal mechanism for capturing the oil. Comparing semi-solid gel formation capacity among SEBS-based fibers, S90P10 demonstrated the highest capacity at 351 wt.%, followed by S80P20 at 318 wt.%, and S100 exhibited the lowest capacity at 264 wt.% (**Fig. 4.4 (d)**). Interestingly, the order of gel formation capacity comparison aligned with the order of immediate oil sorption. The uniform and dense fiber web structure of S90P10, coupled with its relatively low average fiber diameter, facilitated a more efficient interaction between SEBS and vegetable oil. This enabled the oil to be more effectively immobilized within the interstices of the polymer matrix through capillary action.

Furthermore, an oil penetration test was carried out to evaluate and compare the oil-immobilizing capabilities of materials employing oil adsorption (PP fibers) against those utilizing gelation (SEBS-based fibers) in their oil capture mechanisms (**Fig. 4.4 (e)**). For this, FR3 oil was poured onto the oil-saturated P100 and S90P10 fiber mats to examine their ability to prevent the spread of excess oil when saturated.

Upon pouring the oil, P100 allowed the oil to pass through, indicating that it could not adsorb additional oil beyond its sorption capacity. This can be attributed to oil adsorption, which serves as the primary oil uptake mechanism for P100. A notable challenge with oil adsorption is that once saturation is reached, the material is unable to adsorb any more oil, potentially allowing excess oil to disperse without being effectively immobilized.

On the other hand, the S90P10 fiber mat effectively sealed the funnel due to the physical gel formed from the interaction between SEBS and oil. When oil was poured onto the mat, none of it passed through. The setup was monitored for an additional hour to detect any potential oil leakage;

however, no leakage was observed. The gel successfully prevented excess oil from penetrating the fiber mat. By creating a barrier, the gel hindered the further spreading of the excess oil, even when it has reached its saturation point.

Subsequently, the collected oil was removed, and water was poured onto both P100 and S90P10 samples (**Fig. A5** in **Appendix A**). After observing for 1 hour, the results revealed that while the water completely penetrated the P100 mat, it did not infiltrate the S90P10 mat and instead accumulated on its surface. This outcome further confirmed the robust sealing effect provided by the S90P10 gel.

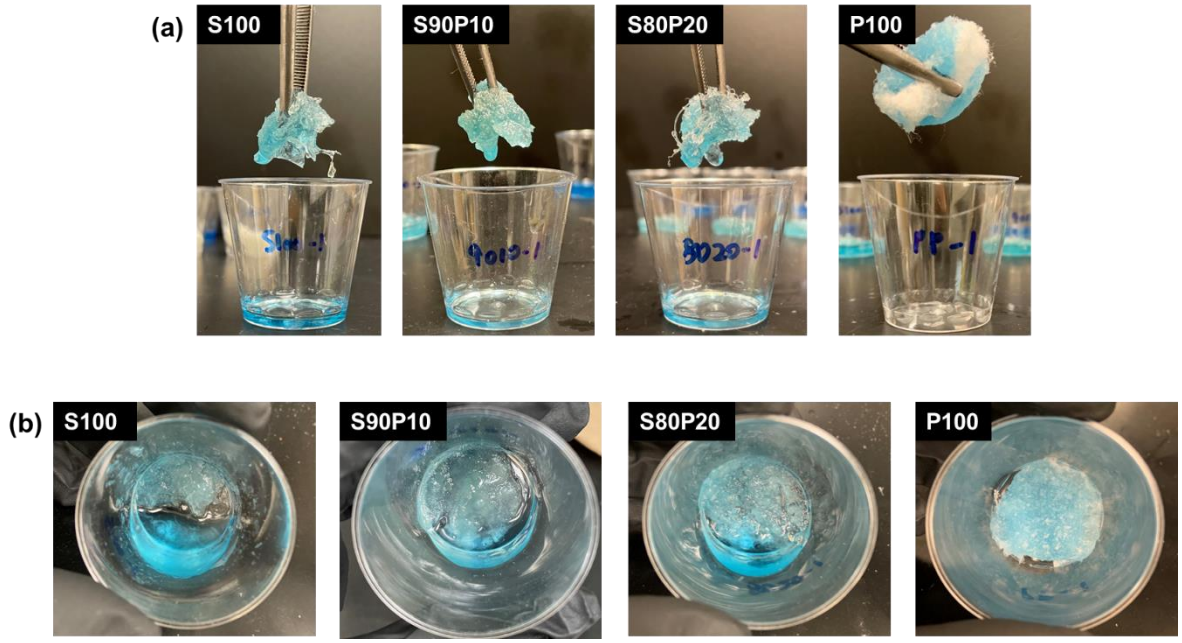

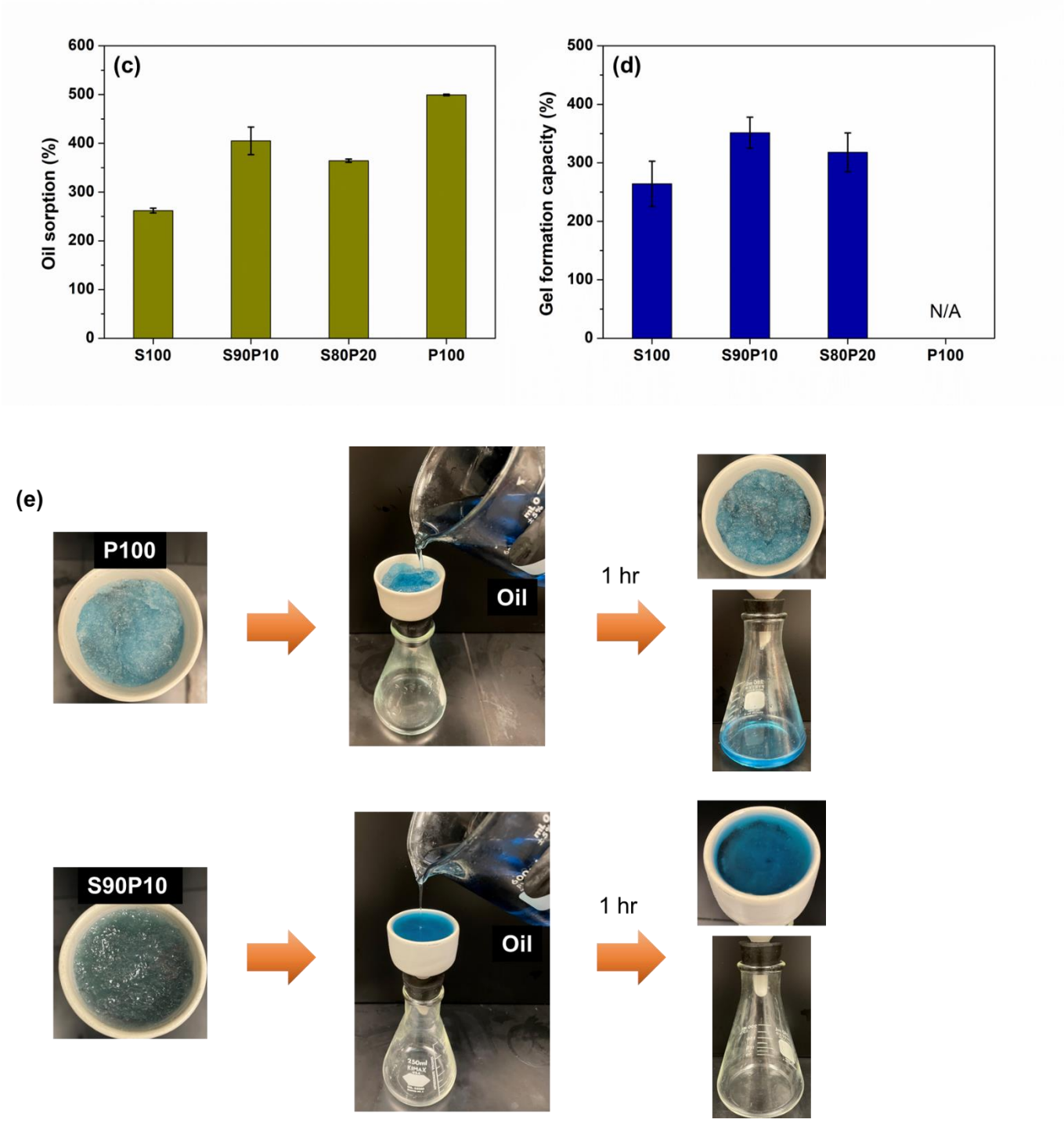

Fig. 4.4. (a) Immediate oil sorption test (1 minute of oil uptake); (b) Gel formation test (1 day of

fiber/oil interaction); (c) Immediate oil sorption capacity and (d) Solid gel formability comparison of SEBS/PP fibers; € Oil penetration test of P100 and S90P10.

4.3.4.2. Rheological study of gelation

The viscoelastic properties of fiber/oil gels in FR3 were investigated using an angular frequency sweep experiment conducted at 25 °C with a fixed strain of 1%. The evaluated parameters included the storage modulus'(G'), representing the elastic or recoverable energy, and the loss modulus''G"), indicative of the viscous or non-recoverable energy. Additionally, complex viscosity (|η*|) was assessed, signifying the overall resistance of a material to deformation when exposed to sinusoidal strain. This can be expressed using Equation (4.5)

$$\eta* = \sqrt{G'^2 + G"^2}/f \tag{4.5}$$

where f is frequency.

Initially, the rheological test for gel formation was carried out by dropping 2.5 times the weight of the oil directly onto the fiber surface, followed by an immediate rheology assessment. The transition from fiber to gel was examined over a frequency range of 100 Hz to 0.01 Hz (high to low frequency). This rheological analysis in **Fig. 4.5 (a-b)** provided a comparison of the viscoelastic behavior of the SEBS/PP fibers as they formed a gel structure from the fibers in response to the added oil. Both S100 and S90P10 displayed identical rheological behavior during the gel formation, as evidenced by the G', G" and |η*| data. However, as the PP content increased, S80P20 exhibited higher G' and G" values, indicating that while a 10 wt% PP content did not cause a change in gel formation behavior, a 20 wt% PP content led to a noticeable shift. This can be

attributed to the formation of a small quantity of neat PP fibers during the melt-blowing process of S80P20. As PP did not interact with oil to create a gel structure, the inclusion of solid PP fibers in the S80P20 gel could result in more solid-like overall mechanical properties.

The rheological properties of the gels with a fiber-to-oil weight ratio of 1:2.5, three days post-gelation, are illustrated in **Fig. 4.5 (c-d),** and those with a weight ratio of 1:5 is shown in **Fig. 4.5 (e-f)**. A semi-solid material can be classified as a physical gel if its storage modulus (G') surpasses its loss modulus (G") during the rheological assessment [218]. For all the fiber/oil gel formulations tested with both 1:2.5 and 1:5 fiber-to-oil ratios, G' consistently exceeded G" across the entire frequency spectrum, indicating that these materials exhibited elastic gel properties within the linear viscoelastic region. It was observed that all the gelled materials (S100, S90P10, and S80P20) with two different oil ratios followed the same trend: G', G", and $|\eta^*|$ gradually increased with an increase in PP content. The results showed that the fiber/oil gel with higher PP content had an overall more rigid structure, resulting in increased resistance to deformation and reduced susceptibility to flow.

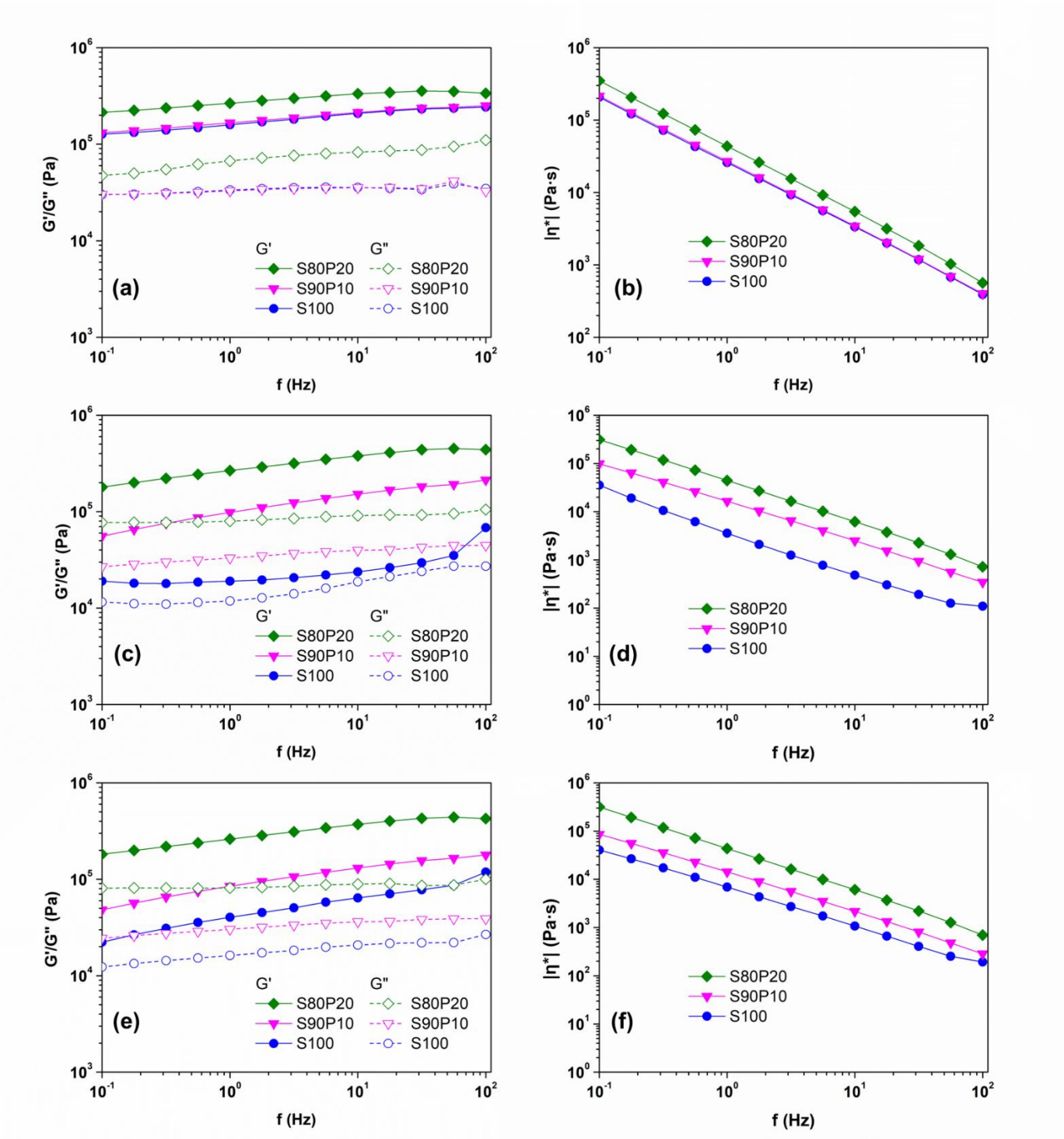

Fig. 4.5. Storage modulus G'(closed symbols), loss modulus G" (open symbols), and complex

viscosity |η*| of (a-b) immediate gel formation, (c-d) Fiber/oil gels (1:2.5 weight ratio), and (e-f) Fiber/oil gels (1:5 weight ratio) of S100, S90P10, and S80P20.

4.3.4.3. Selective oil sorption

SEBS exhibits both oleophilic and hydrophobic properties due to its unique chemical composition. Composed of rubbery ethylene-butylene mid-blocks and glassy styrene end blocks, the long-chain hydrocarbons in the mid-blocks prefer to avoid contact with water molecules, contributing to the material's hydrophobic behavior.

Fig. 4.6 (a) presents the water contact angle (CA) of SEBS/PP fibers. Due to the porous nature of the fiber structure, the fibers permit water to permeate over time. To capture the water contact images before permeation occurs, the images were taken just 1 second after water contact. Melt-blown fibers composed of PP are well known to be hydrophobic [103,137,194]. In our study, SEBS-based fibers exhibited hydrophobicity that was nearly on par with that of the pure PP fibers processed under the same melt-blowing conditions. The highest CA among SEBS-based fibers was observed from S90P10, at 125.5 ± 0.9°, while that of P100 was 129.4 ± 3.4°. S90P10 exhibited the highest CA among the SEBS-based fibers, followed by S100 (120.6 ± 0.9°) and S80P20 (111.0 ± 1.4°). The relatively high CA for S100 and S90P10 compared to S80P20 can be attributed to their denser fiber web structure. The reduced melt-processability of S80P20, owing to excessive PP content, led to a more loosely packed web structure and caused the water droplet to spread further. Also, the different surface roughness of each fiber mat can influence the water contact angles.

Moreover, the oil/water selectivity test was conducted as illustrated in **Fig. 4.6 (b),** in which the oil and water were colored with red and blue dyes, respectively. An oil/water mixture (1:6 weight ratio) was poured onto 3.5 g of each SEBS/PP fiber mat (**Fig. 4.6 (b)** showing S90P10) positioned on the Buchner funnel. Utilizing gravitational force, the combined weight of 73 g of oil and water was separated within 1 minute, particularly, the red-color oil was retained completely in the fiber mat while the blue-color water was completely filtered through. The result showed that S90P10 showed nearly 99 % oil/water selectivity (ignoring a minimal amount of oil adhering to the flask wall) with no residual oil observed in the filtered water. The oil/water separation results for various fiber formulations are depicted in **Fig. A6** in **Appendix A**. Among them, S80P20 exhibited the lowest oil/water selectivity of 85 %, which can be attributed to its coarse fiber mat structure. While minor oil leakage was observed in the filtered water of both S100 and P100 both demonstrated high oil/water separation abilities with minor oil leakage observed in the filtered water.

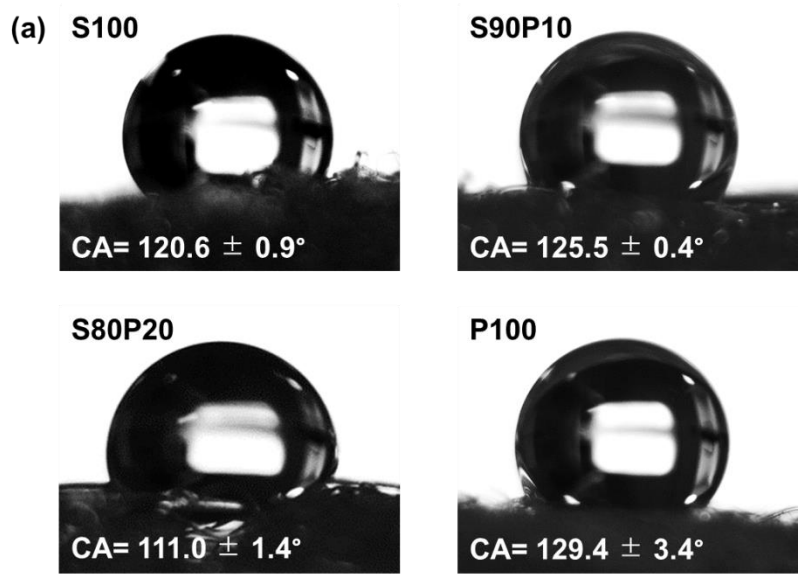

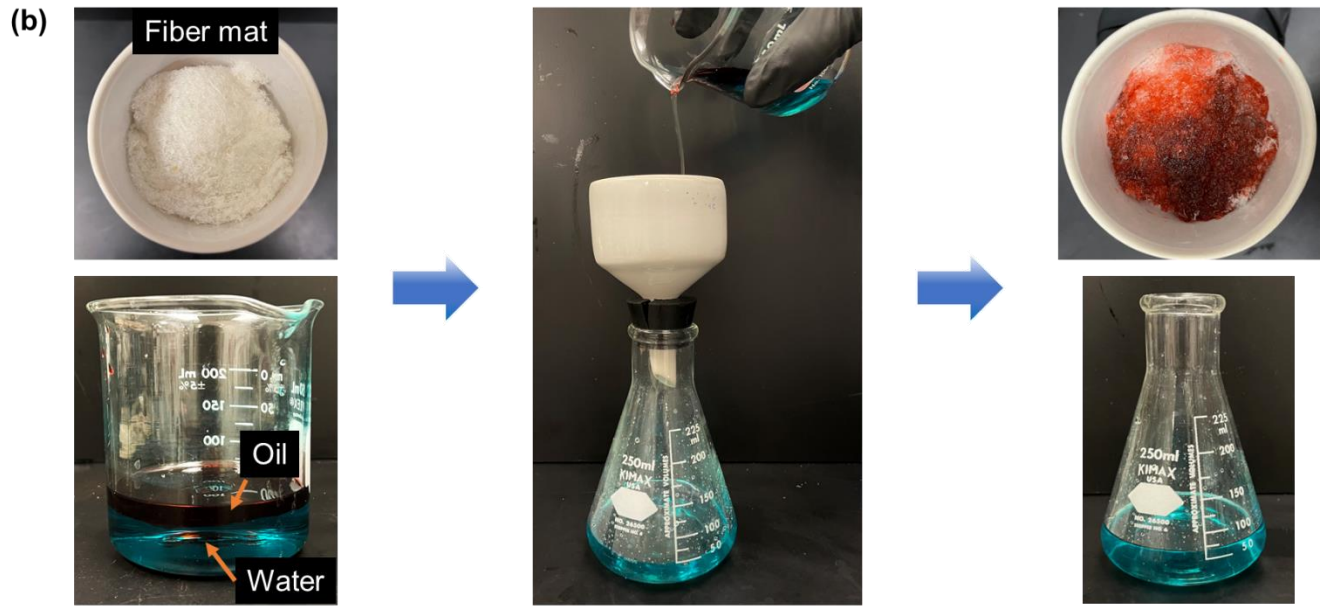

Fig. 4.6. (a) Water contact angle of SEBS/PP fibers (CA: contact angle); (b) Oil/water selectivity test on S90P10.

4.4. Conclusion

This study provides insight into the melt-blown process of the highly elastic tri-block copolymer SEBS, as well as the influence of low-concentration PP loading on the formation of non-woven fibers. Overall, the tri-block copolymer SEBS was successfully processed through a customized laboratory-scale melt-blowing extrusion process to produce continuous and fine non-woven fibers. It was found that a small addition of PP (10 wt.%) significantly improved the melt-blowing processing of SEBS non-woven fibers by acting as a lubricating agent, which was evidently reflected in the processing and morphology analysis of the S90P10 formulation. On the other hand, higher PP loading (20 wt.%) exhibited processing defects, in the form of accumulated SEBS separated at the die exit, which was attributed to the phase separation of SEBS and PP at the

selected processing temperature. Furthermore, oil and water interaction analysis showed that the combination of SEBS and PP provides unique properties that could be useful for oil spill remediation, in which PP helps produce finer fibers to capture more oil while the SEBS provides oil gelation capabilities for the fibers to immobilize the oil within the fiber system. It was shown that the S90P10 formulation exhibited increased oil sorption as well as an enhanced gel formation capacity compared to S100 and S80P20. Moreover, the selective oil-water separation of S90P10 showed that the material nearly isolated 100% of oil from water from a 1:6 ratio oil/water mixture, showcasing great potential utilization of the non-woven SEBS-based fibers in this particular application.

Chapter 5: Concluding Remarks and Future Work

The work presented in this thesis addresses critical environmental issues: oil spill accidents and oil-contaminated wastewater release from industries. The two studies focused on the development of novel, efficient, and high-performance porous materials based on styrene-ethylene-butylene-styrene (SEBS) for oil/water separation and oil sorption applications.

In the first study, A highly effective elastomer foam was successfully developed by blending SEBS with ethylene propylene diene monomer (EPDM) and crosslinking the blend with dicumyl peroxide. The crosslinked SEBS/EPDM foams demonstrated outstanding oil absorption capacity (up to 1030 wt.%), excellent oil/water selectivity, and high oil resistance. Moreover, the foam maintained its morphology after oil absorption, indicating potential for reusability. This work represents a new approach for fabricating elastomer foams using a solvent-free, scalable, and industry-proven melt blending and molding process.

The second study provided insights into the melt-blown process of SEBS and the influence of low-concentration polypropylene (PP) loading on the formation of non-woven fibers. The addition of 10 wt.% PP significantly improved the melt-blown processing and morphology of SEBS non-woven fibers. The combination of SEBS and PP provided unique properties, such as enhanced oil sorption and gel formation capacity, as well as selective oil-water separation.

In the future, the developed materials and processes could be further optimized and scaled up for industrial applications. The reusability and durability of the SEBS-based foams could be investigated in more detail to evaluate their long-term performance and environmental impact.

Additionally, the SEBS foam and SEBS melt-blown fibers could be tested for a broader range of oil types and oil/water mixtures to assess their versatility and practical applicability. Exploring the use of biodegradable or bio-based alternatives to SEBS, EPDM, and PP could also contribute to the development of more sustainable and eco-friendly materials for oil/water separation and oil absorption applications.

Moreover, the knowledge gained from these studies can serve as a foundation for further research on the processing and applications of SEBS-based materials. This includes investigating the impact of various additives, such as compatibilizers or functional fillers, on the properties and performance of SEBS foams and SEBS non-woven fibers.

References

[1] J.S. Sinninghe Damsté, S. Schouten, Biological Markers for Anoxia in the Photic Zone of the Water Column, in: Marine Organic Matter: Biomarkers, Isotopes and DNA, Springer-Verlag, Berlin/Heidelberg, n.d.: pp. 127–163. https://doi.org/10.1007/698_2_005.

[2] B. Zhang, E.J. Matchinski, B. Chen, X. Ye, L. Jing, K. Lee, Marine Oil Spills—Oil Pollution, Sources and Effects, in: World Seas: An Environmental Evaluation, Elsevier, 2019: pp. 391–406. https://doi.org/10.1016/B978-0-12-805052-1.00024-3.

[3] P. Burgherr, In-depth analysis of accidental oil spills from tankers in the context of global spill trends from all sources, J Hazard Mater. 140 (2007) 245–256. https://doi.org/10.1016/j.jhazmat.2006.07.030.

[4] S.M.J. Baban, S. Jules-Moore, An Evaluation of Water Circulation and Contaminant Transport Models for the Intra-American Seas, n.d.

[5] C. Harris, THE SEA EMPRESS INCIDENT: OVERVIEW AND RESPONSE AT SEA, International Oil Spill Conference Proceedings. 1997 (1997) 177–184. https://doi.org/10.7901/2169-3358-1997-1-177.

[6] Q. Zheng, Q. Zhao, W. Nan, C. Li, Oil spill in the Gulf of Mexico and spiral vortex, Acta Oceanologica Sinica. 29 (2010) 1–2. https://doi.org/10.1007/s13131-010-0044-9.

[7] S. Mishra, G. Chauhan, S. Verma, U. Singh, The emergence of nanotechnology in mitigating petroleum oil spills, Mar Pollut Bull. 178 (2022) 113609. https://doi.org/10.1016/j.marpolbul.2022.113609.

[8] M. Baniasadi, S.M. Mousavi, A Comprehensive Review on the Bioremediation of Oil Spills, in: Microbial Action on Hydrocarbons, Springer Singapore, Singapore, 2018: pp. 223–254. https://doi.org/10.1007/978-981-13-1840-5_10.

[9] A.C.S.V. de Negreiros, I.D. Lins, C.B.S. Maior, M.J. das C. Moura, Oil spills characteristics, detection, and recovery methods: A systematic risk-based view, J Loss Prev Process Ind. 80 (2022) 104912. https://doi.org/10.1016/j.jlp.2022.104912.

[10] R.C. Prince, T.J. Amande, T.J. McGenity, Prokaryotic Hydrocarbon Degraders, in: Taxonomy, Genomics and Ecophysiology of Hydrocarbon-Degrading Microbes, Springer International Publishing, Cham, 2019: pp. 1–39. https://doi.org/10.1007/978-3-030-14796-9_15.

[11] R.C. Prince, J.D. Butler, A protocol for assessing the effectiveness of oil spill dispersants in stimulating the biodegradation of oil, Environmental Science and Pollution Research. 21 (2014) 9506–9510. https://doi.org/10.1007/s11356-013-2053-7.

[12] R.P.J. Swannell, F. Daniel, Effect of Dispersants on Oil Biodegradation Under Simulated Marine Conditions, International Oil Spill Conference Proceedings. 1999 (1999) 169–176. https://doi.org/10.7901/2169-3358-1999-1-169.

[13] R.M. Atlas, Microbial hydrocarbon degradation-bioremediation of oil spills, Journal of Chemical Technology & Biotechnology. 52 (2007) 149–156. https://doi.org/10.1002/jctb.280520202.

[14] A. Tuan Hoang, V. Viet Pham, D. Nam Nguyen, A Report of Oil Spill Recovery Technologies, 2018. http://www.ripublication.com.

[15] X. Wang, R. Bartha, Effects of bioremediation on residues, activity and toxicity in soil contaminated by fuel spills, Soil Biol Biochem. 22 (1990) 501–505. https://doi.org/10.1016/0038-0717(90)90185-3.

[16] P.J. Sheppard, K.L. Simons, E.M. Adetutu, K.K. Kadali, A.L. Juhasz, M. Manefield, P.M. Sarma, B. Lal, A.S. Ball, The application of a carrier-based bioremediation strategy for marine oil spills, Mar Pollut Bull. 84 (2014) 339–346. https://doi.org/10.1016/j.marpolbul.2014.03.044.

[17] A.A. Allen, R.J. Ferek, ADVANTAGES AND DISADVANTAGES OF BURNING SPILLED OIL, International Oil Spill Conference Proceedings. 1993 (1993) 765–772. https://doi.org/10.7901/2169-3358-1993-1-765.

[18] J. v Mullin, M.A. Champ, Introduction/Overview to In Situ Burning of Oil Spills, Spill Science & Technology Bulletin. 8 (2003) 323–330. https://doi.org/10.1016/S1353-2561(03)00076-8.

[19] P.E. Ndimele, A.O. Saba, D.O. Ojo, C.C. Ndimele, M.A. Anetekhai, E.S. Erondu, Remediation of Crude Oil Spillage, in: The Political Ecology of Oil and Gas Activities in the Nigerian Aquatic Ecosystem, Elsevier, 2018: pp. 369–384. https://doi.org/10.1016/B978-0-12-809399-3.00024-0.

[20] F. Muttin, R. Campbell, A. Ouansafi, Y. Benelmostafa, Numerical modelling and experimentation of oil-spill curtain booms: Application to a harbor, in: 2017: p. 020104. https://doi.org/10.1063/1.4972696.

[21] A.O. Ifelebuegu, A. Johnson, Nonconventional low-cost cellulose- and keratin-based biopolymeric sorbents for oil/water separation and spill cleanup: A review, Crit Rev Environ Sci Technol. 47 (2017) 964–1001. https://doi.org/10.1080/10643389.2017.1318620.

[22] A. Bayat, S.F. Aghamiri, A. Moheb, G.R. Vakili-Nezhaad, Oil Spill Cleanup from Sea Water by Sorbent Materials, Chem Eng Technol. 28 (2005) 1525–1528. https://doi.org/10.1002/ceat.200407083.

[23] J. Ge, H.-Y. Zhao, H.-W. Zhu, J. Huang, L.-A. Shi, S.-H. Yu, Advanced Sorbents for Oil-Spill Cleanup: Recent Advances and Future Perspectives, Advanced Materials. 28 (2016) 10459–10490. https://doi.org/10.1002/adma.201601812.

[24] D. Loche, L. Malfatti, D. Carboni, V. Alzari, A. Mariani, M.F. Casula, Incorporation of graphene into silica-based aerogels and application for water remediation, RSC Adv. 6 (2016) 66516–66523. https://doi.org/10.1039/C6RA09618B.

[25] Q.F. Wei, R.R. Mather, A.F. Fotheringham, R.D. Yang, Evaluation of nonwoven polypropylene oil sorbents in marine oil-spill recovery, Mar Pollut Bull. 46 (2003) 780–783. https://doi.org/10.1016/S0025-326X(03)00042-0.

[26] J. Wang, Y. Zheng, A. Wang, Superhydrophobic kapok fiber oil-absorbent: Preparation and high oil absorbency, Chemical Engineering Journal. 213 (2012) 1–7. https://doi.org/10.1016/j.cej.2012.09.116.

[27] R. Lin, A. Li, T. Zheng, L. Lu, Y. Cao, Hydrophobic and flexible cellulose aerogel as an efficient, green and reusable oil sorbent, RSC Adv. 5 (2015) 82027–82033. https://doi.org/10.1039/C5RA15194E.

[28] Z. Rahmani, M.T. Samadi, A. Kazemi, A.M. Rashidi, A.R. Rahmani, Nanoporous graphene and graphene oxide-coated polyurethane sponge as a highly efficient, superhydrophobic, and reusable oil spill absorbent, J Environ Chem Eng. 5 (2017) 5025–5032. https://doi.org/10.1016/j.jece.2017.09.028.

[29] J.A. Pavlova, A. v. Ivanov, N. v. Maksimova, K. v. Pokholok, A. v. Vasiliev, A.P. Malakho, V. v. Avdeev, Two-stage preparation of magnetic sorbent based on exfoliated graphite with ferrite phases for sorption of oil and liquid hydrocarbons from the water surface, Journal of Physics and Chemistry of Solids. 116 (2018) 299–305. https://doi.org/10.1016/j.jpcs.2018.01.044.

[30] H. Liu, Y. Kang, Superhydrophobic and superoleophilic modified EPDM foam rubber fabricated by a facile approach for oil/water separation, Appl Surf Sci. 451 (2018) 223–231. https://doi.org/10.1016/j.apsusc.2018.04.179.

[31] Q. Ma, H. Cheng, A.G. Fane, R. Wang, H. Zhang, Recent Development of Advanced Materials with Special Wettability for Selective Oil/Water Separation, Small. 12 (2016) 2186–2202. https://doi.org/10.1002/smll.201503685.

[32] L. Yan, Q. Li, X. Wang, H. Song, H. Chi, Y. Qiao, Y. Zhai, D. Liu, Synthesis and Absorption Performance of Acrylic Ester and Hollow Fiber MgO Nanoparticle Resin Composite, Polym Plast Technol Eng. 56 (2017) 1857–1865. https://doi.org/10.1080/03602559.2017.1295310.

[33] C. Lin, Y.-J. Hong, A.H. Hu, Using a composite material containing waste tire powder and polypropylene fiber cut end to recover spilled oil, Waste Management. 30 (2010) 263–267. https://doi.org/10.1016/j.wasman.2009.03.001.

[34] W. Zhai, J. Jiang, C.B. Park, A review on physical foaming of thermoplastic and vulcanized elastomers, (2021). https://doi.org/10.1080/15583724.2021.1897996.

[35] H.T.T. Duong, R.P. Burford, Effect of foam density, oil viscosity, and temperature on oil sorption behavior of polyurethane, J Appl Polym Sci. 99 (2006) 360–367. https://doi.org/10.1002/app.22426.

[36] R.J. Spontak, N.P. Patel, Thermoplastic elastomers: fundamentals and applications, Curr Opin Colloid Interface Sci. 5 (2000) 333–340. https://doi.org/10.1016/S1359-0294(00)00070-4.

[37] L. Fan, R. Wang, Q. Zhang, S. Liu, R. He, R. Zhang, M. Shen, X. Xiang, Y. Zhou, *In situ* self-foaming preparation of hydrophobic polyurethane foams for oil/water separation, New Journal of Chemistry. 45 (2021) 13902–13908. https://doi.org/10.1039/D0NJ05208F.

[38] X. Qin, B. Wang, X. Zhang, Y. Shi, S. Ye, Y. Feng, C. Liu, C. Shen, Superelastic and Durable Hierarchical Porous Thermoplastic Polyurethane Monolith with Excellent Hydrophobicity for Highly Efficient Oil/Water Separation, Ind Eng Chem Res. 58 (2019) 20291–20299. https://doi.org/10.1021/acs.iecr.9b03717.

[39] Z.C. Ng, R.A. Roslan, W.J. Lau, M. Gürsoy, M. Karaman, N. Jullok, A.F. Ismail, A Green Approach to Modify Surface Properties of Polyurethane Foam for Enhanced Oil Absorption, Polymers (Basel). 12 (2020) 1883. https://doi.org/10.3390/polym12091883.

[40] H. Ding, W. Yang, W. Yu, T. Liu, H. Wang, P. Xu, L. Lin, P. Ma, High hydrophobic poly(lactic acid) foams impregnating one-step Si–F modified lignin nanoparticles for oil/organic solvents absorption, Composites Communications. 25 (2021) 100730. https://doi.org/10.1016/j.coco.2021.100730.

[41] Y. Wang, H. Yang, Z. Chen, N. Chen, X. Pang, L. Zhang, T. Minari, X. Liu, H. Liu, J. Chen, Recyclable Oil-Absorption Foams via Secondary Phase Separation, ACS Sustain Chem Eng. 6 (2018) 13834–13843. https://doi.org/10.1021/acssuschemeng.8b01950.

[42] E. Lopez-Gonzalez, C. Saiz-Arroyo, M.A. Rodriguez-Perez, Low-density open-cell flexible polyolefin foams as efficient materials for oil absorption: influence of tortuosity on oil absorption, International Journal of Environmental Science and Technology. 17 (2020) 1663–1674. https://doi.org/10.1007/s13762-019-02576-0.

[43] J.A. Reglero Ruiz, P. Viot, M. Dumon, Microcellular foaming of polymethylmethacrylate in a batch supercritical CO_2 process: Effect of microstructure on compression behavior, J Appl Polym Sci. 118 (2010) 320–331. https://doi.org/10.1002/app.32351.

[44] B. Xiang, Y. Jia, Y. Lei, F. Zhang, J. He, T. Liu, S. Luo, Mechanical properties of microcellular and nanocellular silicone rubber foams obtained by supercritical carbon dioxide, Polym J. 51 (2019) 559–568. https://doi.org/10.1038/s41428-019-0175-6.

[45] S.-K. Yeh, Z.-E. Liao, K.-C. Wang, Y.-T. Ho, V. Kurniawan, P.-C. Tseng, T.-W. Tseng, Effect of molecular weight to the structure of nanocellular foams: Phase separation approach, Polymer (Guildf). 191 (2020) 122275. https://doi.org/10.1016/j.polymer.2020.122275.

[46] D. Eaves, Handbook of Polymer Foams, Rapra Technology Ltd., 2004.

[47] P. Stevenson, Inter-bubble gas diffusion in liquid foam, Curr Opin Colloid Interface Sci. 15 (2010) 374–381. https://doi.org/10.1016/j.cocis.2010.05.010.

[48] L. Gong, S. Kyriakides, W.-Y. Jang, Compressive response of open-cell foams. Part I: Morphology and elastic properties, Int J Solids Struct. 42 (2005) 1355–1379. https://doi.org/10.1016/j.ijsolstr.2004.07.023.

[49] J.L. Ruiz-Herrero, M.A. Rodríguez-Pérez, J.A. de Saja, Effective diffusion coefficient for the gas contained in closed cell polyethylene-based foams subjected to compressive creep tests, Polymer (Guildf). 46 (2005) 3105–3110. https://doi.org/10.1016/j.polymer.2005.01.093.

[50] S.K. Goel, E.J. Beckman, Generation of microcellular polymeric foams using supercritical carbon dioxide. I: Effect of pressure and temperature on nucleation, Polym Eng Sci. 34 (1994) 1137–1147. https://doi.org/10.1002/pen.760341407.

[51] C.B. Park, L.K. Cheung, A study of cell nucleation in the extrusion of polypropylene foams, Polym Eng Sci. 37 (1997) 1–10. https://doi.org/10.1002/pen.11639.

[52] G. Wypych, DISPERSION AND SOLUBILITY OF BLOWING AGENTS, in: Handbook of Foaming and Blowing Agents, Elsevier, 2017: pp. 45–49. https://doi.org/10.1016/B978-1-895198-99-7.50006-4.

[53] R. Höfer, Processing and Performance Additives for Plastics, in: Polymer Science: A Comprehensive Reference, Elsevier, 2012: pp. 369–381. https://doi.org/10.1016/B978-0-444-53349-4.00272-7.

[54] J. Štěpek, H. Daoust, Chemical and Physical Blowing Agents, in: Additives for Plastics, Springer New York, New York, NY, 1983: pp. 112–123. https://doi.org/10.1007/978-1-4419-8481-4_7.

[55] L. Wang, Y. Hikima, M. Ohshima, A. Yusa, S. Yamamoto, H. Goto, Development of a Simplified Foam Injection Molding Technique and Its Application to the Production of High Void Fraction Polypropylene Foams, Ind Eng Chem Res. 56 (2017) 13734–13742. https://doi.org/10.1021/acs.iecr.7b03382.

[56] Z. Xu, G. Wang, J. Zhao, A. Zhang, G. Dong, G. Zhao, Anti-shrinkage, high-elastic, and strong thermoplastic polyester elastomer foams fabricated by microcellular foaming with CO2 & N2 as blowing agents, Journal of CO2 Utilization. 62 (2022) 102076. https://doi.org/10.1016/j.jcou.2022.102076.

[57] J. Lu, H. Zhang, Y. Chen, Y. Ge, T. Liu, Effect of chain relaxation on the shrinkage behavior of TPEE foams fabricated with supercritical CO2, Polymer (Guildf). 256 (2022) 125262. https://doi.org/10.1016/j.polymer.2022.125262.

[58] J.-H. Kim, K.-C. Choi, J.-M. Yoon, The Foaming Characteristics and Physical Properties of Natural Rubber Foams: Effects of Carbon Black Content and Foaming Pressure, 2006.

[59] M. Amran, Y. Huei Lee, N. Vatin, R. Fediuk, S. Poi-Ngian, Y. Yong Lee, G. Murali, Design Efficiency, Characteristics, and Utilization of Reinforced Foamed Concrete: A Review, Crystals (Basel). 10 (2020) 948. https://doi.org/10.3390/cryst10100948.

[60] J.A. Kosin, J.M. Huber, C.L. Tice, Novel Endothermic Chemical Foaming Agents and Their Applications*, n.d.

[61] R.L. Heck, A Review of Commercially Used Chemical Foaming Agents for Thermoplastic Foams, Journal of Vinyl and Additive Technology. 4 (1998) 113–116. https://doi.org/10.1002/vnl.10027.

[62] A. Rizvi, R.K.M. Chu, J.H. Lee, C.B. Park, Superhydrophobic and Oleophilic Open-Cell Foams from Fibrillar Blends of Polypropylene and Polytetrafluoroethylene, ACS Appl Mater Interfaces. 6 (2014) 21131–21140. https://doi.org/10.1021/am506006v.

[63] G. Wang, G. Wan, J. Chai, B. Li, G. Zhao, Y. Mu, C.B. Park, Structure-tunable thermoplastic polyurethane foams fabricated by supercritical carbon dioxide foaming and their compressive mechanical properties, J Supercrit Fluids. 149 (2019) 127–137. https://doi.org/10.1016/j.supflu.2019.04.004.

[64] Y.-M. Corre, A. Maazouz, J. Duchet, J. Reignier, Batch foaming of chain extended PLA with supercritical CO2: Influence of the rheological properties and the process parameters on the cellular structure, J Supercrit Fluids. 58 (2011) 177–188. https://doi.org/10.1016/j.supflu.2011.03.006.

[65] C. Hopmann, F. Lemke, Q. Nguyen Binh, Foaming of EPDM with water as blowing agent in injection molding, J Appl Polym Sci. 133 (2016). https://doi.org/10.1002/app.43613.

[66] B. Li, G. Zhao, G. Wang, L. Zhang, J. Hou, J. Gong, A green strategy to regulate cellular structure and crystallization of poly(lactic acid) foams based on pre-isothermal cold crystallization and CO2 foaming, Int J Biol Macromol. 129 (2019) 171–180. https://doi.org/10.1016/j.ijbiomac.2019.02.026.

[67] J. Zhao, Q. Zhao, C. Wang, B. Guo, C.B. Park, G. Wang, High thermal insulation and compressive strength polypropylene foams fabricated by high-pressure foam injection molding and mold opening of nano-fibrillar composites, Mater Des. 131 (2017) 1–11. https://doi.org/10.1016/j.matdes.2017.05.093.

[68] B. Li, G. Zhao, G. Wang, L. Zhang, J. Gong, Fabrication of high-expansion microcellular PLA foams based on pre-isothermal cold crystallization and supercritical CO2 foaming, Polym Degrad Stab. 156 (2018) 75–88. https://doi.org/10.1016/j.polymdegradstab.2018.08.009.

[69] H. Liu, W. Zhai, C.B. Park, Biomimetic hydrophobic plastic foams with aligned channels for rapid oil absorption, J Hazard Mater. 437 (2022) 129346. https://doi.org/10.1016/j.jhazmat.2022.129346.

[70] A. Prathap, K.M. Sureshan, Sugar-Based Organogelators for Various Applications, Langmuir. 35 (2019) 6005–6014. https://doi.org/10.1021/acs.langmuir.9b00506.

[71] A. Pal, Y.K. Ghosh, S. Bhattacharya, Molecular mechanism of physical gelation of hydrocarbons by fatty acid amides of natural amino acids, Tetrahedron. 63 (2007) 7334–7348. https://doi.org/10.1016/j.tet.2007.05.028.

[72] S.R. Churipard, K.S. Kanakikodi, D.A. Rambhia, Ch.S.K. Raju, A.B. Halgeri, N. V. Choudary, G.S. Ganesh, R. Ravishankar, S.P. Maradur, Porous polydivinylbenzene (PDVB) as an efficient adsorbent for hydrocarbons: Effect of porogens on adsorption capacity, Chemical Engineering Journal. 380 (2020) 122481. https://doi.org/10.1016/j.cej.2019.122481.

[73] K.T. Kim, C. Park, G.W.M. Vandermeulen, D.A. Rider, C. Kim, M.A. Winnik, I. Manners, Gelation of Helical Polypeptide-Random Coil Diblock Copolymers by a Nanoribbon Mechanism, Angewandte Chemie International Edition. 44 (2005) 7964–7968. https://doi.org/10.1002/anie.200502809.

[74] M. Nandi, S. Banerjee, P. De, Stearoyl-appended pendant amino acid-based hyperbranched polymers for selective gelation of oil from oil/water mixtures, Polym Chem. 10 (2019) 1795–1805. https://doi.org/10.1039/C9PY00105K.

[75] L. Kong, Y. Li, F. Qiu, T. Zhang, Q. Guo, X. Zhang, D. Yang, J. Xu, M. Xue, Fabrication of hydrophobic and oleophilic polyurethane foam sponge modified with hydrophobic Al2O3 for oil/water separation, Journal of Industrial and Engineering Chemistry. 58 (2018) 369–375. https://doi.org/10.1016/j.jiec.2017.09.050.

[76] S. Xiong, Y. Yang, Z. Zhong, Y. Wang, One-Step Synthesis of Carbon-Hybridized ZnO on Polymeric Foams by Atomic Layer Deposition for Efficient Absorption of Oils from Water, Ind Eng Chem Res. 57 (2018) 1269–1276. https://doi.org/10.1021/acs.iecr.7b03939.

[77] D. Yuan, T. Zhang, Q. Guo, F. Qiu, D. Yang, Z. Ou, A novel hierarchical hollow SiO 2 @MnO 2 cubes reinforced elastic polyurethane foam for the highly efficient removal of oil from water, Chemical Engineering Journal. 327 (2017) 539–547. https://doi.org/10.1016/j.cej.2017.06.144.

[78] H. Li, L. Liu, F. Yang, Hydrophobic modification of polyurethane foam for oil spill cleanup, Mar Pollut Bull. 64 (2012) 1648–1653. https://doi.org/10.1016/j.marpolbul.2012.05.039.

[79] A. Visco, A. Quattrocchi, D. Nocita, R. Montanini, A. Pistone, Polyurethane Foams Loaded with Carbon Nanofibers for Oil Spill Recovery: Mechanical Properties under Fatigue

Conditions and Selective Absorption in Oil/Water Mixtures, Nanomaterials. 11 (2021) 735. https://doi.org/10.3390/nano11030735.

[80] X. He, S. Lin, X. Feng, Q. Pan, Synthesis and Modification of Polyurethane Foam Doped with Multi-walled Carbon Nanotubes for Cleaning up Spilled Oil from Water, J Polym Environ. 29 (2021) 1271–1286. https://doi.org/10.1007/s10924-020-01942-1.

[81] T. Zhang, B. Gu, F. Qiu, X. Peng, X. Yue, D. Yang, Preparation of Carbon Nanotubes/Polyurethane Hybrids as a Synergistic Absorbent for Efficient Oil/Water Separation, Fibers and Polymers. 19 (2018) 2195–2202. https://doi.org/10.1007/s12221-018-8399-1.

[82] A. Keshavarz, H. Zilouei, A. Abdolmaleki, A. Asadinezhad, Enhancing oil removal from water by immobilizing multi-wall carbon nanotubes on the surface of polyurethane foam, J Environ Manage. 157 (2015) 279–286. https://doi.org/10.1016/j.jenvman.2015.04.030.

[83] A. Visco, A. Quattrocchi, D. Nocita, R. Montanini, A. Pistone, Polyurethane Foams Loaded with Carbon Nanofibers for Oil Spill Recovery: Mechanical Properties under Fatigue Conditions and Selective Absorption in Oil/Water Mixtures, Nanomaterials. 11 (2021) 735. https://doi.org/10.3390/nano11030735.

[84] M. Anju, N.K. Renuka, Magnetically actuated graphene coated polyurethane foam as potential sorbent for oils and organics, Arabian Journal of Chemistry. 13 (2020) 1752–1762. https://doi.org/10.1016/j.arabjc.2018.01.012.

[85] Z. Lv, N. Zhao, Z. Wu, C. Zhu, Q. Li, Fabrication of Novel Open-Cell Foams of Poly(ε-caprolactone)/Poly(lactic acid) Blends for Tissue-Engineering Scaffolds, Ind Eng Chem Res. 57 (2018) 12951–12958. https://doi.org/10.1021/acs.iecr.8b02233.

[86] S. Wang, W. Yang, X. Li, Z. Hu, B. Wang, M. Li, W. Dong, Preparation of high-expansion open-cell polylactic acid foam with superior oil-water separation performance, Int J Biol Macromol. 193 (2021) 1059–1067. https://doi.org/10.1016/j.ijbiomac.2021.11.033.

[87] X. Gao, R. Li, L. Hu, J. Lin, Z. Wang, C. Yu, Y. Fang, Z. Liu, C. Tang, Y. Huang, Preparation of boron nitride nanofibers/PVA composite foam for environmental remediation, Colloids Surf A Physicochem Eng Asp. 604 (2020) 125287. https://doi.org/10.1016/j.colsurfa.2020.125287.

[88] Q. Hou, X. Wang, The effect of PVA foaming characteristics on foam forming, Cellulose. 24 (2017) 4939–4948. https://doi.org/10.1007/s10570-017-1452-1.

[89] R. Zhang, W. Wan, L. Qiu, Y. Wang, Y. Zhou, Preparation of hydrophobic polyvinyl alcohol aerogel via the surface modification of boron nitride for environmental remediation, Appl Surf Sci. 419 (2017) 342–347. https://doi.org/10.1016/j.apsusc.2017.05.044.

[90] Z. He, H. Wu, Z. Shi, Z. Kong, S. Ma, Y. Sun, X. Liu, Facile Preparation of Robust Superhydrophobic/Superoleophilic TiO_2 -Decorated Polyvinyl Alcohol Sponge for Efficient Oil/Water Separation, ACS Omega. 7 (2022) 7084–7095. https://doi.org/10.1021/acsomega.1c06775.

[91] B. Li, G. Zhao, G. Wang, L. Zhang, J. Gong, Z. Shi, Biodegradable PLA/PBS open-cell foam fabricated by supercritical CO2 foaming for selective oil-adsorption, Sep Purif Technol. 257 (2021). https://doi.org/10.1016/j.seppur.2020.117949.

[92] X. Wang, Y. Pan, X. Liu, H. Liu, N. Li, C. Liu, D.W. Schubert, C. Shen, Facile Fabrication of Superhydrophobic and Eco-Friendly Poly(lactic acid) Foam for Oil–Water Separation via Skin Peeling, ACS Appl Mater Interfaces. 11 (2019) 14362–14367. https://doi.org/10.1021/acsami.9b02285.

[93] S. Jin, X. Wei, Z. Yu, J. Ren, Z. Meng, Z. Jiang, Acoustic-Controlled Bubble Generation and Fabrication of 3D Polymer Porous Materials, ACS Appl Mater Interfaces. 12 (2020) 22318–22326. https://doi.org/10.1021/acsami.0c02118.

[94] M. V. Lorevice, E.O. Mendonça, N.M. Orra, A.C. Borges, R.F. Gouveia, Porous Cellulose Nanofibril–Natural Rubber Latex Composite Foams for Oil and Organic Solvent Absorption, ACS Appl Nano Mater. 3 (2020) 10954–10965. https://doi.org/10.1021/acsanm.0c02203.

[95] U. Hwang, B. Lee, B. Oh, H.S. Shin, S.S. Lee, S.G. Kang, D. Kim, J. Park, S. Shin, J. Suhr, S.-H. Kim, J.-D. Nam, Hydrophobic lignin/polyurethane composite foam: An eco-friendly and easily reusable oil sorbent, Eur Polym J. 165 (2022) 110971. https://doi.org/10.1016/j.eurpolymj.2021.110971.

[96] E.S. Medeiros, G.M. Glenn, A.P. Klamczynski, W.J. Orts, L.H.C. Mattoso, Solution blow spinning: A new method to produce micro- and nanofibers from polymer solutions, J Appl Polym Sci. 113 (2009) 2322–2330. https://doi.org/10.1002/app.30275.

[97] B. Zhao, Experimental study and numerical simulation the air jet flow field of a dual slot sharp blunt die in the melt blowing nonwoven process, Polym Eng Sci. 57 (2017) 417–423. https://doi.org/10.1002/pen.24436.

[98] B.O. Lee, J.A. Ko, S.W. Han, Characteristics of PP/PET Bicomponent Melt Blown Nonwovens as Sound Absorbing Material, Adv Mat Res. 123–125 (2010) 935–938. https://doi.org/10.4028/www.scientific.net/AMR.123-125.935.

[99] Y. Wang, X. Wang, Numerical analysis of new modified melt-blowing dies for dual rectangular jets, Polym Eng Sci. 54 (2014) 110–116. https://doi.org/10.1002/pen.23536.

[100] Y. Kara, K. Molnár, A review of processing strategies to generate melt-blown nano/microfiber mats for high-efficiency filtration applications, Journal of Industrial Textiles. 51 (2022) 137S-180S. https://doi.org/10.1177/15280837211019488.

[101] H. Zhang, Q. Zhen, Z.-Y. Liu, J.-Q. Cui, X.-M. Qian, Facile fabrication of polylactic acid/polyethylene glycol micro-nano fabrics with aligned fibrous roughness for enhancing liquid anisotropic wetting performance via double-stage drafting melt blowing process, Colloids Surf A Physicochem Eng Asp. 648 (2022) 129174. https://doi.org/10.1016/j.colsurfa.2022.129174.

[102] Y. Kara, K. Molnár, A review of processing strategies to generate melt-blown nano/microfiber mats for high-efficiency filtration applications, Journal of Industrial Textiles. 51 (2022) 137S-180S. https://doi.org/10.1177/15280837211019488.

[103] F. Sun, T.-T. Li, X. Zhang, B.-C. Shiu, Y. Zhang, H.-T. Ren, H.-K. Peng, J.-H. Lin, C.-W. Lou, In situ growth polydopamine decorated polypropylen melt-blown membrane for highly efficient oil/water separation, Chemosphere. 254 (2020) 126873. https://doi.org/10.1016/j.chemosphere.2020.126873.

[104] M. Wehmann, W.J.G. McCulloch, Melt blowing technology, in: 1999: pp. 415–420. https://doi.org/10.1007/978-94-011-4421-6_58.

[105] L. Zhang, J. Wu, X. Yang, Y. Di, X. Zhuang, Melt-blowing of silicane-modified phenolic fibrous mat for personal thermal protection, Colloids Surf A Physicochem Eng Asp. 663 (2023) 131076. https://doi.org/10.1016/j.colsurfa.2023.131076.

[106] J.E. Spruiell, E. Bond, Melt spinning of polypropylene, in: 1999: pp. 427–439. https://doi.org/10.1007/978-94-011-4421-6_60.

[107] I.M. Hutten, Processes for Nonwoven Filter Media, in: Handbook of Nonwoven Filter Media, Elsevier, 2007: pp. 195–244. https://doi.org/10.1016/B978-185617441-1/50020-2.

[108] N. Mao, Nonwoven fabric filters, in: Advances in Technical Nonwovens, Elsevier, 2016: pp. 273–310. https://doi.org/10.1016/B978-0-08-100575-0.00010-3.

[109] R. (Rongguo) Zhao, Melt Blown Dies: A Hot Innovation Spot, International Nonwovens Journal. os-11 (2002) 1558925002OS–01. https://doi.org/10.1177/1558925002OS-01100409.

[110] D. Duran, Investigation of the Physical Characteristics of Polypropylene Meltblown Nonwovens Under Varying Production Parameters, in: Thermoplastic Elastomers, InTech, 2012. https://doi.org/10.5772/36798.

[111] J.V. Galaviz, E.H. Rodríguez, M.R. Torrentera, J.J.A. Saiz, Mechanical Design of Primary Air System, Meltblown Banks Machine TL02, Journal of Management Policies and Practices. 3 (2015). https://doi.org/10.15640/jmpp.v3n1a9.

[112] G. Sun, W. Han, Y. Wang, S. Xin, J. Yang, F. Zou, X. Wang, C. Xiao, Overview of the Fiber Dynamics during Melt Blowing, Ind Eng Chem Res. 61 (2022) 1004–1021. https://doi.org/10.1021/acs.iecr.1c03972.

[113] X. Hao, Y. Zeng, A Review on the Studies of Air Flow Field and Fiber Formation Process during Melt Blowing, Ind Eng Chem Res. 58 (2019) 11624–11637. https://doi.org/10.1021/acs.iecr.9b01694.

[114] S. Xie, Y. Zeng, Turbulent Air Flow Field and Fiber Whipping Motion in the Melt Blowing Process: Experimental Study, Ind Eng Chem Res. 51 (2012) 5346–5352. https://doi.org/10.1021/ie202938b.

[115] S. Xie, W. Han, G. Jiang, C. Chen, Turbulent air flow field in slot-die melt blowing for manufacturing microfibrous nonwoven materials, J Mater Sci. 53 (2018) 6991–7003. https://doi.org/10.1007/s10853-018-2008-y.

[116] E.M. Moore, R.L. Shambaugh, D. v. Papavassiliou, Analysis of isothermal annular jets: Comparison of computational fluid dynamics and experimental data, J Appl Polym Sci. 94 (2004) 909–922. https://doi.org/10.1002/app.20963.

[117] B. Zhu, S. Xie, W. Han, G. Jiang, Swirling Diffused Air Flow and Its Effect on Helical Fiber Motion in Swirl-Die Melt Blowing, Fibers and Polymers. 22 (2021) 1594–1600. https://doi.org/10.1007/s12221-021-0809-0.

[118] M.A.J. Uyttendaele, R.L. Shambaugh, Melt blowing: General equation development and experimental verification, AIChE Journal. 36 (1990) 175–186. https://doi.org/10.1002/aic.690360203.

[119] R.S. Rao, R.L. Shambaugh, Vibration and stability in the melt blowing process, Ind Eng Chem Res. 32 (1993) 3100–3111. https://doi.org/10.1021/ie00024a020.

[120] V.T. Marla, R.L. Shambaugh, Three-Dimensional Model of the Melt-Blowing Process, Ind Eng Chem Res. 42 (2003) 6993–7005. https://doi.org/10.1021/ie030517u.

[121] Y. Kara, K. Molnár, Revealing of process–structure–property relationships of fine polypropylene fiber mats generated via melt blowing, Polym Adv Technol. 32 (2021) 2416–2432. https://doi.org/10.1002/pat.5270.

[122] R.R. Bresee, W.-C. Ko, Fiber Formation during Melt Blowing, International Nonwovens Journal. os-12 (2003) 1558925003os–12. https://doi.org/10.1177/1558925003os-1200209.

[123] E.M. Moore, D. V. Papavassiliou, R.L. Shambaugh, Air Velocity, Air Temperature, Fiber Vibration and Fiber Diameter Measurements on a Practical Melt Blowing Die, International Nonwovens Journal. os-13 (2004) 1558925004os–13. https://doi.org/10.1177/1558925004os-1300309.

[124] T. Chen, X. Wang, X. Huang, Effects of Processing Parameters on the Fiber Diameter of Melt Blown Nonwoven Fabrics, Textile Research Journal. 75 (2005) 76–80. https://doi.org/10.1177/004051750507500114.

[125] D. Moyo, A. Patanaik, R.D. Anandjiwala, Process control in nonwovens production, in: Process Control in Textile Manufacturing, Elsevier, 2013: pp. 279–299. https://doi.org/10.1533/9780857095633.3.279.

[126] D.H. Tan, C. Zhou, C.J. Ellison, S. Kumar, C.W. Macosko, F.S. Bates, Meltblown fibers: Influence of viscosity and elasticity on diameter distribution, J Nonnewton Fluid Mech. 165 (2010) 892–900. https://doi.org/10.1016/j.jnnfm.2010.04.012.

[127] H. Yin, Z. Yan, W.-C. Ko, R.R. Bresee, Fundamental Description of the Melt Blowing Process, International Nonwovens Journal. os-9 (2000) 1558925000OS–90. https://doi.org/10.1177/1558925000OS-900408.

[128] Y. Yesil, G.S. Bhat, Porosity and barrier properties of polyethylene meltblown nonwovens, The Journal of The Textile Institute. 108 (2017) 1035–1040. https://doi.org/10.1080/00405000.2016.1218109.

[129] G. Sun, Y. Chen, Y. Ruan, G. Li, W. Hu, S. Xin, Modeling and experimental study of pore structure in melt-blown fiber assembly, Journal of Industrial Textiles. 51 (2022) 6051S-6064S. https://doi.org/10.1177/15280837211011776.

[130] L. Zhang, J.Y. Chen, Comparative study on compressional recovery performance of vertically laid and cross-laid highloft nonwovens, Journal of Industrial Textiles. 51 (2022) 1372S-1391S. https://doi.org/10.1177/1528083720925828.

[131] R.R. Bresee, A. Qureshi, M.C. Pelham, Influence of Processing Conditions on Melt Blown Web Structure: Part 2 -Primary Airflow Rate, International Nonwovens Journal. os-14 (2005) 1558925005os–14. https://doi.org/10.1177/1558925005os-1400202.

[132] A. Ghosal, S. Sinha-Ray, A.L. Yarin, B. Pourdeyhimi, Numerical prediction of the effect of uptake velocity on three-dimensional structure, porosity and permeability of meltblown nonwoven laydown, Polymer (Guildf). 85 (2016) 19–27. https://doi.org/10.1016/j.polymer.2016.01.013.

[133] P.P. Tsai, Characterization of Melt Blown Web Properties using Air Flow Technique, International Nonwovens Journal. os-8 (1999) 1558925099OS–80. https://doi.org/10.1177/1558925099OS-800216.

[134] I. Langmuir, Report on smokes and filters, 1942.

[135] M. Guo, H. Liang, Z. Luo, Q. Chen, W. Wei, Study on melt-blown processing, web structure of polypropylene nonwovens and its BTX adsorption, Fibers and Polymers. 17 (2016) 257–265. https://doi.org/10.1007/s12221-016-5592-y.

[136] W. Wu, T. Hirogaki, E. Aoyama, M. Ikegaya, H. Sota, Investigation of Oil Adsorption Performance of Polypropylene Nanofiber Nonwoven Fabric, J Eng Mater Technol. 141 (2019). https://doi.org/10.1115/1.4041853.

[137] Z. Zhang, D. Yu, X. Xu, H. Li, T. Mao, C. Zheng, J. Huang, H. Yang, Z. Niu, X. Wu, A polypropylene melt-blown strategy for the facile and efficient membrane separation of oil–water mixtures, Chin J Chem Eng. 29 (2021) 383–390. https://doi.org/10.1016/j.cjche.2020.03.033.

[138] X.H. Meng, H.H. Wu, Y.C. Zeng, Blended Polypropylene Fiber of Various MFR via a Melt-Blowing Device for Oil Spill Cleanup, Applied Mechanics and Materials. 624 (2014) 669–672. https://doi.org/10.4028/www.scientific.net/AMM.624.669.

[139] F. Sun, T.-T. Li, H. Ren, Q. Jiang, H.-K. Peng, Q. Lin, C.-W. Lou, J.-H. Lin, PP/TiO2 Melt-Blown Membranes for Oil/Water Separation and Photocatalysis: Manufacturing Techniques and Property Evaluations, Polymers (Basel). 11 (2019) 775. https://doi.org/10.3390/polym11050775.

[140] R.R. Lessard, G. DeMarco, The Significance of Oil Spill Dispersants, Spill Science & Technology Bulletin. 6 (2000) 59–68. https://doi.org/10.1016/S1353-2561(99)00061-4.

[141] Y. Choe, J. Lee, W. Jung, J. Park, J. Lee, J.Y. Jho, K.T. Lee, T. Kim, Y.H. Kim, Gravity-based oil spill remediation using reduced graphene oxide/LDPE sheet for both light and

heavy oils, Process Safety and Environmental Protection. 156 (2021) 617–624. https://doi.org/10.1016/j.psep.2021.10.045.

[142] J. Sayyad Amin, M. Vared Abkenar, S. Zendehboudi, Natural Sorbent for Oil Spill Cleanup from Water Surface: Environmental Implication, Ind Eng Chem Res. 54 (2015) 10615–10621. https://doi.org/10.1021/acs.iecr.5b01715.

[143] A.T. Hoang, X.D. Pham, An investigation of remediation and recovery of oil spill and toxic heavy metal from maritime pollution by a new absorbent material, Journal of Marine Engineering & Technology. 20 (2021) 159–169. https://doi.org/10.1080/20464177.2018.1544401.

[144] Z. Yin, Y. Li, T. Song, M. Bao, Y. Li, J. Lu, Y. Li, An environmentally benign approach to prepare superhydrophobic magnetic melamine sponge for effective oil/water separation, Sep Purif Technol. 236 (2020) 116308. https://doi.org/10.1016/j.seppur.2019.116308.

[145] P.K. Renjith, C. Sarathchandran, V. Sivanandan Achary, N. Chandramohanakumar, V. Sekkar, Micro-cellular polymer foam supported silica aerogel: Eco-friendly tool for petroleum oil spill cleanup, J Hazard Mater. 415 (2021) 125548. https://doi.org/10.1016/j.jhazmat.2021.125548.

[146] Q. Shuai, X. Yang, Y. Luo, H. Tang, X. Luo, Y. Tan, M. Ma, A superhydrophobic poly(dimethylsiloxane)-TiO2 coated polyurethane sponge for selective absorption of oil from water, Mater Chem Phys. 162 (2015) 94–99. https://doi.org/10.1016/j.matchemphys.2015.05.011.

[147] H.-Y. Mi, X. Jing, Y. Liu, L. Li, H. Li, X.-F. Peng, H. Zhou, Highly Durable Superhydrophobic Polymer Foams Fabricated by Extrusion and Supercritical CO_2 Foaming for Selective Oil Absorption, ACS Appl Mater Interfaces. 11 (2019) 7479–7487. https://doi.org/10.1021/acsami.8b21858.

[148] J. Li, C. Xu, Y. Zhang, R. Wang, F. Zha, H. She, Robust superhydrophobic attapulgite coated polyurethane sponge for efficient immiscible oil/water mixture and emulsion separation, J Mater Chem A Mater. 4 (2016) 15546–15553. https://doi.org/10.1039/C6TA07535E.

[149] X. Zhang, X. Wang, X. Liu, C. Lv, Y. Wang, G. Zheng, H. Liu, C. Liu, Z. Guo, C. Shen, Porous Polyethylene Bundles with Enhanced Hydrophobicity and Pumping Oil-Recovery Ability via Skin-Peeling, ACS Sustain Chem Eng. 6 (2018) 12580–12585. https://doi.org/10.1021/acssuschemeng.8b03305.

[150] N. Zhang, S. Zhong, T. Chen, Y. Zhou, W. Jiang, Emulsion-derived hierarchically porous polystyrene solid foam for oil removal from aqueous environment, RSC Adv. 7 (2017) 22946–22953. https://doi.org/10.1039/C7RA02953E.

[151] M. Niaounakis, Foaming and Foamed Products, in: Biopolymers: Processing and Products, Elsevier, 2015: pp. 327–359. https://doi.org/10.1016/B978-0-323-26698-7.00009-X.

[152] W. Zhai, S.N. Leung, L. Wang, H.E. Naguib, C.B. Park, Preparation of microcellular poly(ethylene- *co* -octene) rubber foam with supercritical carbon dioxide, J Appl Polym Sci. (2010) NA-NA. https://doi.org/10.1002/app.31640.

[153] J.A. Sarver, J.L. Sumey, M.L. Williams, J.P. Bishop, D.M. Dean, E. Kiran, Foaming of poly(ethylene -*co*- vinyl acetate) and poly(ethylene -*co*- vinyl acetate -*co*- carbon monoxide) and their blends with carbon dioxide, J Appl Polym Sci. 135 (2018) 45841. https://doi.org/10.1002/app.45841.

[154] J. Lu, H. Zhang, Y. Chen, Y. Ge, T. Liu, Effect of chain relaxation on the shrinkage behavior of TPEE foams fabricated with supercritical CO2, Polymer (Guildf). 256 (2022) 125262. https://doi.org/10.1016/j.polymer.2022.125262.

[155] H. Zheng, G. Pan, P. Huang, D. Xu, W. Zhai, Fundamental Influences of Crosslinking Structure on the Cell Morphology, Creep Property, Thermal Property, and Recycling Behavior of Microcellular EPDM Foams Blown with Compressed CO2, Ind Eng Chem Res. 59 (2020) 1534–1548. https://doi.org/10.1021/acs.iecr.9b05611.

[156] J.G. Drobny, Processing Methods Applicable to Thermoplastic Elastomers, in: Handbook of Thermoplastic Elastomers, Elsevier, 2014: pp. 33–173. https://doi.org/10.1016/B978-0-323-22136-8.00004-1.

[157] G. Polacco, A. Muscente, D. Biondi, S. Santini, Effect of composition on the properties of SEBS modified asphalts, Eur Polym J. 42 (2006) 1113–1121. https://doi.org/10.1016/j.eurpolymj.2005.11.024.

[158] J.K. Kim, M.A. Paglicawan, M. Balasubramanian, Viscoelastic and Gelation Studies of SEBS Thermoplastic Elastomer in Different Hydrocarbon Oils, 2006.

[159] S. Ghosh, D. Khastgir, A.K. Bhowmick, Phase modification of SEBS block copolymer by different additives and its effect on morphology, mechanical and dynamic mechanical properties, J Appl Polym Sci. 67 (1998) 2015–2025. https://doi.org/10.1002/(SICI)1097-4628(19980321)67:12<2015::AID-APP7>3.0.CO;2-P.

[160] P. Sengupta, J.W.M. Noordermeer, Effects of Composition and Processing Conditions on Morphology and Properties of Thermoplastic Elastomer Blends of SEBS-PP-Oil and Dynamically Vulcanized EPDM-PP-Oil, Journal of Elastomers & Plastics. 36 (2004) 307–331. https://doi.org/10.1177/0095244304042668.

[161] B. Wang, Z. Peng, Y. Zhang, Y. Zhang, Compressive response and energy absorption of foam EPDM, J Appl Polym Sci. 105 (2007) 3462–3469. https://doi.org/10.1002/app.26399.

[162] B.Q. Wang, Z.L. Peng, Y. Zhang, Y.X. Zhang, Study on foaming kinetics and preparation of EPDM foams, Plastics, Rubber and Composites. 35 (2006) 360–367. https://doi.org/10.1179/174328906X149673.

[163] H. Wen, M. Wang, S. Luo, Y. Zhou, T. Liu, Mechanical Properties of Silicone Rubber Enhanced Microcellular EPDM Foams Based on Supercritical CO_2 Foaming Technology, Macromol Mater Eng. 306 (2021) 2100310. https://doi.org/10.1002/mame.202100310.

[164] A. Hosseinpour, A.A. Katbab, A. Ohadi, Improving the sound absorption of a highly deformable nanocomposite foam based on ethylene-propylene-diene-monomer (EPDM) infused with multi-walled carbon nanotubes (MWCNTs) to absorb low-frequency waves, Eur Polym J. 178 (2022) 111522. https://doi.org/10.1016/j.eurpolymj.2022.111522.

[165] Y. Shen, B. Xie, W. Yang, Z. Li, M. Yang, Effect of EPDM Content on Melt Flow, Microstructures and Fracture Behavior of Dynamically Vulcanized PP/EPDM Blends, Journal of Macromolecular Science, Part B. 46 (2007) 1127–1138. https://doi.org/10.1080/00222340701582753.

[166] R.W.B. Sharudin, M. Ohshima, CO_2 -Induced Mechanical Reinforcement of Polyolefin-Based Nanocellular Foams, Macromol Mater Eng. 296 (2011) 1046–1054. https://doi.org/10.1002/mame.201100085.

[167] X. Zhang, B. Sun, G. Yuan, S. Zhang, Y. Ji, B. Liu, M. Zhang, Y. Yang, J. Chen, Preparation and balanced mechanical properties of solid and foamed isotactic polypropylene/ <scp>SEBS</scp> composites, J Appl Polym Sci. 138 (2021) 50342. https://doi.org/10.1002/app.50342.

[168] R. Banerjee, S. Sinha Ray, A.K. Ghosh, Dynamic rheology and foaming behaviour of styrene–ethylene–butylene–styrene/ polystyrene blends, Journal of Cellular Plastics. 53 (2017) 389–406. https://doi.org/10.1177/0021955X16652108.

[169] R.W.B. Sharudin, M. Ohshima, Preparation of microcellular thermoplastic elastomer foams from polystyrene -*b* -ethylene-butylene- *b* -polystyrene (SEBS) and their blends with polystyrene, J Appl Polym Sci. 128 (2013) 2245–2254. https://doi.org/10.1002/app.38104.

[170] Z.X. Zhang, X.R. Dai, L. Zou, S.B. Wen, T.K. Sinha, H. Li, A developed, eco-friendly, and flexible thermoplastic elastomeric foam from SEBS for footwear application, Express Polym Lett. 13 (2019) 948–958. https://doi.org/10.3144/expresspolymlett.2019.83.

[171] A.S. Prakash, W.A. Swam, A.N. Strachan, The thermal decomposition of azodicarbonamide (1,1′-azobisformamide), J. Chem. Soc., Perkin Trans. 2. (1975) 46–50. https://doi.org/10.1039/P29750000046.

[172] J. Wang, S. Pan, Y. Zhang, S. Guo, Crosslink network evolution of BIIR/EPDM blends during peroxide vulcanization, Polym Test. 59 (2017) 253–261. https://doi.org/10.1016/j.polymertesting.2016.12.034.

[173] S.M. Tamboli, S.T. Mhaske, D.D. Kale, Crosslinked polyethylene, 2004.

[174] T.L. Chantawansri, A.J. Duncan, J. Ilavsky, K.K. Stokes, M.C. Berg, R.A. Mrozek, J.L. Lenhart, F.L. Beyer, J.W. Andzelm, Phase behavior of SEBS triblock copolymer gels, J Polym Sci B Polym Phys. 49 (2011) 1479–1491. https://doi.org/10.1002/polb.22335.

[175] K. Almdal, J. Dyre, S. Hvidt, O. Kramer, Towards a phenomenological definition of the term ‘gel,’ Polymer Gels and Networks. 1 (1993) 5–17. https://doi.org/10.1016/0966-7822(93)90020-I.

[176] S. Pavlovsky, A. Siegmann, Chemical sensing materials II: Electrically conductive peroxide crosslinked SEBS copolymers systems, J Appl Polym Sci. 114 (2009) 1390–1396. https://doi.org/10.1002/app.30738.

[177] E. Alikhani, M. Mohammadi, M. Sabzi, Preparation and study of mechanical and thermal properties of silicone rubber/poly(styrene–ethylene butylene–styrene) triblock copolymer blends, Polymer Bulletin. (2022). https://doi.org/10.1007/s00289-022-04440-7.

[178] K. Polat, M. Şen, Curing kinetics of styrene-(ethylene-butylene)-styrene (SEBS) copolymer by peroxides in the presence of co-agents, Journal of Polymer Engineering. 34 (2014) 787–792. https://doi.org/10.1515/polyeng-2014-0056.

[179] M.N. Azman Mohammad Taib, N.M. Julkapli, Dimensional stability of natural fiber-based and hybrid composites, in: Mechanical and Physical Testing of Biocomposites, Fibre-Reinforced Composites and Hybrid Composites, Elsevier, 2019: pp. 61–79. https://doi.org/10.1016/B978-0-08-102292-4.00004-7.

[180] Taib M, Julkapli N, Dimensional stability of natural fiber-based and hybrid composites, in: T.M.S.N. Jawaid M (Ed.), Mechanical and Physical Testing of Biocomposites, Fibre-Reinforced Composites and Hybrid Composites, 2019: pp. 441–457. https://doi.org/https://doi.org/10.1016/C2016-0-04437-6.

[181] J.G. Drobny, Thermoplastic Polyurethane Elastomers, in: Handbook of Thermoplastic Elastomers, Elsevier, 2014: pp. 233–253. https://doi.org/10.1016/B978-0-323-22136-8.00009-0.

[182] A. Rizvi, R.K.M. Chu, J.H. Lee, C.B. Park, Superhydrophobic and Oleophilic Open-Cell Foams from Fibrillar Blends of Polypropylene and Polytetrafluoroethylene, (2014). https://doi.org/10.1021/am506006v.

[183] H. Sun, Y. Xi, Y. Tao, J. Zhang, Facile fabrication of multifunctional transparent glass with superhydrophobic, self-cleaning and ultraviolet-shielding properties via polymer coatings, Prog Org Coat. 158 (2021) 106360. https://doi.org/10.1016/j.porgcoat.2021.106360.

[184] H. Sun, J. Zhang, Modified epoxy resin with SEBS-g-MAH to fabricate crack-free and robust hydrophobic coatings on the surface of PP/SEBS matrix, Surfaces and Interfaces. 28 (2022) 101662. https://doi.org/10.1016/j.surfin.2021.101662.

[185] J.K. Kim, I.-H. Kim, Characteristics of surface wettability and hydrophobicity and recovery ability of EPDM rubber and silicone rubber for polymer insulators, J Appl Polym Sci. 79 (2001) 2251–2257. https://doi.org/10.1002/1097-4628(20010321)79:12<2251::AID-APP1032>3.0.CO;2-Q.

[186] R.S. Kurusu, N.R. Demarquette, Blending and Morphology Control To Turn Hydrophobic SEBS Electrospun Mats Superhydrophilic, Langmuir. 31 (2015) 5495–5503. https://doi.org/10.1021/acs.langmuir.5b00814.

[187] T. Zhang, Z. Li, Y. Lü, Y. Liu, D. Yang, Q. Li, F. Qiu, Recent progress and future prospects of oil-absorbing materials, Chin J Chem Eng. 27 (2019) 1282–1295. https://doi.org/10.1016/j.cjche.2018.09.001.

[188] A.A. El-Samak, D. Ponnamma, M.K. Hassan, A. Ammar, S. Adham, M.A.A. Al-Maadeed, A. Karim, Designing Flexible and Porous Fibrous Membranes for Oil Water Separation—A Review of Recent Developments, Polymer Reviews. 60 (2020) 671–716. https://doi.org/10.1080/15583724.2020.1714651.

[189] X. Wang, J. Yu, G. Sun, B. Ding, Electrospun nanofibrous materials: a versatile medium for effective oil/water separation, Materials Today. 19 (2016) 403–414. https://doi.org/10.1016/j.mattod.2015.11.010.

[190] H. Zhang, Q. Zhen, Y. Liu, R. Liu, Y. Zhang, One-step melt blowing process for PP/PEG micro-nanofiber filters with branch networks, Results Phys. 12 (2019) 1421–1428. https://doi.org/10.1016/j.rinp.2019.01.012.

[191] H. Zhang, Q. Zhen, Y. Yan, X. Guan, R. Liu, Y. Liu, Polypropylene/polyester composite micro/nano-fabrics with linear valley-like surface structure for high oil absorption, Mater Lett. 261 (2020) 127009. https://doi.org/10.1016/j.matlet.2019.127009.

[192] A. Molina, P. Vyas, N. Khlystov, S. Kumar, A. Kothari, D. Deriso, Z. Liu, S. Banavar, E. Flaum, M. Prakash, Low cost centrifugal melt spinning for distributed manufacturing of non-woven media, PLoS One. 17 (2022) e0264933. https://doi.org/10.1371/journal.pone.0264933.

[193] J. Drabek, M. Zatloukal, Meltblown technology for production of polymeric microfibers/nanofibers: A review, Physics of Fluids. 31 (2019) 091301. https://doi.org/10.1063/1.5116336.

[194] B. Qi, X. Hu, S. Cui, H. Liu, Y. Li, Y. Li, J. Lu, M. Bao, Rapid fabrication of superhydrophobic magnetic melt-blown fiber felt for oil spill recovery and efficient oil–water separation, Sep Purif Technol. 306 (2023) 122486. https://doi.org/10.1016/j.seppur.2022.122486.

[195] H. Zhang, Q. Zhen, J.-Q. Cui, R.-T. Liu, Y.-F. Zhang, X.-M. Qian, Y. Liu, Groove-shaped polypropylene/polyester micro/nanofibrous nonwoven with enhanced oil wetting capability for high oil/water separation, Polymer (Guildf). 193 (2020) 122356. https://doi.org/10.1016/j.polymer.2020.122356.

[196] A. Rezaei, M. Rowshanzamir, S. Mahdi Hejazi, M. Banitalebi-Dehkordi, Application of superabsorbent geotextiles to decontaminate and improve crude oil-contaminated soil, Transportation Geotechnics. 38 (2023) 100910. https://doi.org/10.1016/j.trgeo.2022.100910.

[197] A.S. Alsagri, A.A. Alrobaian, S.A. Almohaimeed, Concentrating solar collectors in absorption and adsorption cooling cycles: An overview, Energy Convers Manag. 223 (2020) 113420. https://doi.org/10.1016/j.enconman.2020.113420.

[198] I. Ali, V.K. Gupta, Advances in water treatment by adsorption technology, Nat Protoc. 1 (2006) 2661–2667. https://doi.org/10.1038/nprot.2006.370.

[199] J. Park, Evaluation of Changes in the Permeability Characteristics of a Geotextile–Polynorbornene Liner for the Prevention of Pollutant Diffusion in Oil-Contaminated Soils, Sustainability. 13 (2021) 4797. https://doi.org/10.3390/su13094797.

[200] L. Wang, Y. Zeng, H. Lu, Z. Huang, Y. Liu, Gelation at oil–water interface by using dimethylcyclohexylamine/fatty acid-based surface-active ionic liquids, J Mol Liq. 376 (2023) 121428. https://doi.org/10.1016/j.molliq.2023.121428.

[201] D. Juárez, S. Ferrand, O. Fenollar, V. Fombuena, R. Balart, Improvement of thermal inertia of styrene–ethylene/butylene–styrene (SEBS) polymers by addition of microencapsulated phase change materials (PCMs), Eur Polym J. 47 (2011) 153–161. https://doi.org/10.1016/j.eurpolymj.2010.11.004.

[202] J.H. Laurer, R. Bukovnik, R.J. Spontak, Morphological Characteristics of SEBS Thermoplastic Elastomer Gels, Macromolecules. 29 (1996) 5760–5762. https://doi.org/10.1021/ma9607271.

[203] M. Suzuki, Y. Nakajima, M. Yumoto, M. Kimura, H. Shirai, K. Hanabusa, Effects of Hydrogen Bonding and van der Waals Interactions on Organogelation Using Designed Low-Molecular-Weight Gelators and Gel Formation at Room Temperature, Langmuir. 19 (2003) 8622–8624. https://doi.org/10.1021/la034772v.

[204] Y. Wang, E. Shim, N. He, B. Pourdeyhimi, W. Gao, Modeling the Triboelectric Behaviors of Elastomeric Nonwoven Fabrics, Advanced Materials. 34 (2022) 2106429. https://doi.org/10.1002/adma.202106429.

[205] L. Chang, C. Wu, P. Lan, B. Bai, L. Jiang, S. Chen, S. Jerrams, J. Ma, Elastic melt-blown nonwoven fabrication of styrene-ethylene/butylene-styrene copolymer and polypropylene blends: a study of morphology and properties, Textile Research Journal. 92 (2022) 1620–1630. https://doi.org/10.1177/00405175211066359.

[206] S. Besco, A. Lorenzetti, D. Hrelja, C. Boaretti, M. Roso, D. Ferri, M. Modesti, Influence of Melt Viscosity on the Structure and Properties of Electrically Conductive Nanocomposites Produced by Masterbatch Process, Macromol Mater Eng. 299 (2014) 814–824. https://doi.org/10.1002/mame.201300336.

[207] J.W. Harding, J.P. Keller, R.R. Buntin, United States Patent (19), 1974.

[208] A.K. Gupta, S.N. Purwar, Studies on binary and ternary blends of polypropylene with SEBS, PS, and HDPE. I. Melt rheological behavior, J Appl Polym Sci. 30 (1985) 1777–1798. https://doi.org/10.1002/APP.1985.070300501.

[209] A.K. Gupta, K.R. Srinivasan, Melt rheology and morphology of PP/SEBS/PC ternary blend, J Appl Polym Sci. 47 (1993) 167–184. https://doi.org/10.1002/APP.1993.070470118.

[210] E. Saldívar-Guerra, E. Vivaldo-lima, HANDBOOK OF POLYMER SYNTHESIS, CHARACTERIZATION, AND PROCESSING, 2013.

[211] H.E. Burch, C.E. Scott, Effect of viscosity ratio on structure evolution in miscible polymer blends, Polymer (Guildf). 42 (2001) 7313–7325. https://doi.org/10.1016/S0032-3861(01)00240-3.

[212] Y. Kara, K. Molnár, A review of processing strategies to generate melt-blown nano/microfiber mats for high-efficiency filtration applications, Journal of Industrial Textiles. 51 (2022) 137S-180S. https://doi.org/10.1177/15280837211019488/ASSET/IMAGES/LARGE/10.1177_15280837211019488-FIG20.JPEG.

[213] R. Deng, Y. Liu, Y. Ding, P. Xie, L. Luo, W. Yang, Melt electrospinning of low-density polyethylene having a low-melt flow index, J Appl Polym Sci. 114 (2009) 166–175. https://doi.org/10.1002/app.29864.

[214] Kusmono, Z.A. Mohd Ishak, W.S. Chow, T. Takeichi, Rochmadi, Influence of SEBS-g-MA on morphology, mechanical, and thermal properties of PA6/PP/organoclay nanocomposites, Eur Polym J. 44 (2008) 1023–1039. https://doi.org/10.1016/J.EURPOLYMJ.2008.01.019.

[215] S.C. Tjong, S.A. Xu, R.K.Y. Li, Y.W. Mai, Mechanical behavior and fracture toughness evaluation of maleic anhydride compatibilized short glass fiber/SEBS/polypropylene hybrid composites, Compos Sci Technol. 62 (2002) 831–840. https://doi.org/10.1016/S0266-3538(02)00037-4.

[216] D. Rigger, EDIBLE OILS: ARE THEY REALLY THAT DIFFERENT?, International Oil Spill Conference Proceedings. 1997 (1997) 59–61. https://doi.org/10.7901/2169-3358-1997-1-59.

[217] J. Saleem, M. Adil Riaz, M. Gordon, Oil sorbents from plastic wastes and polymers: A review, J Hazard Mater. 341 (2018) 424–437. https://doi.org/10.1016/j.jhazmat.2017.07.072.

[218] S. Basak, J. Nanda, A. Banerjee, A new aromatic amino acid based organogel for oil spill recovery, J Mater Chem. 22 (2012) 11658. https://doi.org/10.1039/c2jm30711a.

Appendix A

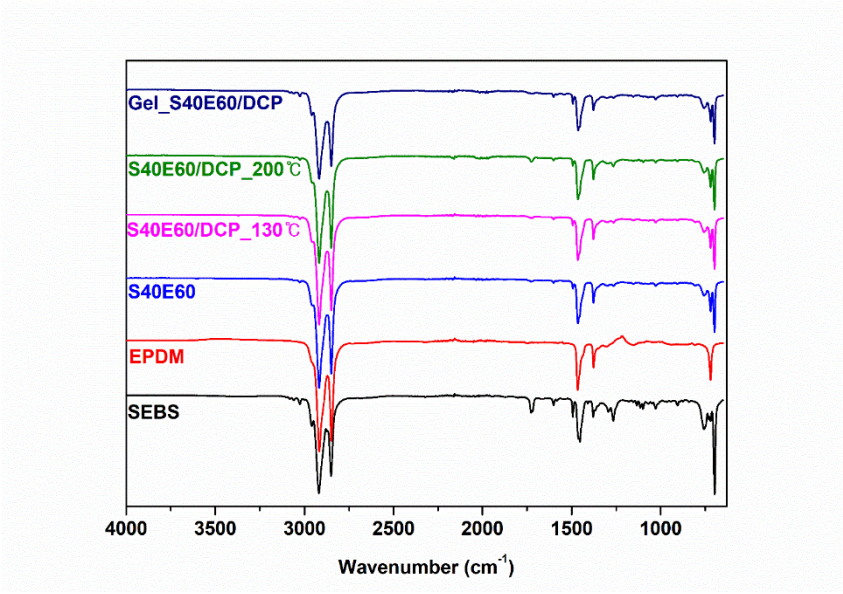

Fig. A1. FTIR of 1) SEBS, 2) EPDM, 3) S40E60 4) S40E60/DCP sheet processed at 130 ℃, 5) S40E60/DCP foam processed at 200 ℃, and 6) Gel of S40E60/DCP.

FTIR analysis was carried out for the 6 samples listed above. Samples 1) and 2) are pure materials. Sample 3) is a blend of SEBS 40 wt.% and EPDM 60 wt.% without any chemical additives such as a foaming agent or a cross-linker. Sample 4) is a blend of SEBS 40 wt.%, EPDM 60 wt.%, and DCP without adding a chemical foaming agent. This material hasn't undergone cross-linking process yet. Sample 5) is sample 4) after being cross-linked. Sample 6) is a gel of sample 5) after being extracted in Toluene.

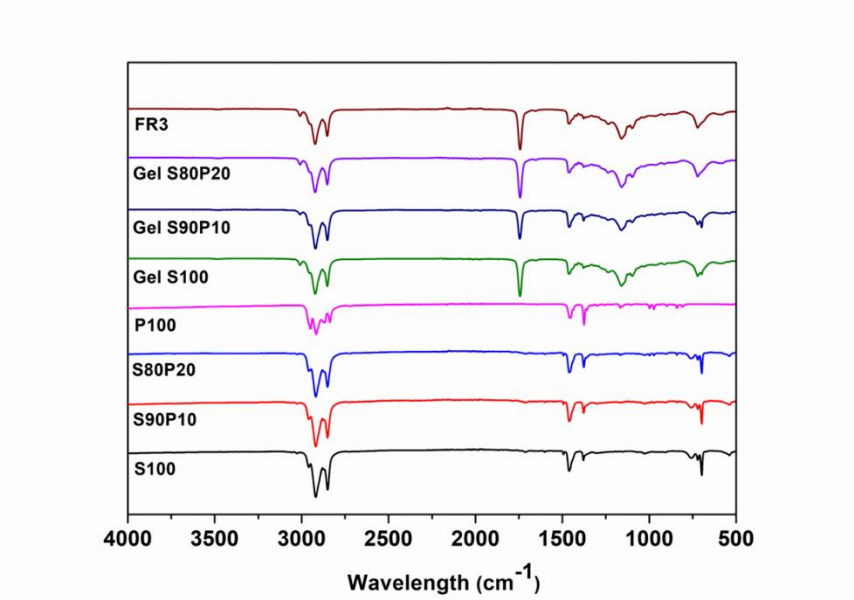

Fig. A2. FTIR of SEBS/PP fibers, gelled fibers, and FR3 (vegetable oil).

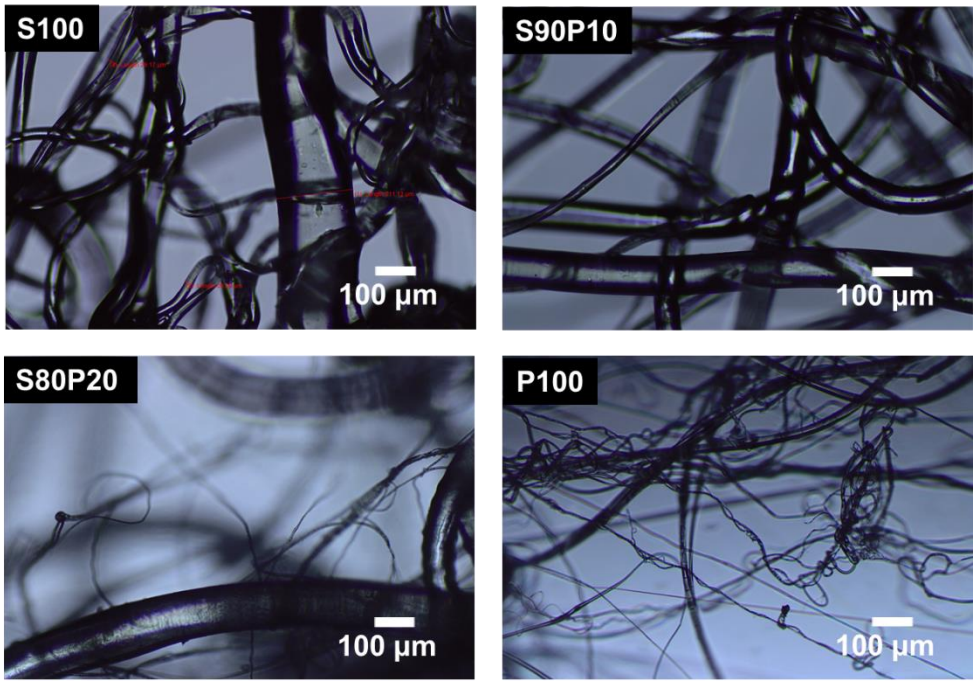

Fig. A3. Additional polarized optical microscope images of SEBS/PP fibers.

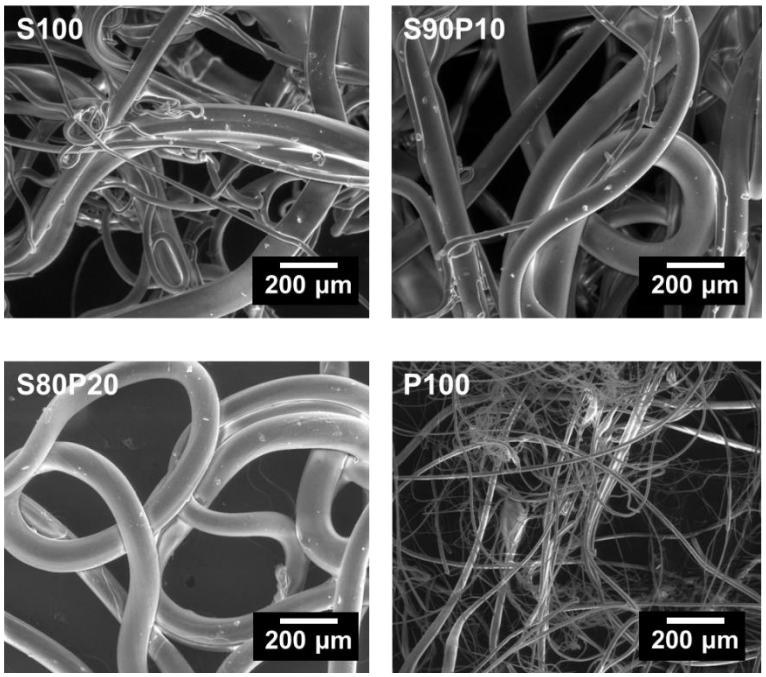

Fig. A4. SEM image of SEBS/PP fibers.

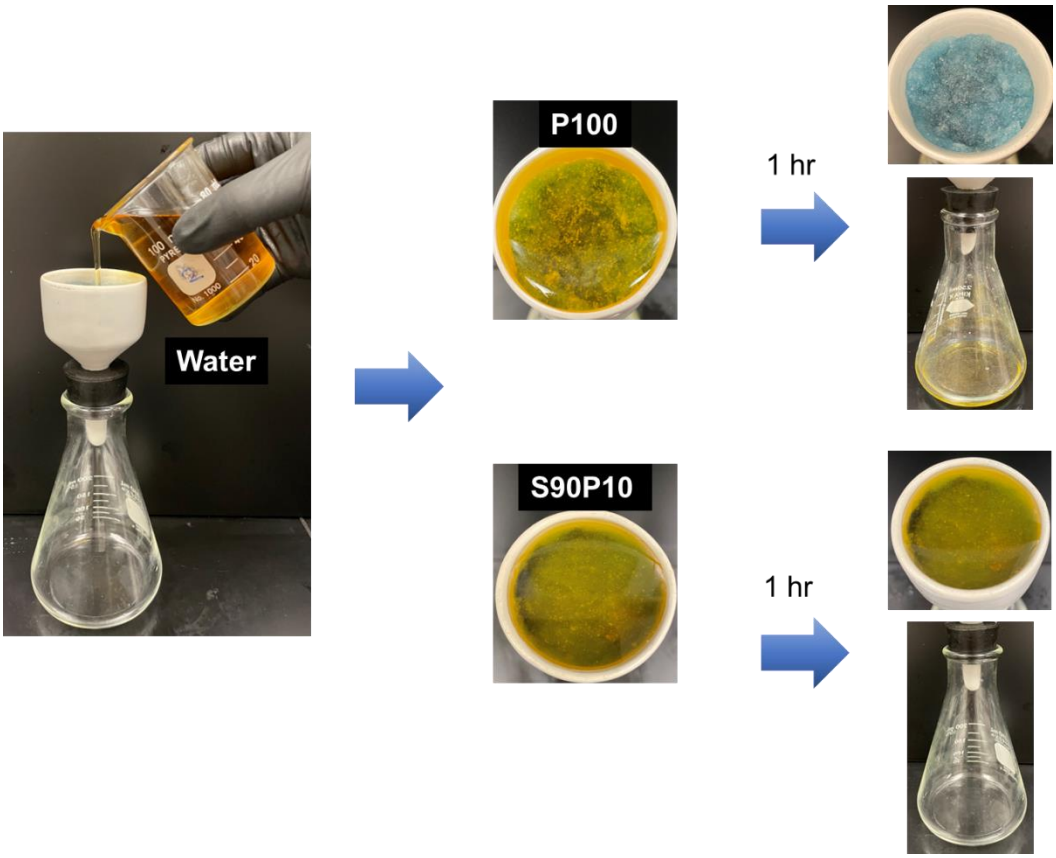

Fig. A5. Water penetration test of P100 and S90P10.

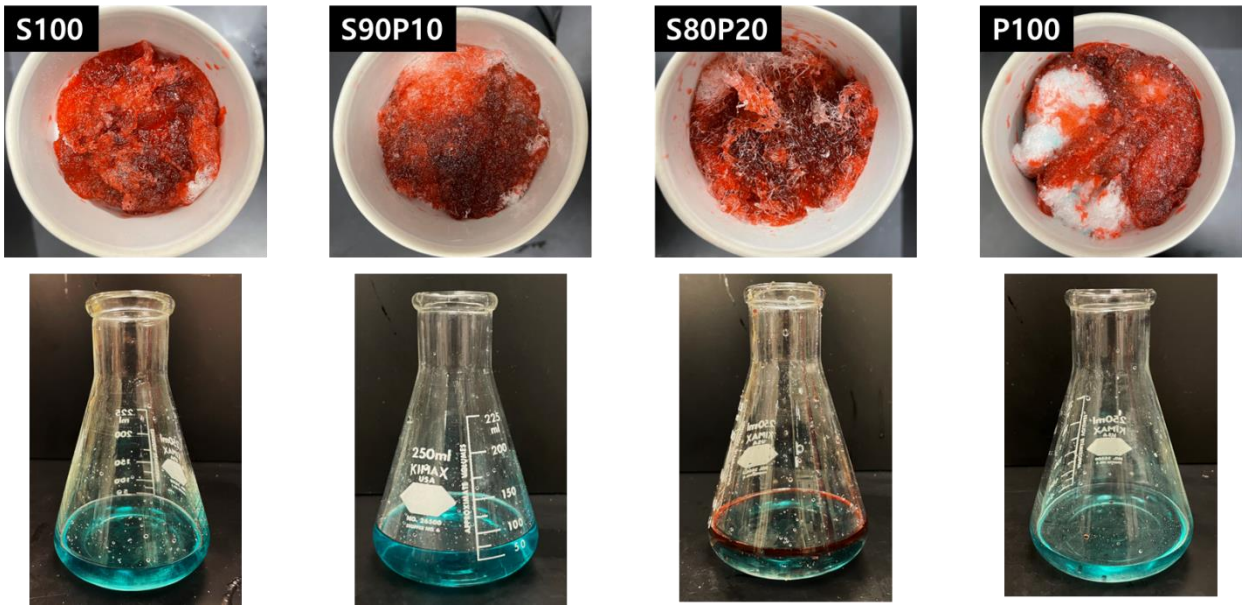

Fig. A6. Oil/water separation test results of SEBS/PP fibers.